Epitaxial Growth of Lead and Bismuth on Silver and Silver Rich Alloys

Thesis submitted in accordance with the requirements of
the University of Liverpool for the degree of
Doctor in Philosophy by

Ian Mathew McLeod

February 2014

Abstract

Epitaxial Growth of Lead and Bismuth on

Silver and Silver Rich Alloys

The growth of Bi on Ag(111) induces different surface structures, including ($\sqrt{3} \times \sqrt{3}$)R30°surface alloy, Bi-(p×) overlayer and Bi(110) thin film as a function of increasing Bi coverage. These structures have been studied using low-temperature scanning tunneling microscopy, low-energy electron diffraction, ab initio calculations and photoemission spectroscopy from core-levels and valence bands at room temperature.

At 1/3 of a monolayer of Bi on Ag(111) leads to the formation of $BiAg_2$ surface alloy with a long range ordered ($\sqrt{3} \times \sqrt{3}$)R30° superstructure. A detailed analysis of this structure using LEED I-V measurements together with DFT calculations is presented. The Bi atom is found to replace one top layer Ag atom in each unit cell, forming a substitutional $BiAg_2$ surface alloy. This mode of accommodation of Bi was found to be energetically favourable based on ab initio total-energy calculations.

Based on photoemission spectroscopy we find the sp-derived Shockley surface state on Ag(111) is rapidly quenched upon deposition of Bi, due to the strong variation of in-plane surface potential in the Ag_2Bi surface alloy. The core levels of Bi 4f of the ($\sqrt{3} \times \sqrt{3}$)R30° Ag_2Bi alloy and Bi(110) thin film are shifted to lower binding energy by ~0.6 eV and ~0.3 eV compared with the Bi bulk value, respectively. Mechanisms inducing the core level shifts are discussed as due to a complex superposition of several factors.

At coverage above a critical value of 0.55 monolayers, the Ag_2Bi alloy phase gradually converts into an ordered Bi (p × √3) overlayer structure supported on Ag(111). We postulate that the dealloying transition is likely driven by compressive strain induced by incorporation of large-size Bi atoms into Ag at a high coverage and the subsequent lack of miscibility of Ag and Bi bulk phases. After completion of the dealloying process, Bi(110) thin films can be grown epitaxially on top of Ag(111) with a chemically abrupt interface.

The deposition of 1/3 of a monolayer of Pb on Ag(111) leads to the formation of Ag_2Pb surface alloy with a long range ordered (√3x√3)R30° superstructure. A detailed analysis of this structure using LEED I-V and MEIS measurements together with DFT calculations is presented.

Quasicrystals, materials with aperiodic long-range order, are usually formed by at least two elements with a specific chemical composition. In this study, we demonstrate that, a single element multilayer quasicrystal can be formed on a template. Using a hitherto unexplored quasicrystalline substrate, the icosahedral Ag-In-Yb quasicrystal, and various experimental techniques including scanning tunneling microscopy combined with theoretical calculations of adsorption energies, we identify the initial adsorption sites for Pb atoms on the substrate and hence deduce the multilayer structure of the Pb overlayer. We propose a mechanism for the growth of epitaxial materials on the quasicrystalline substrate.

.

Acknowledgements

I would like to thank my supervisor Dr. Vinod Dhanak for all of his help and support throughout my time as a research student. I'm sure I would not have made it to the end without his motivation and I am pleased to count him as a friend.

Special thanks to Katariina Pussi and her co-workers for their outstanding efforts with the DFT and LEED I-V analysis.

Many thanks to all of my co-workers, detailed in the publication list, who were involved in the experimental effort. Special thanks to Dr. K. H. L. Zhang for collaborating with me and for providing invaluable insight into the results. Thanks also to David Hesp for his continued help with the work and equipment in the lab.

Finally, thank you to all of my family and friends for pretending to be interested in my work and to Laura for her immense support. It is to her that I dedicate this thesis.

Authors Contributions to Publications

Chapter 3   Zhang, K.H.L., McLeod, I.M., Lahti, M., Pussi, K., and Dhanak, V.R., 2012. The evolution of the electronic structure at the Bi/Ag(111) interface studied using photoemission spectroscopy. *Journal of Physics: Condensed Matter*, **24(43), pp. 435502.** I. M. McLeod collected the data and worked with K.H.L Zhang on its analysis. K.H.L Zhang authored the first draft of the paper. I. M. Mcleod reworked the paper following referees comments. M Lahti, K Pussi and V R Dhanak were involved in the discussion of the findings.

Chapter 4   Zhang, K.H.L., McLeod, I.M., Lu, Y.H., Dhanak, V.R., Matilainen, A., Lahti, M., Pussi, K., Egdell, R.G., Wang, X.S., Wee, A.T.S. and Chen, W., 2011. Observation of a surface alloying-to-dealloying transition during growth of Bi on Ag(111). *Phys. Rev. B,* **83(23), pp. 235418.** K. H. L. Zhang, X. S. Wang, A. T. S. Wee, and W. Chen collected the data. I. M. McLeod worked with K.H.L Zhang on its analysis. K. H. L Zhang authored the paper. All authors, including V. R. Dhanak, A. Matilainen, M. Lahti, K. Pussi, and R. G. Egdell were involved in the discussion of the findings.

Chapter 5   McLeod, I.M., Dhanak, V.R., Matilainen, A., Lahti, M., Pussi, K. and Zhang, K.H.L., 2010. Structure determination of the Bi–Ag(111) surface alloy using LEED I–V and DFT analyses. *Surface Science,* **604(17–18), pp. 1395-1399.** I. M. McLeod collected the data and authored the paper. A. Matilainen, M. Lahti and K. Pussi carried out LEED I-V analysis and DFT calculations though the LEED I-V was later repeated at Liverpool. All authors, including K.H.L Zhang and V.R. Dhanak, were involved in the discussion of the findings.

Chapter 6 **McLeod, I.M., Dhanak, V.R., Lahti, M., Matilainen, A., Pussi, K. and Zhang, K.H.L., 2011. LEED *I–V* and DFT structure determination of the Pb–Ag(111) surface alloy.** *Journal of Physics: Condensed Matter,* **23, pp. 265006.** I. M. McLeod collected the data and authored the paper. A. Matilainen, M. Lahti and K. Pussi carried out LEED I-V analysis and DFT calculations though the LEED I-V was later repeated at Liverpool. All authors, including K.H.L Zhang and V.R. Dhanak, were involved in the discussion of the findings.

Chapter 7 **McLeod, I.M., Sercomb, D., Bailey, P., and Noakes, T. Structure Determination of the p($\sqrt{3}\times\sqrt{3}$)R30° Pb-Ag(111) Surface Alloy Using MEIS.** *Awaiting Publication.* I. M. McLeod, D. Sercomb P. Bailey and T. Noakes were involved with data collection. I. M. McLeod performed the analysis and authoered the paper. All authors, including V. R. Dhanak, were involved in the discussion of the findings.

Chapter 8 **Sharma, H. R., Nozawa, K., Smerdon, J. A., Nugent, P. J., McLeod, I., Dhanak, V. R., Shimoda, M., Ishii, Y., Tsai, A.P., McGrath, R. 2013. Templated three-dimensional growth of quasicrystalline lead. Nature communications, 4.** I. M. McLeod collected and analysed the XPS data. J. A. Smerdon and P. J. Nugent collected STM data though this was later repeated by I. M. McLeod. H. R. Sharma analysed the STM data and authored the paper. Theoretical calculations were done by K. Nozawa. All authors, including M. Shimoda, Y. Ishii, A. P. Tsai, and R. McGrath, were involved in the discussion of the findings.

Contents

Chapter 9 **Conclusions** **170**

Appendix **List of Publications**

Chapter 1

Introduction and Background

1.1 - Introduction

A thin film is a layer of material ranging from fractions of a nanometer (monolayer) to several micrometers in thickness. Electronic semiconductor devices and optical coatings are the main applications benefiting from thin-film construction though their use is much wider ranging than this.

The growth of thin metal films on metallic substrates has received a lot of attention in recent years. Clearly bulk alloys are of great interest and often possess mechanical and electronic qualities which differ vastly from their elemental constituents. Surface alloys are also of particular interest and exhibit their own range of interesting and useful phenomenon.

Recently, 2D surface alloys were identified as a new class of materials that exhibit a particularly large Rashba-Bychkov-type (RB) spin splitting [1,2]. A surface alloy is formed by replacing every third atom of a silver or copper (111) surface by a heavy atom such as bismuth, lead or antimony. Although (Bi, Pb, Sb) and Ag atoms are immiscible in the bulk they form long-range ordered surface alloys, where every third Ag atom is replaced by an alloy atom. In these systems a spin splitting of the 2D band structure due to the RB effect is seen. The RB model states that in a symmetry broken environment (such as the surface of a semi-infinite crystal) the spin-orbit interaction will lift the spin-degeneracy of the band structure. Such a spin-split band structure bares great potential for applications in the field of spintronics, e.g. in a Datta-Das spin field effect transistor [3]. Despite significant recent interest in these systems [4-12], detailed surface structural investigation of this class of surface alloy is lacking in the literature. Furthermore, bismuth coated Ag nano particles show enhanced surface plasmon resonance, with potential applications in photonics and photovoltaic devices (PV) [13].

Indeed, recently there has been considerable interest in silver nano particles because of their unique optical and electrical properties resulting from electron quantum confinement effects. Examples of applications range from PV to biological and chemical sensors. An increasingly common application is in the use of silver nano particles for antimicrobial coatings. Industrial processes involving the use of silver is as conductive adhesives in electronic circuit board industry and in catalysis, and a possible route to improving such processes is to modify the silver surfaces by alloying with other metals. An example is the use of bismuth silver system used in lead free solder [14]. Silver surfaces have also been recently used to support silicine monolayers grown by epitaxial growth of silicon from the vapour phase [15].

The present thesis is concerned with using surface science techniques to investigate the thin film growth of so called semi-metals, namely lead and bismuth, on silver and silver rich surfaces. Using a variety of analysis techniques, detailed structural analysis and surface characterisation is provided for each of the studied systems.

As the alloy systems studied in this body of work are of current interest and are still receiving attention from various sections of the scientific community, the decision was made to to publish the data along the way. Given this, the decision has been made to present the work as a collection of papers with each paper forming a separate chapter.

Chapter 2 gives a brief overview of the techniques used in the work along with some experimental details and descriptions of the equipment.

In Chapter 3 examines the Bi/Ag(111) system, looking at the evolution of the electronic structure at the interface. Bi is a typical semimetal with a small density of states at the Fermi level [16, 17]. However, studies on the low index surfaces of Bi such as Bi(111), Bi(100) and Bi(110) have shown that these surfaces are much more metallic than the

bulk with a high density of states at the Fermi level [18-22]. The surface electronic states have been attributed to the spin-orbit (SO) splitting of the bands at the surface due to the breakdown of spatial inversion symmetry perpendicular to the surface (Rashba-Bychkov effect) [1,23]. More interestingly, a Bi induced $(\sqrt{3} \times \sqrt{3})R30°$ surface alloy structure on Ag(111) has received considerable attention, because it exhibits exceptionally large spin-orbit splitting of its surface states [5]. In this chapter, we extend these structural studies by reporting on the evolution of electronic states of these Bi structures using X-ray/ultraviolet photoemission spectroscopy (XPS/UPS).

Chapter 4 looks at the surface alloying-to-dealloying transition during growth of Bi on Ag(111). As previously stated, submonolayer Bi on Ag(111) forms a $(\sqrt{3} \times \sqrt{3})R30°$ surface alloy.[1] The $(\sqrt{3} \times \sqrt{3})R30°$ structure is of particular interest because the inter-mixing of the size mismatched atoms and the corresponding in-plane potential variations lead to giant SO splitting, which has implications for spintronics applications.[6,7,24] Nonetheless, a detailed investigation of the atomic structures of these two- dimensional (2D) surface alloys is still lacking, even though such structural information plays a critical role in determining the in-plane potential gradient, and thus the SO splitting of the surface alloys.[25] Furthermore, a similar class of electronic states evolves by the quantum confinement of electrons in ultrathin films with a thickness comparable to the electron coherence length, to give so-called quantum well states. In this chapter we present a detailed study of the nucleation of Bi on Ag(111), the subsequent development of the Ag_2Bi surface alloy, and the growth of a Bi thin film on Ag(111) using STM data and ab initio total-energy calculations. We show that after the initial formation of a substitutional surface alloy, a dealloying process ensues with

increasing Bi coverage. For coverages above 1 monolayer (ML), the Ag_2Bi surface alloy demixes and a highly ordered Bi(110) monolayer is formed on top of Ag(111).

Chapter 5 begins by looking at the surface alloy which is formed when approximately 1/3 of a monolayer of Bi is deposited on the Ag(111) surface. Bismuth is a particularly attractive adsorbate material due to its small electron effective mass, anomalously high values of electron mean free path and mobility, highly anisotropic Fermi surface as well as having a long Fermi wavelength at room temperature and small overlap between the conduction and valence bands [26-29]. At 1/3 ML coverage of Bi on Ag(111) we report the formation of $BiAg_2$ surface alloy with a long range ordered $(\sqrt{3} \times \sqrt{3})R30°$ superstructure. A detailed analysis of this structure is presented using LEED I-V measurements together with DFT calculations.

Chapter 6 essentially repeats the work of Chapter 5, only in this time Bi is replaced with Pb. The case of Pb/Ag(111) has, in fact, been the subject of recent studies both from a structural and electronic point of view [4,30]. Interestingly, Dalmas *et al.* [31] reported a rumpling not only between the Pb and Ag atoms in the surface layer but also between the two Ag atoms in the unit cell of this surface layer, as seen with scanning tunneling microscopy (STM). They speculated this phenomenon was induced by a Pierls type distortion although such an effect has not been seen in any similar systems. Given the interest in these materials for properties such as the Rashba effect and the fact that Rashba energies can be tuned with small changes in surface composition and structure [8,32], as well as the unusual nature of the rumpling, we have carried out this further structural study on the system.

Chapter 7 revisits the Pb/Ag(111) $(\sqrt{3} \times \sqrt{3})R30°$ structure. This time the surface is analysed using the technique of medium energy ion scattering in an attempt to further

clarify the reported situation of rumpling between the two Ag atoms of the surface unit cell.

Chapter 8 looks at the growth of Pb, Bi and Sb on the icosahedral Ag-In-Yb quasicrystal. Here we demonstrate the formation of a novel form of quasicrystalline structure, which is formed by single elements grown on a template. Using a hitherto unexplored quasicrystalline substrate, the fivefold surface of the icosahedral (i -) Ag-In-Yb quasicrystal, we have succeeded in growing multilayered quasicrystalline films of the single elements Pb, Bi and Sb, in contrast to all previous observations.

1.2 - Background to Quasicrystals

It is worth spending a little more time reviewing quasicrystals as they generally fall outside the remit of most standard condensed matter physics courses. Quasi-periodic crystals, or quasicrystals, as they are commonly known, are intermetallic alloys with long range atomic ordering but as they have no translational symmetry they effectively have an infinite unit cell. Despite this, there is ordering to their structures, which is evident when we look at their diffraction patterns. LEED images show clearly defined spots although typically they have orders of rotational symmetry which were originally thought impossible. As such they are often termed as 'the third state of solid matter' as they are neither amorphous nor truly crystalline.

The formation of quasicrystals generally requires quite precise stoichiometry with even small changes in composition preventing their formation. It is also the case that quasicrystals consisting of just two elements have a tendency to be unstable. However, the addition of a third metal may be used to stabilise the structure [33]. So far there are

more than a hundred binary, ternary and quaternary, stable quasicrystals with rotational symmetry of 5-, 8-, 10- and 12- fold [34-36]. The order of symmetry may sometimes be visible in the morphology of the grain, Figure 1.1.

In terms of their macroscopic properties, quasicrystals tend to exhibit slightly unusual properties, contrasting with those of their constituent parts. For example, typical electrical conductivity, σ, is around 10^2 $\Omega^{-1}.cm^{-1}$ and thermal conductivity, κ, is around $3\ W.m^{-1}.K^{-1}$. The cause of these unusual properties is the low density of states at the Fermi level, termed the `pseudogap'. This is due to strong electron scattering by the structure leading to a hybridisation of the electronic states at the atomic cluster level.
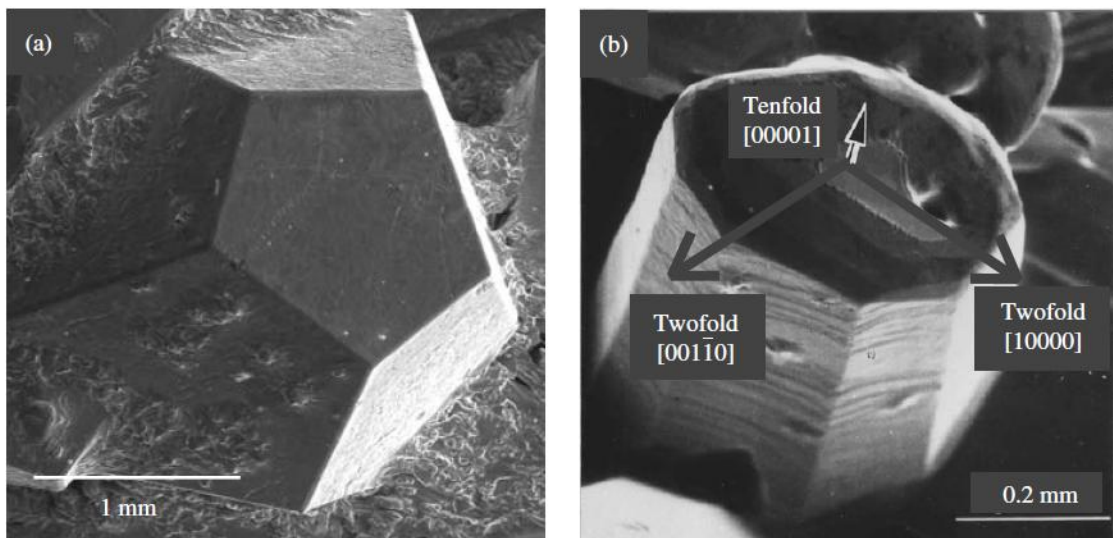
Figure 1.1 - (a) Scanning electron microscopy (SEM) micrograph showing an as-grown single-grain samples of i-Al-Pd-Re and (b) d-Al-Ni-Co quasicrystal showing different high-symmetry axes. Figure reproduced from [28].

Aside from being interesting on a fundamental basis, quasicrystals have generated interest for a number of possible engineering applications due to their surface qualities, i.e. they are quite hard materials with low frictional coefficients with unique morphology. This means they are potentially ideal for non-stick coatings, low friction

coating for combustion engines, reinforced composite materials, as well as possible catalytic properties. It is still to be determined whether their macroscopic properties are as a result of their aperiodic ordering or their complex chemical nature.

There are two types of quasicrystal. The first type, polygonal quasicrystals, have an axis of 8-, 10-, or 12-fold local symmetry (octagonal, decagonal, or dodecagonal quasicrystals, respectively). They are periodic along this axis and quasiperiodic in planes normal to it. The second type, icosahedral quasicrystals, are aperiodic in all directions. Icosahedral quasicrystals are quasi periodic in all three spatial directions and possess three different high symmetry axes: fivefold, threefold and twofold. The threefold axes are located 37.4° away from the fivefold axis. Every five threefold axes form a cone. Similarly, the twofold axes are located 31.7° (the nearest neighbour angle) away from the same axis [37]. These high symmetry axes can be seen in Figure 1.1.

1.2.1 - Creation and availability of quasicrystals

In order to study quasicrystals, we ideally require single grain samples in the order of mm in size. There are only relatively few systems which meet these requirements and which are also suitable for use in UHV. Icosahedral samples include Ag-In-Yb, Al-Pd-Mn, i-Al-Cu-Ru and i-Al-Cu-Fe amongst others and although there are still more systems being discovered the list is relatively small.

For 16 years after the publication of Dan Shechtman's discovery [38], the majority of subsequently discovered stable quasicrystals were ternary alloys usually consisting of Al and two other constituents. Several binary quasicrystals were discovered, such as the dodecagonal quasicrystal Ta-Te, but their lack of abundance and stability made them more difficult to study. In 2000, Tsai et al published the discovery of the first thermodynamically stable binary quasicrystal [39].

Tsai et al have been able to prepare quasicrystals alloys made from Cd-Mg-RE (where RE is a rare earth). This family of quasicrystals was discovered taking an i-Zn-Mg-RE and replacing the Zn component with Cd. Quasicrystals can be considered to be a Hume-Rothery electron compound with a definite valence concentration (valence to electron atom ratio or e/a) of roughly 2 [40]. The e/a ratio may be calculated by;

$$e/a = Z_A(1-c_B) + Z_B c_B \tag{1.1}$$

where Z is the valency species of A and B and c_B is the concentration of species B.

The e/a ratio is an important determinant of crystal structures due to its indication of how full the Brillouin zones are. If a Brillouin zone is filled but more electrons are present it is energetically favourable to change the shape of the Brillouin zone to accommodate more than to promote electrons across the band gap to the next empty of partially filled Brillouin zone. This makes it possible to predict which compounds may make quasicrystals when swapping constituents from existing quasicrystals to make new materials. Based on this method new quasicrystalline phase was discovered with a composition of $Cd_{5.7}Yb$ [41]. X-ray diffraction reveals diffraction peaks that can be attributed to icosahedral symmetry using the indexing method proposed by Elser [42], exhibiting primitive icosahedral lattice. Both Cd and Yb are divalent, with e/a of the quasicrystal being 2.0, adhering to the valence concentration condition. The surface study of the Cd-Yb system is however, hindered by the high vapour pressure of Cd.

Takakura et al [43] have calculated a complete model structure for i-Cd-Yb, which also supplies a model structure for i-Ag-In-Yb. This was the first time a complete model was calculated for any species of quasicrystal.

1.2.2 - The icosahedral Ag-In-Yb quasicrystal

Guo *et al.* replaced the Cd component with equal amounts of Cd's neighbours in the periodic table, namely Ag and In [44]. Substituting Cd in this way creates a compound which still adheres to the Hume-Rothery conditions above. Silver in monovalent while In is trivalent, so in equal parts the new material will have 2 free electrons per atom. In regards to atomic sizes, $d_{Cd}=0.314$ nm, $d_{Ag}=0.290$ nm and $d_{In}=0.332$ nm. This gives an average size of Ag-In of 0.311 nm meaning the overall difference in size of Cd and its replacement is just 1%. The proportion of Yb remains unchanged and we find that the new material has a composition of $Ag_{42}In_{42}Yb_{16}$.

It is this non-aluminium based icosahedral quasicrystal which is the focus of study here. In particular we examine the growth of Pb on its 5-fold surface and propose mechanism which allows the prediction of novel epitaxial material phases. We show in this work that the mechanism is not limited to Pb but also applicable to other elements as well.

Because all available bulk quasicrystals are associated with a complex chemistry, it has not been possible previously to separate the influence of quasicrystalline order and chemistry on the intriguing physical properties of quasicrystals. The single element systems presented in this work exhibit quasicrystalline order with chemical simplicity and thus these can be used as model systems to study the impact of quasicrystalline order on physical properties, independent of chemical complexity. As well as this, it is of great interest to compare physical properties such as superconductivity in the case of Pb in its natural periodic form and this quasicrystalline film. An additional bonus of the multi layer structure we form is that a wide range of experimental techniques can now be implemented to exclusively probe the overlayer, without having a contribution from the underlying substrate, which is not possible for a monolayer film.

1.3 - References

[1] Bychkov, Y.A. and Rashba, E.I., 1984. Properties of a 2D electron gas with lifted spectral degeneracy. *JETP Lett.*, 39, pp. 66.

[2] Bychkov, Y.A. and Rashba, E.I., 1984. Oscillatory effects and the magnetic susceptibility of carriers in inversion layers *J. Phys. C: Solid State Phys.* 17, 6039.

[3] S. Datta, S., Biswajit, D. 1990. Electronic analog of the electro-optic modulator *Appl. Phys. Lett.*, 56, 665.

[4] Pacilé, D., Ast, C.R., Papagno, M., Da Silva, C., Moreschini, L., Falub, M., Seitsonen, A.P. and Grioni, M.1., 2006. Electronic structure of an ordered Pb⁄Ag(111) surface alloy: Theory and experiment. *Phys. Rev. B*, 73(24), pp. 245429.

[5] Ast, C.R., Henk.J., Ernst.A., Moreschini, L., Falub, M.C., Pacilé, D., Bruno, P., Kern, K. and Grioni, M., 2007. Giant Spin Splitting through Surface Alloying. *Phys. Rev. Lett.,* 98(18), pp. 186807.

[6] Ast, C.R., Wittich, G., Wah, P., Vogelgesang, R., Pacilé, D., Falub, M.C., Moreschini, L., Papagno, M., Grioni, M. and Kern, K., 2007. Local detection of spin-orbit splitting by scanning tunneling spectroscopy. *Phys. Rev. B*, 75(20), pp. 201401.

[7] Ast, C. R., Pacilé, D., Moreschini, L., Falub, M. C., Papagno, M., Kern, K., Grioni M., 2008. Spin-orbit split two-dimensional electron gas with tunable Rashba and Fermi energy *Phys. Rev. B* 77, 081407(R).

[8] Meier, F., Petrov, V., Guerrero, S., Mudry, C., Patthey, L., Osterwalder, J. and Hugo Dil, J., 2009. Unconventional Fermi surface spin textures in the BixPb1−x/Ag(111) surface alloy. *Phys. Rev. B*, 79, pp. 241408(R).

[9] Moreschini, L., Bendounan, A., Ast, C. R., Reinert, F., Falub, M., Grioni, M. 2008. Effect of rare-gas adsorption on the spin-orbit split bands of a surface alloy: Xe on Ag (111)-(√3× √3) R30°-Bi *Phys. Rev. B* 77, 115407.

[10] Bentmann, H., Forster, F., Bihlmayer, G., Chulkov, E. V., Moreschini, L., Grioni, M., Reinert, F., 2009. Origin and manipulation of the Rashba splitting in surface alloys *Europ. Phys. Lett.* 87, 37003.

[11] Gierz, I., Stadtmüller, B., Vuorinen, J., Lindroos, M., Meier, F., Dil, H., Kern, K., Ast, C. R., 2010. Structural influence on the Rashba-type spin splitting in surface alloys. *Phys. Rev. B* 81, 245430.

[12] Moreschini, L., Bendounan, A., Bentmann, H., Assig, M., Kern, K., Reinert, F., Henk, J., Ast, C. R., Grioni, M., 2009. Influence of the substrate on the spin-orbit splitting in surface alloys on (111) noble-metal surfaces *Phys. Rev. B* 80, 035438.

[13] Singh, S. P., Karmaker, B., 2011. Single-Step Synthesis and Surface Plasmons of Bismuth-Coated Spherical to Hexagonal Silver Nanoparticles in Dichroic Ag:Bismuth Glass Nanocomposites *Plasmonics* 6, 457.

[14] He, B., Ghosh, G., Chung, Y., Wang, Q., 2010. Effect of Melting and Microstructure on the microscale friction of silver–bismuth alloys. *Tribology Letters* 38. 275

[15] Majzik, Z., Rachid, M., Tchalala, M Švec, P Hapala, H Enriquez, A Kara, A J Mayne, G Dujardin, P Jelínek and H Oughaddou 2013 Combined AFM and STM measurements of a silicene sheet grown on the Ag (111) surface. *J. Phys. C.* 25, 225301.

[16] Issi, J.P., 1979. Low Temperature Transport Properties of the Group V Semimetals. *Australian Journal of Physics*, 32, pp. 585.

[17] Shick, A.B., Ketterson, J.B., Novikov, D.L. and Freeman, A.J., 1999. Electronic structure, phase stability, and semimetal-semiconductor transitions in Bi. *Phys. Rev. B*, 60(23), pp. 15484.

[18] Koroteev, Y.M., Bihlmayer, G., Gayone, J.E., Chulkov, E.V., Blügel, S., Echenique, P.M. and Hofmann, P., 2004. Strong Spin-Orbit Splitting on Bi Surfaces. *Phys. Rev. Lett.*, 93(4), pp. 046403.

[19] Hofmann, P., Gayone, J.E., Bihlmayer, G., Koroteev, Y.M. and Chulkov, E.V., 2005. Electronic structure and Fermi surface of Bi(100). *Phys. Rev. B*, 71(19), pp. 195413.

[20] Ast, C.R. and Höchst, H., 2001. Fermi Surface of Bi(111) Measured by Photoemission Spectroscopy. *Phys. Rev. Lett.*, 87(17), pp. 177602.

[21] Hofmann, P., 2006. The surfaces of bismuth: Structural and electronic properties. *Progress in Surface Science*, 81(5), pp. 191-245.

[22] Agergaard,S.,. Sondergaard, C., Li, H., Nielsen,, M. B., Hoffmann, S.V., Li, Z., Hofmann, P., 2001. The effect of reduced dimensionality on a semimetal: the electronic structure of the Bi(110) surface. *New Journal of Physics,* 3, pp. 15.

[23] LaShell, S., McDougall, B.A. and Jensen, E., 1996. Spin Splitting of an Au(111) Surface State Band Observed with Angle Resolved Photoelectron Spectroscopy. *Phys. Rev. Lett.*, 77(16), pp. 3419.

[24] Mirhosseini, H., Henk, J., Ernst, A., Ostanin, S., Chiang, C.T., YU, P., Winkelmann, A. and Kirschner, J., 2009. Unconventional spin topology in surface alloys with Rashba-type spin splitting. *Phys. Rev. B*, 79(14), pp. 245428.

[25] Gierz1, I., Stadtmüller, B., Vuorinen, J., Lindroos, M., Meier, F., Hugo Dil, J., Kern, K. and Ast, C.R., 2010. Structural influence on the Rashba-type spin splitting in surface alloys. *Phys. Rev. B*, 81(24), pp. 245430.

[26] Hofmann, P., 2006. The surfaces of bismuth: Structural and electronic properties. *Progress in Surface Science,* 81(5), pp. 191-245.

[27] Xu, J.H., Wang, E.G., Ting, C.S. and Su, W.P., 1993. Tight-binding theory of the electronic structures for rhombohedral semimetals. *Phys. Rev. B*, 48(23), pp. 17271.

[28] Yang, F.Y., Liu, K., Hong, K., Reich, D.H., Searson, P.C. and Chien, C.L., 1999. Large Magnetoresistance of Electrodeposited Single-Crystal Bismuth Thin Films. *Science*, 284(5418), pp. 1335-1337.

[29] Black, M.R., Hagelstein, P.L., Cronin, S.B., Lin1, Y.M. and Dresselhaus, M.S., 2003. Optical absorption from an indirect transition in bismuth nanowires. *Phys. Rev. B,* 68(23), pp. 235417

[30] Dalmas, J., Oughaddou, H., Léandri, C., Gay, J., Le Lay, G., Tréglia, G., Aufray, B., Bunk, O. and Johnson, R.L., 2005. Ordered surface alloy formation of immiscible metals: The case of Pb deposited on Ag(111). *Phys. Rev. B*, 72(15), pp. 155424.

[31] Dalmas, J., Oughaddou, H., Le Lay, G., Aufray, B., Tréglia, G., Girardeaux, C., Bernardini, J., Fujii, J. and Panaccione, G., 2006. Photoelectron spectroscopy study of Pb/Ag(1 1 1) in the submonolayer range. *Surface Science*, 600(6), pp. 1227-1230.

[32] Ast, C.R., Pacilé, D., Moreschini, L., Falub, M.C., Papagno, M., Kern, K. and Grioni, M., 2008. Spin-orbit split two-dimensional electron gas with tunable Rashba and Fermi energy. *Phys. Rev. B*, 77(8), pp. 081407.

[33] Grushko, B. and Velikanova, T. Ya., 2004. Stable and metastable quasicrystals in Albased alloy systems with transition metals. *Journal of Alloys and Compounds*, 367(1-2), pp. 58 − 63.

[34] Wang, N., Chen, H., and Kuo, K. H., 1987. Two-Dimensional Quasicrystal with Eightfold Rotational Symmetry. *Phys. Rev. Lett*, 59, pp. 1010 − 1013.

[35] Bendersky, L., 1985. Quasicrystal with One-Dimensional Translational Symmetry and a Tenfold Rotation Axis. *Phys. Rev. Lett*, 55, pp. 1461 − 1463.

[36] Ishimasa, T., Nissen, H.U., Fukano, Y., 1985. New Ordered State Between Crystalline and Amorphous in Ni-Cr Particles. *Phys. Rev. Lett*, 55, pp. 511 − 513.

[37] Sharma, H.R., Shimoda, M. and Tsai, A.P., 2007. Quasicrystal surfaces: structure and growth of atomic overlayers. *Advances in Physics*, 56, pp. 403.

[38] Shechtman, D., Blech, I., Gratias, D., Cahn, J., 1984. Metallic Phase with Long-Range Orientational Order and No Translational Symmetry. *Physical Review Letters* 53 (20), pp. 1951.

[39] Tsai, A.P, Guo, J.Q., Abe, E., Takakura, H. and Sato, T.J., 2000. Alloys: A stable binary quasicrystal. *Nature*, 408, pp. 537.

[40] A. Tsai, 2004. A test of Hume-Rothery rules for stable quasicrystals *Journal of Non-Crystalline Solids* 334-335, pp.317-322

[41] Guo, J., Abe, E., and Tsai, A., Stable icosahedral quasicrystals in binary Cd-Ca and Cd-Yb systems 2000. *Phys. Rev. B* 62, pp.14605-14608.

[42] V.Elser, 1985. Indexing problems in quasicrystal diffraction *Phys. Rev. B* 32, pp.4892-4898.

[43] Takakura, H., Gómez, C.P., Yamamoto, A., Boissieu, M.D. and Tsai, A.P., 2007. Atomic structure of the binary icosahedral Yb–Cd quasicrystal. *Nature Materials*, 6, pp. 58.

[44] Guo, J. Q., and Tsai, A. P. 2002. Stable icosahedral quasicrystals in the Ag-In-Ca, Ag-In-Yb, Ag-In-Ca-Mg and Ag-In-Yb-Mg systems *Phil. Mag. Lett*. *82*(6), 349-352.

Chapter 2

Background to Experimental Techniques

Throughout this work, molecular beam epitaxy (MBE) is used to grow thin films of semi metals, namely lead and bismuth, on single crystal and quasicrystal substrates. The techniques of low energy electron diffraction, scanning tunnelling microscopy, photo-emission spectroscopy and medium energy ion scattering are used to characterize the structural and electronic properties of the thin films. In this chapter we examine the principles and theories behind these techniques.

2.1 - Molecular Beam Epitaxy

Epitaxial growth of thin films on surfaces with mismatched lattices is a complex process which is governed by the interplay of kinetics and thermodynamics [1]. The resulting surface is generally not a static place with several kinetic processes occurring dependant on the substrate temperature.

Upon condensing on the surface there are three possibilities for an adatom:

(i) It may bond strongly to the surface and remain trapped, this is particularly likely at certain sites such as step edges or other defects points;

(ii) It may diffuse across a terrace in order to reach a point where its surface energy is minimised, or at least reduced, at which point it will remain fixed, e.g. Diffusion, nucleation etc. which leads to film growth; or

(iii) It may be desorbed and leave the surface, probably ending up contaminating the chamber in some way and causing no end of trouble.
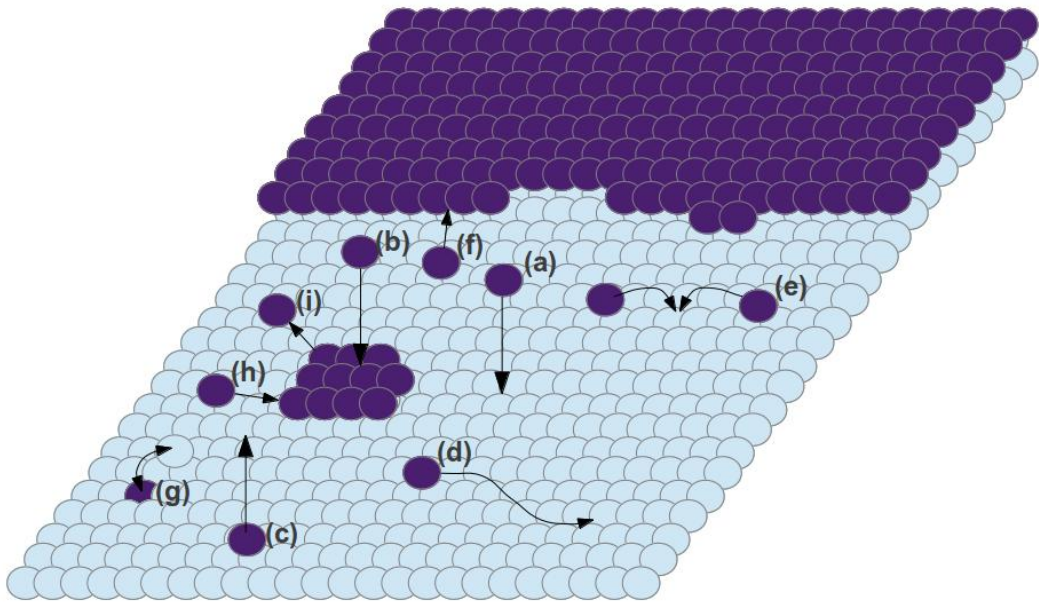
Figure 2.1 – The fundamental atomic processes occurring during epitaxial growth; (a) adsorption on a terrace, (b) adsorption on an island, (c) desorption, (d) diffusion, (e) nucleation, (f) attachment at a step edge, (g) exchange or inter-diffusion, (h) attachment at an island, (I) detachment from an island.

In any of these processes an energy barrier must be overcome. Regardless of which process is energetically most favourable, its rate is governed by what is sometimes called the 'principle of detailed balance' [1]. This is given in the relationship:

$$r = \exp^{(\Delta E/kT)} \tag{2.1}$$

where r is the diffusion rate, ΔE is the difference in energy between initial and final states, k is Boltzman's constant and T is the substrate temperature. The ΔE term for all the different processes is dependent on the atomic details of structure or surface concerned.

We can take an atomistic approach to understanding the growth process and Figure 2.1 illustrates the range of fundamental atomic processes which can occur during epitaxial growth. Which path an atom takes is ultimately determined by its desire to minimise the total free energy as well as its ability to do so i.e. its ability to overcome energy barriers. This in turn is highly dependent on surface temperature with higher temperatures providing more energy to overcome activation barriers. The equilibrium state of a one component system, containing N particles, at a pressure, p, volume, V, and held at a fixed temperature, T, occurs when the Gibbs free enthalpy, G(N,p,T), is minimised.

$$G=F+pV \tag{2.2}$$

where F(T,V,N) is the Helmholtz free energy. From this we can see that as the gas condenses on the surface there will be a reduction in G. This is only part of the story, however, as there are also surface and interface energies to be considered which gives us total energy resulting from the formation of a nucleation centre, ΔG. Hence;

$$\Delta G=\Delta\mu_V+\Delta\mu_S \tag{2.3}$$

where $\Delta\mu_V$ is the cohesive free energy and is negatively proportional to r^3, where r is the radius of the nucleation cluster, and $\Delta\mu_S$ is the surface free energy which is proportional to r^2. This relationship is illustrated in Figure 2.2.

Clearly the relative magnitudes of these terms are based on a complex set of factors dependent on a range of effects including lattice sizes, electronic configurations, etc. but we can see their relationship gives us a critical point beyond which stable island growth occurs (labelled r* in figure 2.2). As coverage increases it becomes increasingly likely that additional atoms will find islands and it follows there is a reduction in
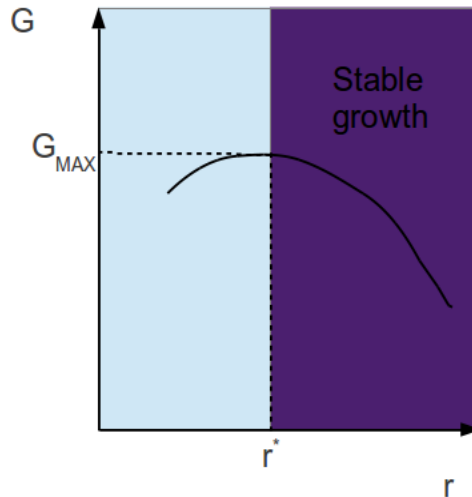
Figure 2.2 – Representation of the critical radius, r^*, where G is a function of r.

nucleation events. This stage of growth is termed the aggregation regime and during this stage the island density remains fairly constant whilst island size increases. This continues up to a point at which the separation between islands is significantly reduced and they begin to coalesce, termed the coalescence regime. During this period island density falls but island size continues to rise.

Rather than this atomistic view of the process, we can take a step back an view the situation from more of a microscopic point. A microscopic point of view can provide a phenomenological description of thin film growth [2]. Broadly speaking, there are three different categories of growth mode, as illustrated in Figure 2.3, below. As to which of the growth modes will prevail depends upon several factors including surface and interface energy, lattice mismatch and the size of the activation barrier.

In cases where the lattice mismatch is small but the bond to the surface is relatively weak the deposited atoms are able to move on the surface and three dimensional island growth is favoured. If the bond is strong then movement of the adatom is restricted and growth tends to be layer by layer. Finally, in the case of a lattice mismatch with a

(a) Layer by layer (Frank-Van de Merwe)

(b) Island Growth (Volmer-Weber)

(c) Layer plus Island growth (Stranski-Krastanov)
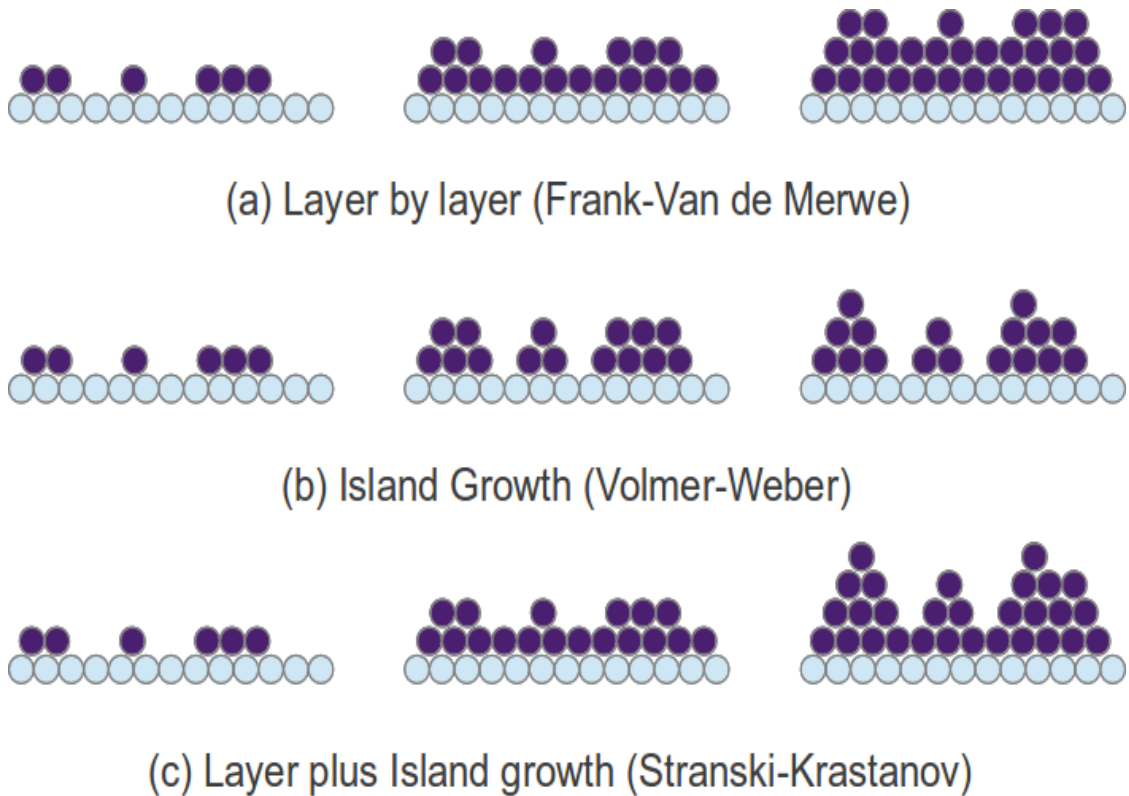
Figure 2.3. Schematics of of three growth modes of a film for different coverage (θ) regimes.

strong bond between substrate and adsorbate growth will initially be layer by layer withthe condensing atoms growing pseudomorphically with the same lattice constant as the substrate. Clearly this lattice mismatch will cause strain on the surface but while the adsorbate layer remains below a critical thickness the strain is absorbed elastically within the structure. Above this critical thickness it becomes energetically favourable for misfit dislocations to form to reduce strain energy at the expense of dislocation energy. At this point the pseudomorphic nature of the overlayer is destroyed allowing for three dimensional island growth on top of the wetting layers.

2.2 - Ultra High Vacuum (UHV)

In order to successfully characterise a surface on an atomic level it is clearly necessary

that the surface remains essentially unchanged throughout the experiment. It is, therefore, advantageous to keep the rate of arrival of any contaminants to a minimum. If we use approximations made by Woodruff [2] for the rates of atoms arriving at the surface, based on his figure of 10^{15} atoms cm^{-2} required for the formation of a complete monolayer it takes 3×10^{-6}s to form a compete layer at 1 torr, 3 s at 10^{-6} torr and almost an hour at 10^{-9} torr. This is somewhat of a worst case scenario and assumes all of the atoms arriving will stick to the surface. It is not uncommon for surfaces of interest to match these conditions, however, so the need for a good vacuum is clear. Furthermore, the presence of atmosphere in the experiment can seriously interfere with analysis techniques. Electrons, for example, have a mean free path in air of around 1 cm. A technique such as Low Energy Electron Diffraction relies on the measurement of electrons diffracted from the sample surface, so it is obvious that the presence of a gas at atmospheric pressure would make the measurements impossible. All of the techniques used in this work were done in UHV conditions.

It seems unnecessary to delve into the finer points of vacuum technology here. Its understanding is not central to the research and it is well documented in many volumes specifically concerned with vacuums and their generation [3].

2.3 - Scanning Tunnelling Microscopy (STM)

2.3.1 Introduction

An STM is used for imaging surfaces at an atomic level. Good resolution is considered to be about 0.1 nm both laterally and for depth. At this resolution, individual atoms within materials can be imaged and manipulated. The technique is suitable for use in vacuum, air and certain liquids and is based on the concept of quantum tunnelling.

2.3.2 The Principle of Operation

Scanning tunnelling microscopy is based around the concept of quantum mechanical tunnelling. It essentially involves an atomically fine tip being brought into close proximity with a conducting/semi-conducting surface with a potential applied between them. Electron wave functions close to the Fermi level leak out of their potential wells with a characteristic exponential inverse decay length, K, given by;

$$K = h^{-1}(2m\varphi)^{1/2} \quad [1] \qquad (2.4)$$

where m is the electron mass and φ is the local work function. When two of these potential wells are brought into close proximity with one another (typically in the region of 4 Å), and a potential is applied between them, it allows tunnelling to occur and a current will flow. Due to the exponential nature of the decay of the electron wave function there is a strong dependence between tunnelling current (I) and sample-tip tip distance (d). This is expressed in the equation;

$$I(d) \propto e^{-Kd} \quad [1] \qquad (2.5)$$

There are typically two modes of operation of the STM, either constant current or constant height mode, shown in Figure 2.4. In both cases the tip rasters across the surface of the sample and either the current is held constant and changes in tip height are measured or the height is held constant and changes in current are measured, thus providing a topographical map of the surface, or more specifically of the density of states.

In constant current mode the tip is brought close to the surface with operating voltages
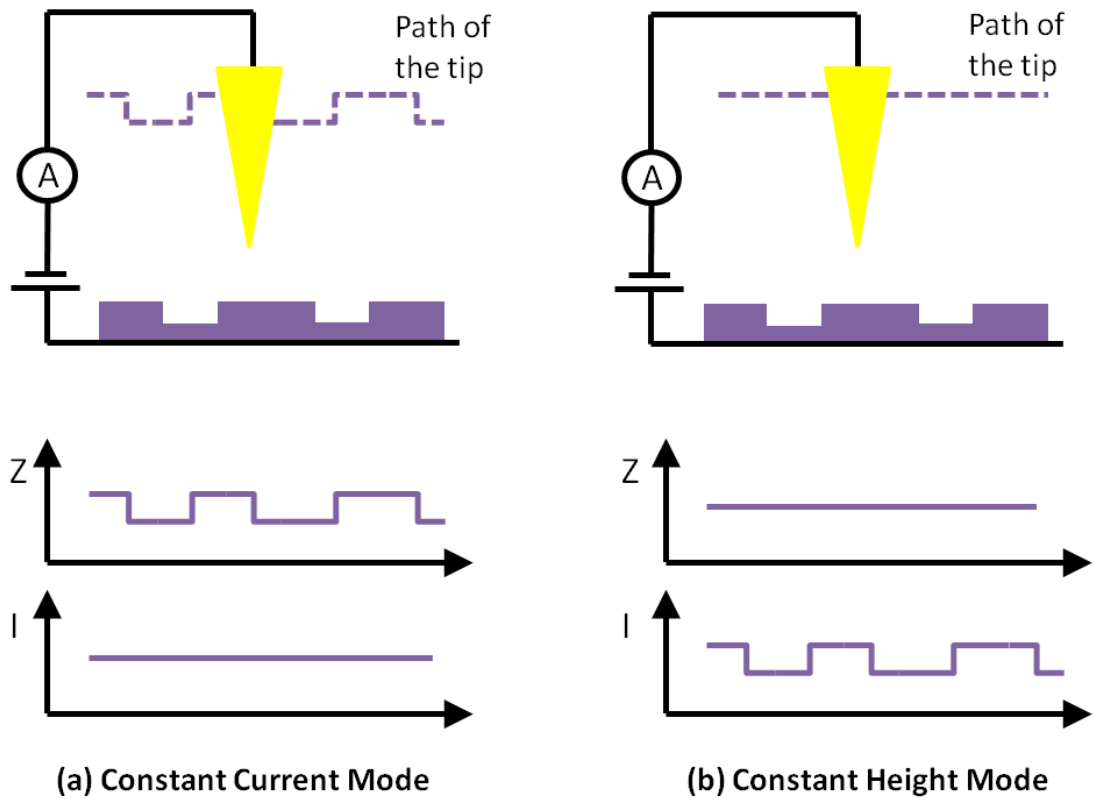
Figure 2.4 - Two operation modes in STM system: (a) constant current mode and (b) constant height mode.

usually in the region of 2mV to 2V, which allows for a suitable tunnelling current to be measured, typically in the nanoamp region. Using a feedback loop, the tip height is varied as is scans across in the x-y plane in order to maintain constant current. Given the relationship between I and d, a plot of dZ as a function of x and y effectively gives the contours of the surface.

In constant height mode the there is no change in the height of the tip and it is a change in tunnelling current which is measured and plotted as a function of x and y position. There are advantages to both methods but constant height mode generally allows for faster scanning.

Although the STM allows us to view surface structures with atomic resolution we must

bear in mind the fact that it is actually a map of electron density of states that is generated rather than of the atoms themselves. In many cases these are one and the same thing, however, quite often this difference can be seen by altering the direction of the potential in relation to tip-surface giving to quite different images of the surface. Furthermore, tunnelling involves states at the Fermi level which may themselves have complex spatial structures and the electronic structures of the tip and surface might combine in a very complex way. The theory of tunnelling doesn't make any distinction between the tip and the surface but in STM the distinction is critical. The STM can also be used to measure the density of states of a sample. This can be done by taking measurements of tunnelling current versus potential while the tip is held at a fixed point or by observing of changes in constant-current topographs with tip-sample bias. This technique is known as scanning tunnelling spectroscopy STS.

2.3.3 – The Microscope

Figure 2.5 shows an illustration of a typical STM setup. An inertial slider is used for coarse movement of the tip allowing different locations of the sample to be scanned. Sensitivity of tip position is critical. Changes in the tunnelling current are fed back, via an electrical circuit, to the scan head which is mounted on arms of a piezoelectric material such as quartz. The application of a voltage to such a material causes its macroscopic dimensions to change and so the height of the tip can be controlled and adjusted. It is the continual changes in the tunnelling current which are measured in order to build up an image of the profile of the surface.

The data collected in this work was done using tungsten tips. These were prepared by chemically etching tungsten wire using sodium hydroxide with a solution concentration of approximately 8g NaOH/100ml distilled water and an applied voltage of 4V. To etch

the tip, the end of the wire was placed in the solution using a Graphite electrode (anode) held about 1cm from the wire. As soon as the end of the tungsten wire dropped off the tip was removed and cleaned in distilled water.
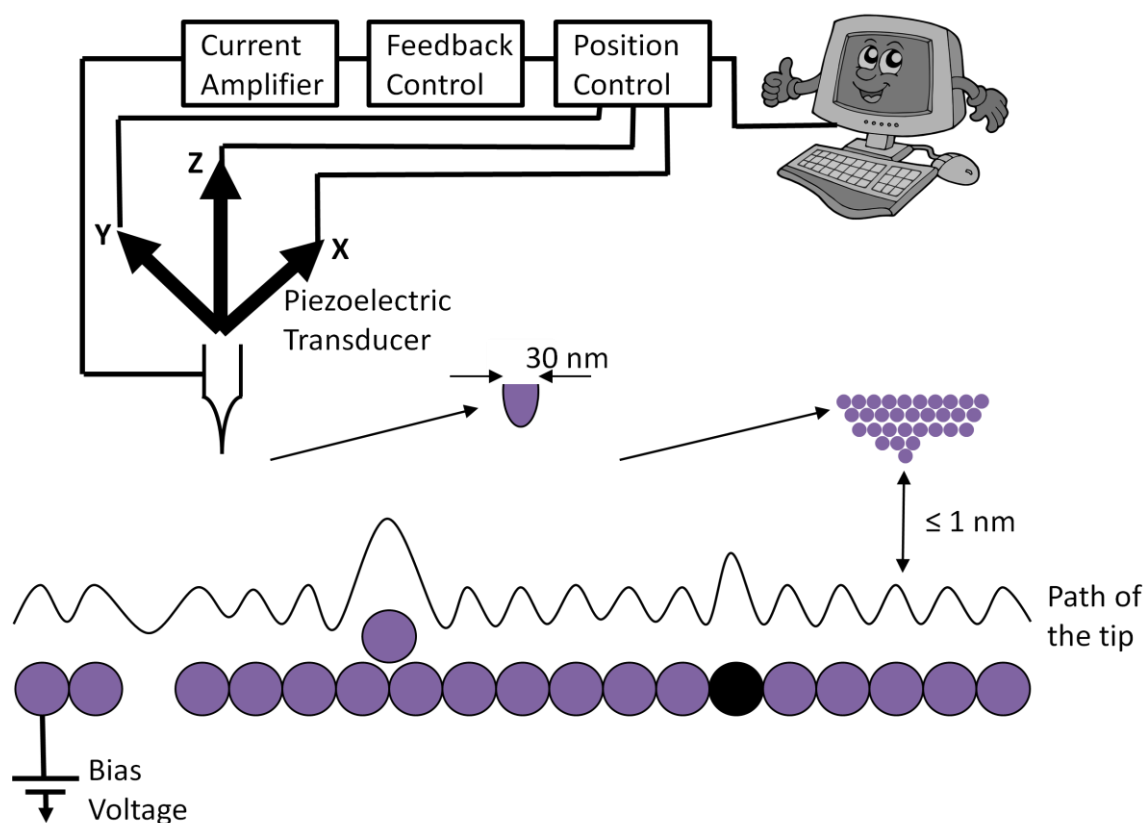
Figure 2.5 - Basic elements of scanning tunnelling microscope.

2.4 - Low Energy Electron Diffraction (LEED)

2.4.1 - Introduction

LEED is a powerful technique for crystal structure determination as well as being a standard technique used to assess the crystallographic quality of a sample. It is used in two ways;

1.   Qualitatively, with the diffraction pattern being recorded and analysis of spot positions providing information on size, rotational alignment and symmetry of a super structure with respect to the unit cell of the substrate.

2.   Quantitatively, with the relative intensities of diffracted beams being recorded as a function of the incident electron beam energy giving I-V curves (intensity vs. energy, eV). These curves can then be compared to theoretically generated curves where the theoretical model is adjusted iteratively to give the best possible correlation.

2.4.2 - The LEED Optic
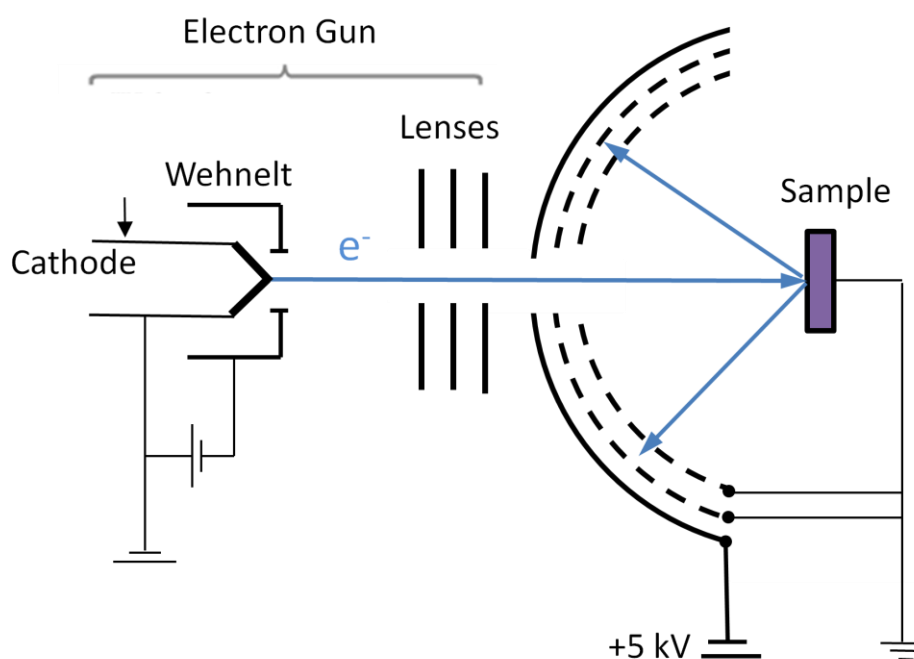
Figure 2.6 - A Schematic drawing of four grids LEED device.

Figure 2.6 shows a typical setup of a LEED optic. A beam of electrons of a well defined energy is directed toward the sample. Typical electron energies are in the range of 30-300 eV although imaging is possible from as low as 10 eV to beyond 500 eV. At these energies the electrons have de Broglie wavelengths ranging from 0.1-0.2 nm, which satisfies the condition for diffraction, namely, the wavelength is equal or smaller

than the atomic spacing. Electrons within this energy range have inelastic mean free paths of around 5-10 Å, which is equivalent to a few atomic layers. This means that LEED is a highly surface sensitive technique.

As well as elastically-scattered electrons, there are secondary electrons leaving the surface which may account for as much as 99% of the total flux. In order to filter these out, a series of grids are set between the sample and the screen. Only spherical fields around the sample are allowed in order to avoid distortion of the electron waves. The first grid, closest to the sample, screens the space around the sample from the retarding field. The second grid is held at a small negative potential to block lower energy secondary electrons and a third grid is often, also held at a negative bias in order to make the field homogeneous and mechanically stable. The potential on these grids can be adjusted to optimally filter out the 'background noise' whilst leaving the diffraction spots as bright as possible. A fourth grid held at ground is sometimes included to act to shield the screen from the field, allowing the current at the screen to be measured.

Finally, the screen is held at a high potential, in the order of 5 kV, to accelerate the electrons to a high enough energy to excite the fluorescence in the screen so that a pattern of LEED spots can be seen.

The LEED pattern displayed on the screen gives information about the surface structure in reciprocal space from which the atomic structures of the sample may be determined. Ideally the LEED pattern should have sharp diffraction spots with a low background intensity providing as great a contrast as possible. An increased background signal can be indicative of a poorly ordered surface or poor crystalinity due to scattering from defects.

2.4.3 - Basic Theory of LEED

LEED relies on the concept of wave particle duality, whereby the electrons may be considered as both waves and particles. The electron beam can be considered as a series of electron waves which are scattered from the atoms of the sample surface. The electron wavelength is given by the de Broglie relation :

$$\lambda = h / p \tag{2.6}$$

where λ is the wavelength of the electron, h is Plank's constant and p is the momentum of the electron. The momentum can be rewritten as

$$p = m.v = (2m.e.V)^{1/2} \tag{2.7}$$

where m is the mass of the electron (kg),v is the electron velocity (ms^{-1}), e is the electronic charge and V is the energy of the electron (eV). From this it is easy to show that the wavelengths used in LEED measurements are comparable to typical inter atomic spacings.In order to explain the basic principle it is easier to consider a two dimensional situation in which electrons are scattered off a single layer of atoms as shown in Figure 2.7.
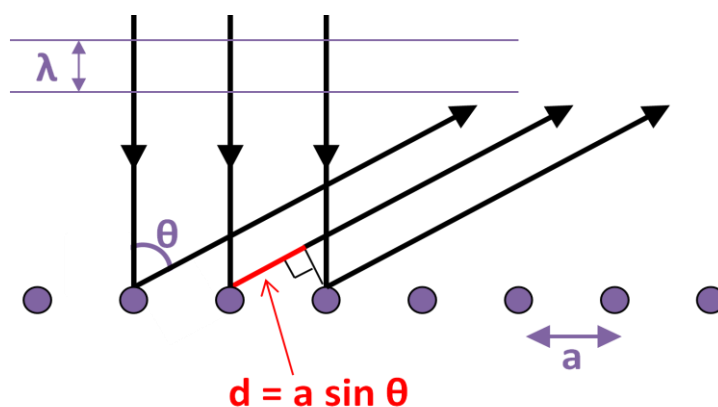
Figure 2.7 – 2D representation of electrons scattered from a surface.

Let us consider a wave arriving at a normal incidence to the surface before being scattered. We can see from the diagram that the backscattered wave front, at some angle, θ, will have a path difference, d, which is the difference in the distance the wave must travel from each atom.

The path difference is $a \sin \theta$ and if this is equal to an integral number of wavelengths, i.e.

$$d = a \sin \theta = n \lambda \quad \text{(where n is an integer)} \tag{2.8}$$

then there will be constructive interference between the wavefronts. This corresponds to a bright spot on the screen of the LEED optic.

To see how this translates to a three dimensional situation, Figure 2.8, below, shows the topmost layer of atoms from a sample with a 2x2 layer of ad atoms on the surface (left) and the LEED pattern generated from this surface (right).
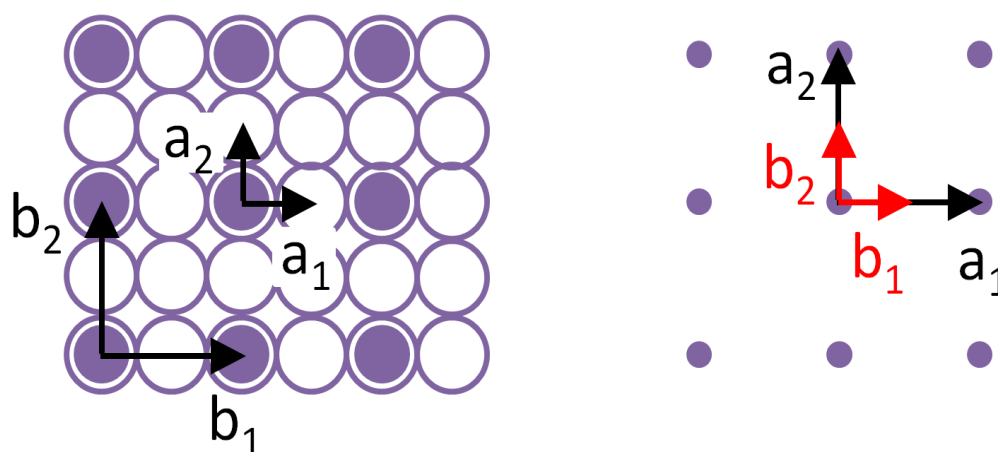
Figure 2.8 - topmost layer of atoms from a sample with a 2x2 layer of ad atoms on the surface (left) and the LEED pattern generated from this surface (right).

The relationship between the unit vectors of the sample and of the LEED pattern, which is in reciprocal space, is given by the equation;

$$A = 2\pi/a \qquad (2.9)$$

So from relatively simple analysis of the diffraction pattern, the size of the lattice spacing, symmetry and rotational alignment of the substrate and the reconstructed surface can be determined.

We have seen how the image can yield qualitative information but the diffraction image can also give a quantitative analysis of LEED experimental data. This is done using the I-V curves for as many of the inequivalent diffraction spots as possible. The section above describes the basic principles of diffraction but there is a further factor not yet mentioned. When the electrons are scattered from the atoms of the crystal there is a complex interaction between the scattered electron and the electrons of the atom. This gives us what is termed the 'form factor'. A form factor, generally, is a function that gives the properties of a certain particle interaction without including all of the underlying physics. In the case of LEED diffraction, even a small change in the electronic configuration will have a significant effect on the fit of the I-V curve. Figure 2.9 shows the curves for two surface alloys, one of Pb on Ag(111) and one of Bi on Ag(111). Even though the positions of the atoms are almost identical in both cases, the presence of an additional electron in Bi compared with Pb changes the electronic configuration and hence causes a different phase shift in the scattered electron. Due to this fact, the technique can be used to identify not only atomic positions but the type of atom as well.
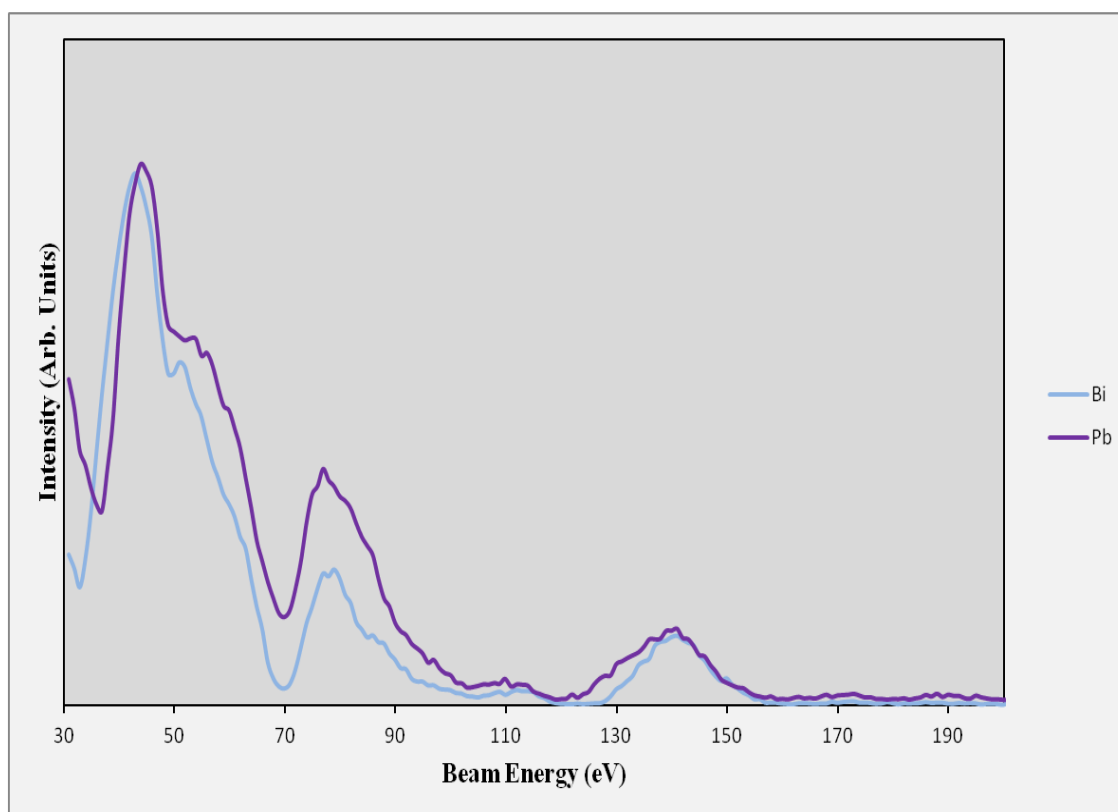
Figure 2.9 – I-V curves for the 1/3,1/3 spots for Pb on Ag(111) and Bi on Ag(111) at 1/3 ML coverage.

The technique of LEED I-V generally involves the use of a CCD camera to record the diffraction patterns as the electron energy is changed at set intervals. The images are stored to computer and then the intensities of the diffraction spots are extracted from the data. The I-V curves are then compared to computer generated, theoretical curves based on a given model structure. The calculations involve multiple scattering of the incident electrons which factor in the amplitudes and phase shifts of the wave as it scatters from individual atoms and the amplitudes of thermal oscillations of the atoms as reflected in Debye temperatures. The most commonly used method to compare the experimental and theoretical data is the Pendry reliability factor. $L(E) = I'/I$. [4]

The R-factor is then given by:

$$R = \sum_g (Y_{gth} - Y_{gexp})^2 dE / \sum (Y_{gth}^2 + Y_{gexp}^2) \; dE \; [4] \qquad (2.10)$$

where $Y(E) = L^{-1}/(L^{-2} + V_{oi}^2)$ and V_{oi} is the imaginary part of the electron self-energy. In general, $R_p \leq 0.2$ is considered as a good agreement, $R_p \leq 0.25$ is considered mediocre and $R_p \leq 0.3$ is considered a poor agreement. The fit is an iterative process using the Tensor LEED code. The model is incrementally adjusted and the new theoretical curves are compared to the experimental and so on until there is maximum agreement between the two data sets.

2.5 - Photoelectron Spectroscopy (PES)

2.5.1 Introduction to PES

Photoelectron spectroscopy is based on Einstein's photoelectric effect. The technique is used to study the energy levels of atomic core electrons, primarily in solids. Ionization energy is provided by photons with energy ranging from tens to thousands of eV. Regardless of the energy of the incident photon, all photoelectron spectroscopy involve the general principle of surface analysis by measuring energy the electrons ejected from the surface.

2.5.2 Basic principle

Ionising radiation imparts energy to an electron as it is absorbed. If enough energy is imparted then the electron may break the bonds confining it to an atom and the resultant ejected electron is termed a photoelectron. Photoelectron spectroscopy involves looking at the energy distribution of these electrons.

The technique can be split into three categories depending on the photon energy used. At the lower energy range is Ultraviolet photoelectron spectroscopy (UPS) and above this range is XPS which utilises X-ray emissions. XPS is split into two categories. For energies below 2000 eV it is termed s-XPS where the s indicates the use of soft X-rays
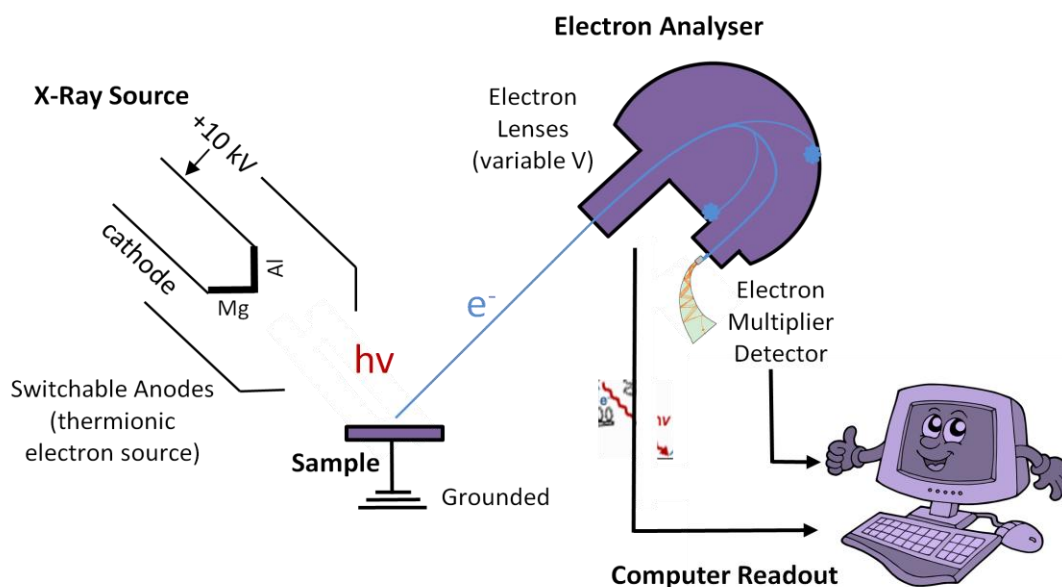
Figure 2.10 Photoelectron spectroscopy setup.

and above this, in the range of hard X-rays, it is usually simply referred to as XPS. Figure 2.10 shows the basic setup of an XPS system with the three main components; photon source, sample and analyser. There is also a need for UHV as to avoid any scattering of the photoelectrons.

Essentially the energy of the ejected electron is the energy of the photon less the energy required to break its bonds from its neighbours and escape from the surface. The incoming photon has an energy given by hv and in order to escape, the electron must overcome its binding energy as well as the workfunction of the surface. Therefore we have the relationship;

$$K.E. = h\nu - BE - \varphi \qquad (2.11)$$

Where K.E. is the kinetic energy of the photo electron, BE is the binding energy and φ is the workfunction. A schematic representation of the process is shown in Figure 2.11. By measuring the energy of the electron we can easily find out the energies of occupied energy levels within the material. Every element and material has a unique set of energy levels allowing the identification of the composition of the material and information about its chemical state. In this sense the technique is analogous to 'fingerprinting' the material.
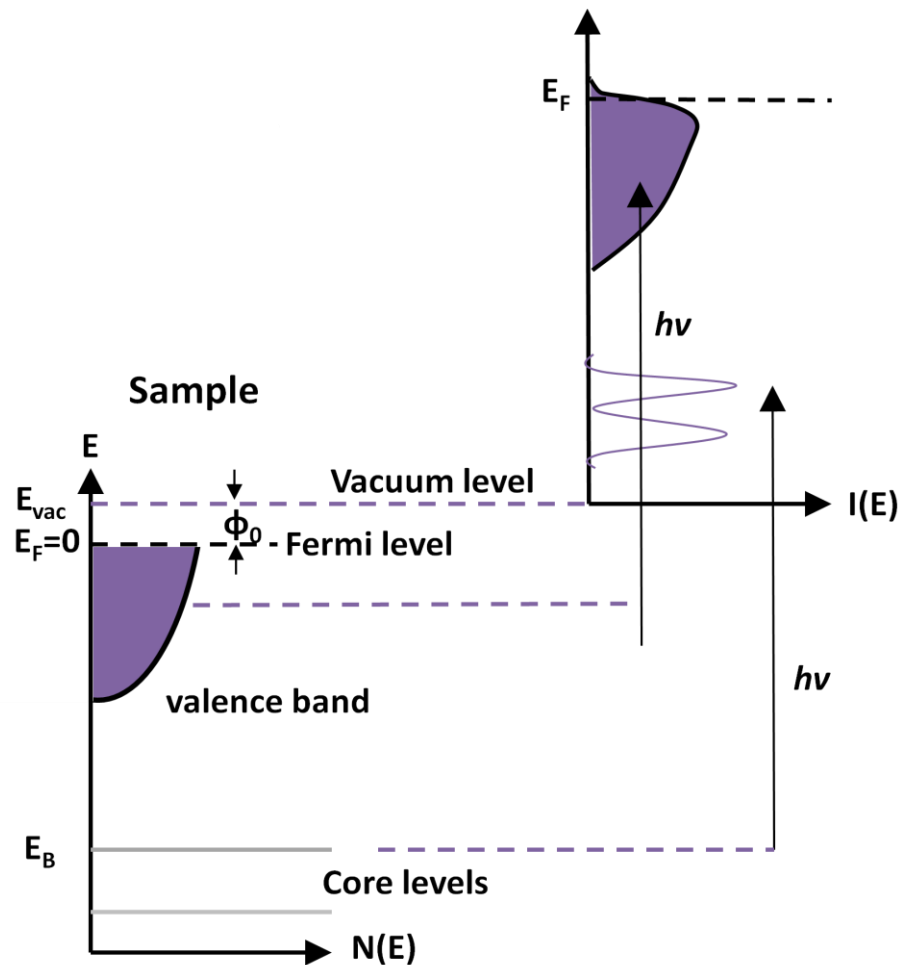
Figure 2.11 - Schematic of energy levels.

2.5.3 Analysis depth

Photoemission spectroscopy is a surface sensitive technique. The depth sensitivity is primarily due to the mean free path of electrons in a material. The process is complex and dependant on the interaction between the photoelectron and the electrons in the material. The escape depth is essentially proportional to e^{-1} and the intensity of electrons emitted from a surface (I) is affected by the depth of material through which an electron must travel (d) and its wavelength (λ). It can be expressed as;

$$I \propto e^{(-d/\lambda)} \tag{2.12}$$

As a general rule, about 65% of electrons emitted originate from less than a distance of λ from the surface and 95% from within 3λ.

By comparing with known values, the thicknesses of an overlayer may be calculated although where the overlayer is of a more complex nature empirical data may not be available.

2.5.4 Photon source

The photon source is one half of the kit used for PES. For accurate measurement of electron energy levels in an atom it is essential to have as narrow a range of photon energies as possible and ideally a monochromated source is best.

Deeper core levels require higher photon energies to liberate the electrons whereas valence electrons typically require less than 20 eV. This means that the study of electrons around the Fermi level can be done with an ultra violet light source whereas the study of closed core shells involves the use of X-rays with energies up to several keV.

Figure 2.12 shows the energy levels accessible using different sources. The most accurate measurements are obtained using a synchrotron light source. Unfortunately this is not a lab based source and usually involves a whole facility dedicated to its use. Lab based X-ray sources can be thought of as operating on the reverse process of PES. In order to generate the X-ray a current is passed through a filament in close proximity to a metal target. The metal target in kept at a high potential, causing thermal electrons from the filament to be accelerated toward it. If these electrons have sufficient energy they can remove core electrons from the atoms in the target. The subsequent holes are then filled by electrons from higher orbits which emit X-rays as they move to a lower core level. X-ray energies created from some common target materials are shown in Table 2.1.
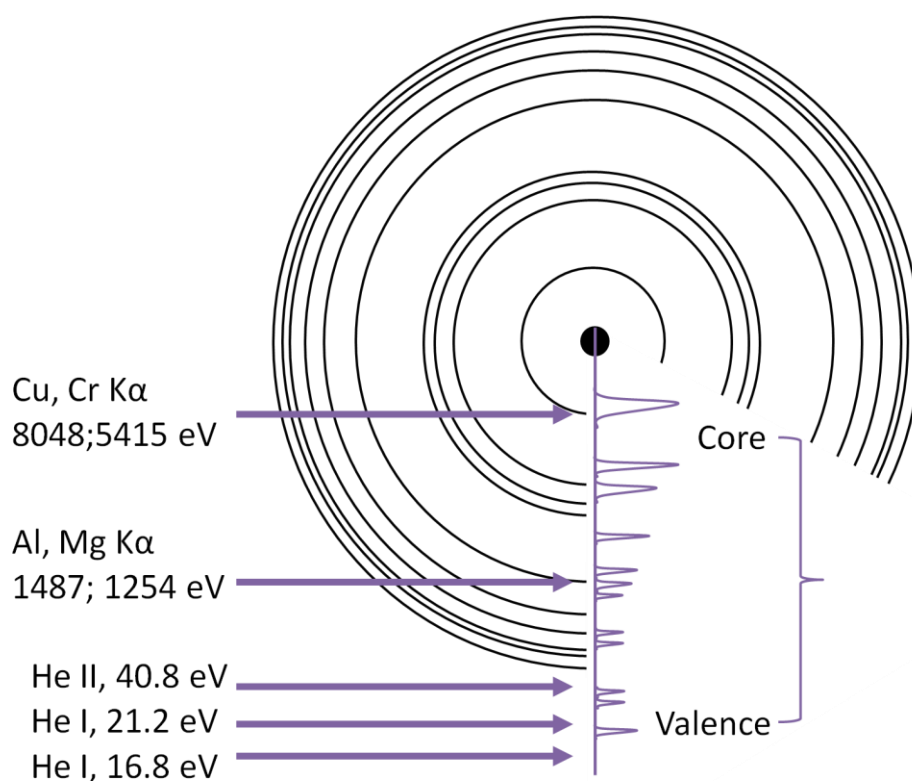
Figure 2.12 - The energy levels of a hypothetical atom, probed by electromagnetic radiation of varying energy.

Element	Energy (eV)	FWHM (eV)
Mg	1253.6	0.7
Al	1486.6	0.9
Si	1739.6	1.0
Cr	5417.0	2.1

Table 2.1 Metal x-ray resonance emission lines. [5].

2.5.5 Electron Analyser

An electron analyser is used to measure the energy of the photoelectrons. There are three methods to measure electron energy; time of flight, acceleration in an electric field and change of orbit in a magnetic field. The focus here is on the method utilising the acceleration in an electric field.

The most popular setup involves the use of a hemispherical analyser although the precursors to this were the cylindrical mirror and cylindrical deflection analysers [6]. Figure 2.13 shows a schematic of a typical hemispherical analyser. The principal advantage of the HSA over other designs is the 180° geometry that allows perfect focus of the electrons without distortion allowing well defined angular and energy dispersion [7]. The function of analyser can be split into three parts. They are the collection, dispersion and the counting of the electrons.

The collection involves selecting the desirable electrons to be counted. With the use of electrostatic lenses, incoming electrons can be deflected, accelerated or retarded in order to focus and collect data from the focal plane of the sample whilst allowing the analyser to be a distance away. In more modern analysers, complex arrangements of
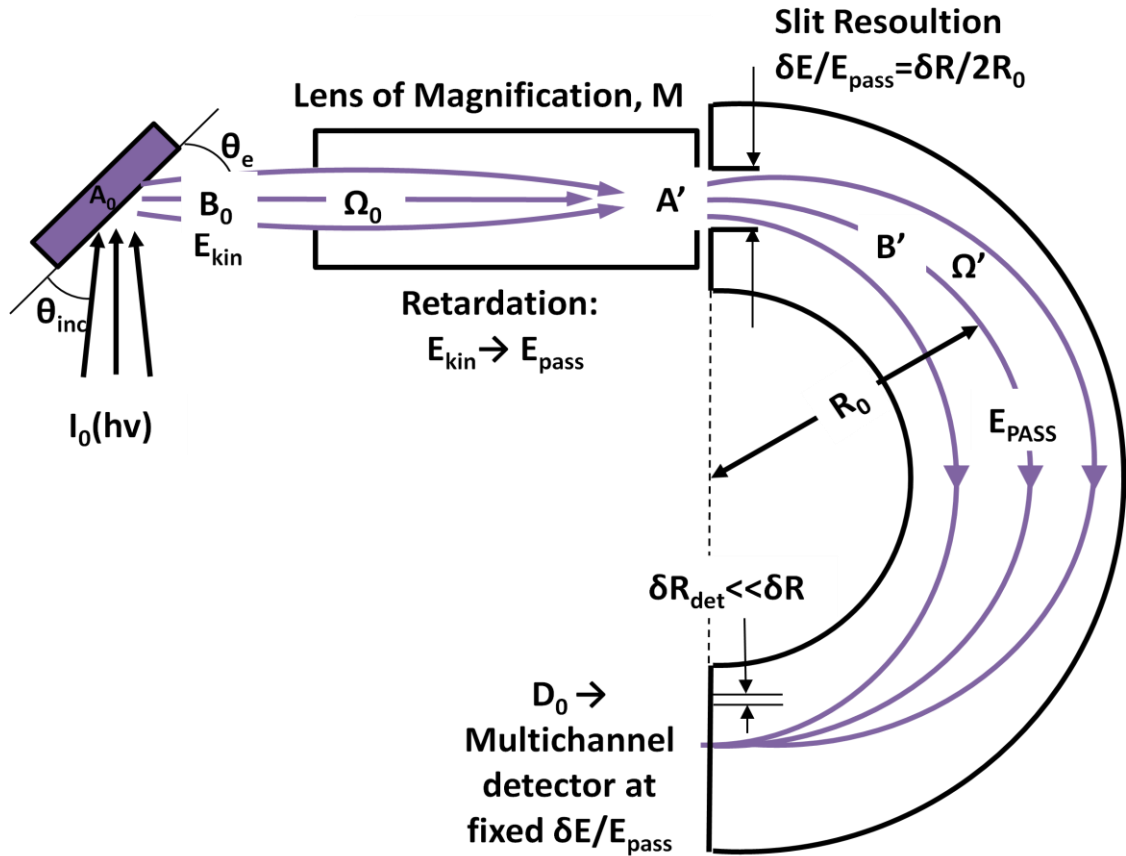
Figure 2.13 - Schematic of the HSA. Top left is the sample producing photoelectrons which are collected by a lens, top centre. Right, are the hemispheres and bottom right is the exit plane with a multi channel detector. A single point detector with an exit slit may also be used.

lenses are used to reduce the area of the sample from which data is collected allowing for analysis of smaller sample or for more local information to be gathered from different parts of a sample.

The electron dispersion in a hemispherical analyser is done by means of two concentric, hemispherical, metal plates. By applying a potential to each of the plates only electrons of certain energies can pass through to the detector. The potential on each plate can be varied in order to select whichever electron energy is desirable. This is given by the relationship:

$$\Delta E = e\Delta V \, (R_{inner}R_{outer}/ \, R_{outer}^2 - R_{inner}^2) = ke\Delta V \, [5] \tag{2.13}$$

Where ΔE is the range of electron energies able to pass through, ΔV is the potential difference between the inner and outer hemispherical plate, R denotes the plate radius and k is a geometrical constant particular to the given analyser. The situation is a little more complex, however, and the analyser's resolution is also dependent upon the energy of the electron with resolution improving at lower energies [8]. For this reason there is normally a retarding field applied before the electron enters between the plates. The field can be varied to adjust the electron energies to an optimal level depending on the energy of interest. At the exit the electron energy is naturally dispersed in one direction and angularly dispersed in an orthogonal axis.

Detection is essentially a matter of counting electrons or more macroscopically, measuring a current. Typically the intensity is measured in terms of counts per second and detectors measure the number of voltage pulses in a given time period. The number of electrons at any given energy is usually very small, to the point where detection is problematic. In order to boost the count rate a channel electron multiplier is used (CEM).

CEMs work using secondary electron emission to increase the number of electrons. They are coated with a material that emits several electrons after an electron collision event takes place. They are usually designed with a large opening, to collect as many incoming electrons as possible, which is connected to a curved tube. By curving the tube of the CEM it increases the likelihood of secondary electrons themselves colliding with the tube to generate yet more electrons and so on until there is a significant amplification of the signal. The basic principle is illustrated in Figure 2.14, below.
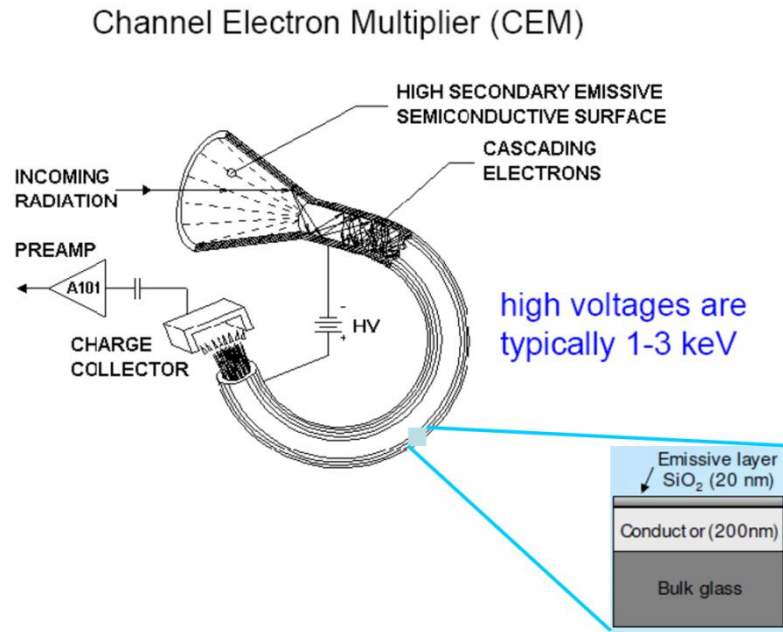
Figure 2.14 – Representation of a typical channeltron configuration. [9]

There is a slit placed in front of the collection device to select the area over which electrons are collected (termed the exit slit). The slit width is variable and defines the energy resolution while the area of the CEM, which is fixed, defines the angular resolution. The electron energy in the exit plane is naturally dispersed and measuring this entire energy window would hugely increase the count rate and reduce collection time. This then shows us the limitation of using a single collection device. It is possible to use multi channel devices to combat this and some analysers have arrays of maybe 5, 9 or even more channeltrons. The limitation here is the physical size of such devices resulting in much of the exit plain being taken up by inter-channeltron space.

In order to measure the entire energy window a microchannel plate (MCP) is used. This is a plate with a high density of small CEMs, an illustration of which is shown in Figure 2.14. The signal gain is not as high as a single channel device although sometimes the plates may be used in series in order to increase this. Position sensitive devices (PSD's)

Figure 2.15 – Illustration of a multichannel plate. [10]

are effectively high-density detector modules suitable for spatially resolved electron counting.

An MCP is a high density collection of small channel electron multipliers housed in a plate, as illustrated in Figure 2.15. Due to their small size, typically 0.5 mm diameter with 12.5 μm spacing, the gain is much less than a single channeltron unit and therefore multi-channel plates tend to be used in tandem, producing similar final gains. Position sensitive devices (PSD's) are effectively high-density detector modules suitable for spatially resolved electron counting. A similar device was is also included in the LEED optic in order facilitate a much lower beam energy which was less damaging to certain surface structures.

2.5.6 Resolution

There are three factors which affect the resolution of a PES scan. They are the line width of the source, the inherent line width of the sample and the resolution of the analyser. The full width half maximum (FWHM) of the observed peak is related to these three factors in accordance with the following expression:

$$w_o^2 = w_s^2 + w_x^2 + w_a^2 \tag{2.14}$$

where w_o is the observed FWHM of the XPS core line; w_s is the intrinsic width the core level of the sample; w_x is the FWHM of the x-ray; and w_a is the analyser widening term.

There is nothing that can be done about the w_s term as it is a physical constant of the sample being studied. The size of this term does differ, however, between electron core levels within an atom. The higher energy levels tend to have larger line widths than the deeper core levels, the result of which is that UPS scans have much broader features than those in XPS as UPS is primarily concerned with the valence level electrons. The resolution in UPS is, in fact, dominated by the sample line width with the equipment used throughout this work.

The natural line width of the incoming X-ray is also a physical constant of the X-ray source. Different materials generate different characteristic X-rays, however, so the resolution can be improved by the correct choice of anode for a given experiment. Table 2.1 shows the energy and FWHM values for some common materials used in X-ray sources. The line width can also be improved with the use of a monochromator. The monochromatic x-ray system offers narrower x-ray line widths, the removal of x-ray satellite lines and reduction of the Bremsstrahlung radiation. The line width of the

incident x-ray is reduced and so an improved energy resolution is possible compared to that using a non-monochromatic X-ray. The line width of AlKα is 0.9 eV while the monochromator can produce a line width of about 0.3 eV for Al. The results presented in this thesis were taken without the benefit of a monochromator and so the overall resolution was dominated by the X-ray source.

For a hemispherical analyser the resolution depends both on the geometrical parameters and on the angular divergence of the incoming photoelectrons in accordance with the following expression:

$$\Delta E = E_0 \left(\frac{\omega}{2R_0} + \frac{\alpha^2}{4} \right) \quad [11] \tag{2.15}$$

where ω is the average width of the two slits, R_0 is the radius of the analyser, and α is the incidence angle of the incoming photoelectrons. The $\alpha^2/4$ term can be thought of as a secondary term for the analyser used here as the resolution is dominated by the R_0 term in the expression. In general, increasing the radius of the analyser improves resolution although technical difficulties arise due to size, limiting the actual sizes possible.

2.6 - Medium Energy Ion Scattering (MEIS)

2.6.1 - Introduction

MEIS is a variation of, and developed from, the technique of Rutherford backscattering spectrometry (RBS). MEIS, however, has the advantage of enhanced depth and angle resolution over RBS. Due to the technique requiring a beam of light ions such as H^+ or He^+, it tends to be quite a large scale operation.

2.6.2 - The principles of MEIS

The technique of MEIS relies on a collimated beam of light ions and at a set energy. Usually the ions are H^+ or He^+ with and energy in the region of 100keV. The ions are directed onto the surface of a sample at a known angle of incidence relative to the crystal structure. The energy and angle of departure of the scattered ions is then measured. From this data, information can then be discerned about the mass and depth of the scattering atom as well the crystal structure of the sample.

The interaction between ion and scattering atom can be viewed as a 'billiard ball' collision. The mass of the scattering atom is directly proportional to the energy of scattered ion so by comparing to known values, the type of scattering atom may be deduced.

Similarly, the depth of the scattering atom below the surface may be found, as the rate at which the scattered ion loses energy is proportional to the distance travelled through the sample. Using energy loss alone, MEIS may have a depth resolution as small as 1 atomic layer.
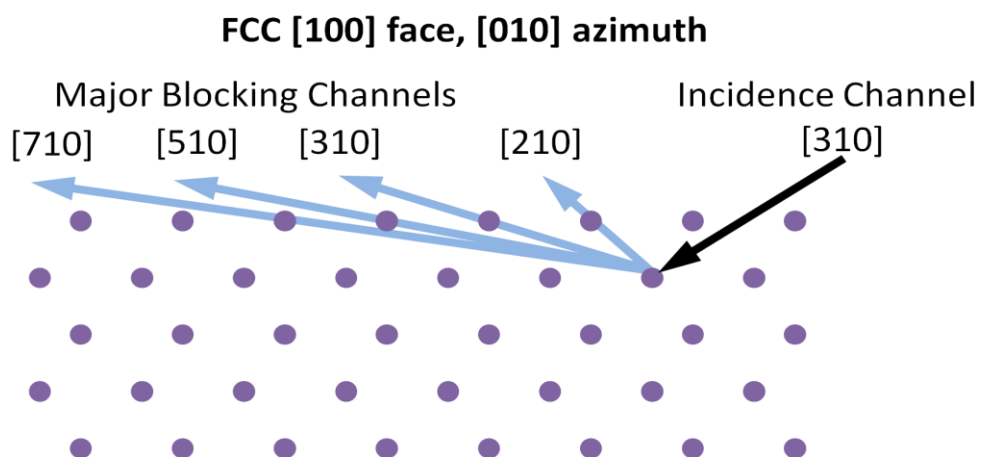
Figure 2.16 - Schematic diagram of surface atoms and scattering geometry.

In order to determine the crystal structure the technique takes data from several crystallographic axes. It relies on the fact that the ions are only able to travel unimpeded through the structure in certain directions, and even then only for a short distance, before they interact with an atom in the sample. Typically the technique can only look about five atomic layers or so into the sample, and even by this depth the information is limited. Figure 2.16 shows some possible paths of an ion through a sample. Depending on the angle of incidence selected the ion may only be able to see the top two or three layers of atoms and the analyser is moved through a range of angles to measure the count rate and ion energy of the scattered ions. As can be seen from the figure, at certain angles, atoms in the layers above act to block the scattered ions path. A sample set of data is shown in Figure 2.17. The drops in count rate correspond to blocking channels due to the position of atoms in the surface of the sample.

A complete determination of the surface structure involves computer modelling of blocking spectra from several scattering geometries. The experimental data set is compared to a set generated theoretically from a model. This was done using VEGAS, a computer programme using Monte Carlo scattering in order to simulate MEIS curves for given structures. Comparisons between these and MEIS experimental results are used for structure determination. An R factor made from chi-squared calculations was to quantise the agreement between the two data sets:

$$R_\chi = \left(\frac{1}{N}\right)\sum_i^N \left\{\frac{(I_{\exp} - I_{theory})^2}{I_{\exp}}\right\} \qquad [12] \qquad (2.16)$$

It is then an iterative process involving adjustment of the model in order to obtain the best fit.
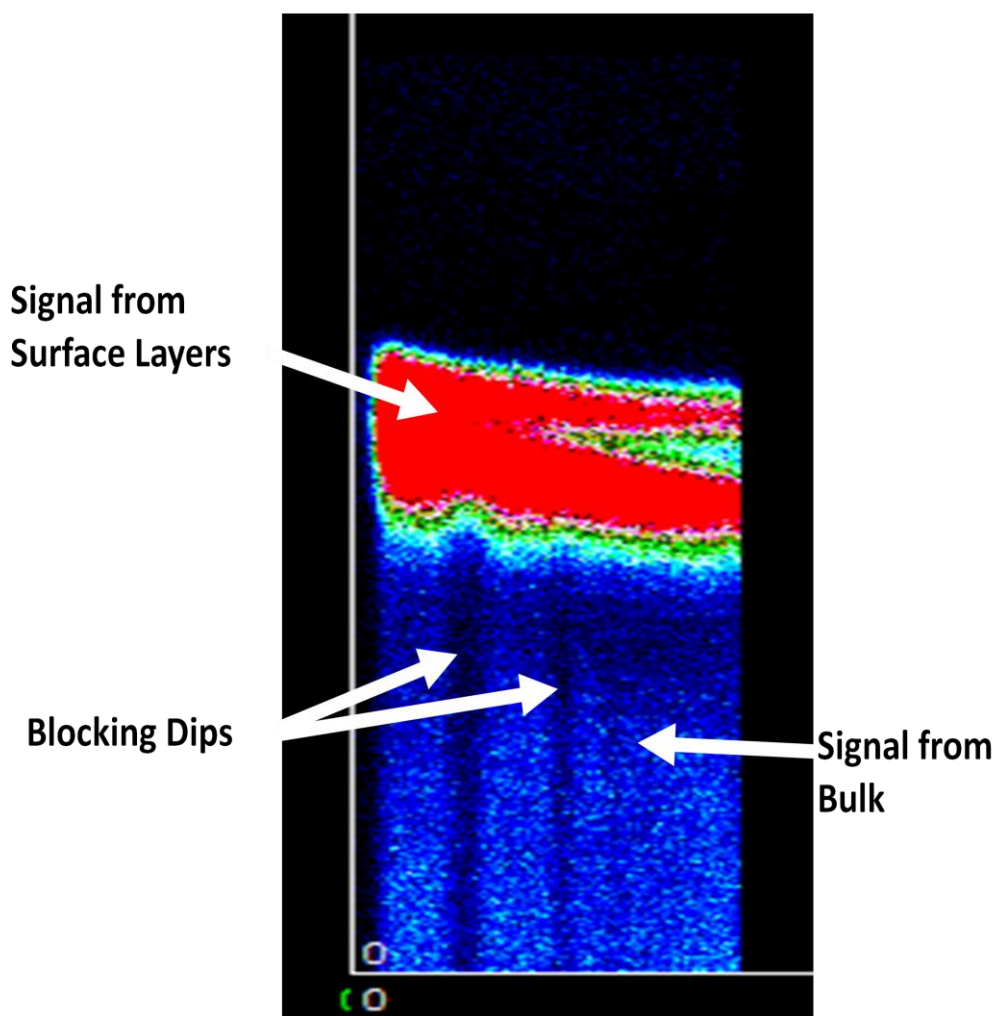
Figure 2.17 – Sample angular energy spectrum from MEIS scan of Pb/Ag(111) 1/3 ML coverage with the incident beam in the (110) direction.

2.7 – Equipment and Setup

With the exception of the MEIS work, all of the techniques were performed at the University of Liverpool and were housed in a single ultra high vacuum system. The system consisted of three chambers, each of which could be isolated by means of a gate valve and independently pumped. The system is shown below in Figure 2.17. Base pressure was 1×10^{-10} mbar and was maintained using a combination of ion pumps and turbo molecular pumps.
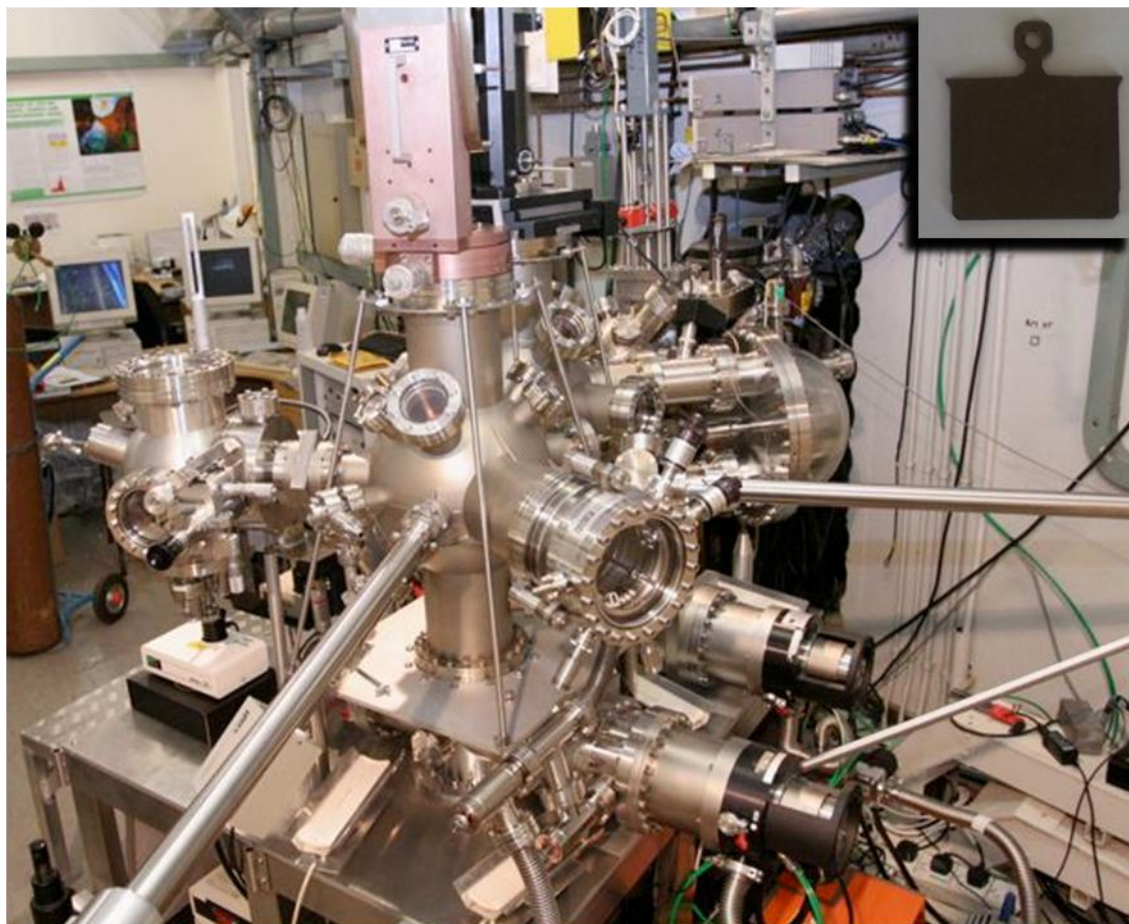
Figure 2.18 – UHV system in the Nano Technology Laboratory, University of Liverpool

The system was fitted with a fast entry lock enabling the admittance of samples into the system without the need to break vacuum in the chambers. The samples were mounted on omicron style sample plates, shown in the inset in Figure 2.18, and could be moved between chambers by means of a magnetically operated transfer arm. Both the preparation and analysis chambers housed ion guns which were used for sputtering the samples by means of bombardment with argon ions. Manipulators were used to hold the sample plates and were able to move in the X-, Y-, and Z- directions as well as rotate the samples through 360° about the Z- axis. They were also equipped for heating and cooling the samples. Heating was performed using a filament mounted in close

proximity to the rear of the sample and heated the sample by means of radiation. Cooling of the sample as done by passing nitrogen in a thin pipe through a reservoir of liquid nitrogen and then through a copper block which was mounted on the manipulator, to the rear of the sample. Using these methods, sample temperatures could be varied in the range of 120-1200 K. Deposition of both Pb and Bi was done using a Knudsen Cell with a quartz microbalance to monitor the flux of the beam. Coverages for the $\left(\sqrt{3} \times \sqrt{3}\right)R30°$ structures were calculated using a combination of LEED and XPS. Pb and Bi were deposited at a known flux rate and length of time. The structure was deemed fully formed at the point when the LEED image showed a clear $\left(\sqrt{3} \times \sqrt{3}\right)R30°$ image and the addition of any extra material lead to the formation of additional spots not consistent with the structure. The surface was also checked with XPS to see the magnitude of the shift in binding energy of Pb or Bi as it had been determined that the formation of the alloy structure caused their 4f peaks to shift to lower binding energies. Once the structure was completely formed the relative ratios of Pb or Bi to Ag were measured and used to determine coverage in subsequent experiments. In Chapters 3 and 4, which look at the dealloyed structures formed at higher coverages, 1 ML is defined as 1 atomic layer of Bi(110), i.e., 9.3×10^{14} atoms cm^{-2}. In Chapters 5-7 which are concerned with the $\left(\sqrt{3} \times \sqrt{3}\right)R30°$ surface alloy structures, 1/3 ML refers to the coverage at which the structure is fully formed and a Bi or Pb atom is found to replace one top layer Ag atom in each unit cell, forming a substitutional BiAg$_2$ surface alloy.

The STM was an Omicron UHV STM 1 is housed in its own, dedicated chamber. The microscope features eddy current damping and allows UHV sample/tip exchange.

The X-ray source and analyser were made by PSP Vacuum Technologies. The analyser radius was 120mm with full 180 degree deflection angle, fringe field correction by Jost electrodes, fully magnetically screened m-metal lined vacuum housing and 5 MCD channels.

The MEIS data was taken at the Daresbury Laboratory. Again, the experiments were performed in UHV conditions with a base pressure of $1x10^{-9}$ mbar. Hydrogen (H+) ions accelerated to produce incident scattering energies within the keV scale. The size of the beam was controlled using an aperture placed in front of the sample and the flux of ions the sample received was measured using an integrated current which was detected at the sample.

More specific experimental details are given in the results chapters.

2.8 - References

[1] Bechstedt, F. 1965. *Principles of Surface Science.* Springer, Berlin, Germany, pp.46.

[2] Woodruff, D. P., Delchar, T. A. 1994. *Modern Techniques of Surface science – Second Edition* Cambridge University Press, Cambridge, UK, pp.5.

[3] Vickerman, J. C., Gilmore, I. S. 2009. *Surface Analysis : the Principal Techniques* Chichester : Wiley

[4] Heinz, K., and Besold, G. 1983. Comparison of Zanazzi-Jona and Pendry reliability factors over an extended energy range. *J. Phys. C: Solid State Phys.* 16, pp. 1299.

[5] Watts, J.F., and Wolstenholme, J., 2003. *An introduction to surface analysis by XPS and AES.* Chichester: Wiley. pp. 212.

[6] Hüfner, S., 2003. *Photoelectron spectroscopy. Principles and applications.* 3rd ed. Berlin:Springer.

[7] Kevan, S.D., 1983. Design of a high-resolution angle-resolving electron energy analyzer. *Review of Scientific Instruments*, 54(11), pp. 1441-1445.

[8] Helmer, J.C., and Weichert, N. H. 1968. Enhancement of sensitivity in ESCA Spectrometers. *Applied Physics Letters*, 13(8), pp. 266-268.

[9] http://www.docstoc.com/docs/95306562/The-channeltron

[10] Unknown (2012) *MCP Basics.* URL: http://www.photonis.com/en/content/133-ism-mcp-reference-list . [June 2103]

[11] King, G., 2005. *An Introduction to Electron Optics*, Lecture notes taken from: http://es1.ph.man.ac.uk/george-king/gcking.html [August 2013]

[12] Woodruff, D.P., Brown, D., Quinn, P.D., Noakes, T.C.Q. and Bailey, P., 2001. Structure determination of surface adsorption and surface alloy phases using medium energy ion scattering. *Nuclear Instruments and Methods in Physics Research, Section B: Beam Interactions with Materials and Atoms*, 183(1-2), 128-139.

Chapter 3

The Evolution of The Electronic Structure at the Bi/Ag(111) Interface

Studied by Photoemission Spectroscopy

3.1 - Abstract

The growth of Bi on Ag(111) induces different surface structures, including $\left(\sqrt{3} \times \sqrt{3}\right)R30°$ surface alloy, Bi-$\left(p \times \sqrt{3}\right)$ overlayer and Bi(110) thin film as a function of increasing Bi coverage. Here we report the study of electronic states of these structures using photoemission spectroscopy from core-levels and valence bands at room temperature. The *sp*-derived Shockley surface state on Ag(111) is rapidly quenched upon deposition of Bi, due to the strong variation of in-plane surface potential in the Ag_2Bi surface alloy. The core levels of Bi *4f* of the $\left(\sqrt{3} \times \sqrt{3}\right)R30°$ Ag_2Bi alloy and Bi(110) thin film are shifted to lower binding energy by ~0.6 eV and ~0.3 eV compared with the Bi bulk value, respectively. Mechanisms inducing the core level shifts are discussed as due to a complex superposition of several factors. At ~1 ML coverage, a surface resonance state is observed arising from split-off bands from Ag 5*sp* due to change of the surface potential upon Bi overlayer adsorption. Finally the change of work function as a function of coverage is discussed based on a charge transfer model.

3.2 - Introduction

Bismuth (Bi) is a typical group-V element with an atomic electron configuration of $6s^2 6p^3$. The $6s^2$ subshell is rather localized at ~10 eV below the Fermi level and does not have significant contribution to the valence band. The $6p^3$, which just locates at 1-3.5 eV below the Fermi level, is thus the predominant character for the energy bands near the Fermi level. Bismuth crystallizes in the rhombohedra A7 structure (R3̄m space group) with two atoms per unit cell [1]. Each Bi atom has three nearest neighbours at a distance of 3.06 Å, linked through predominantly covalent p^3 bonds, which makes Bi a typical semimetal with a small density of states at the Fermi level [2-3]. However, studies on the low index surfaces of Bi such as Bi(111), Bi(100) and Bi(110) have shown that these surfaces are much more metallic than the bulk with a high density of states at the Fermi level [4-8]. The surface electronic states have been attributed to the spin-orbit (SO) splitting of the bands at the surface due to the breakdown of spatial inversion symmetry perpendicular to the surface (Rashba-Bychkov effect) [9-10]. More interestingly, a Bi induced $(\sqrt{3} \times \sqrt{3})R30°$ surface alloy structure on Ag(111) has received considerable attention, because it exhibits exceptionally large spin-orbit splitting of its surface states [11]. It was predicted that variations of the surface in-plane potential gradient induced by the surface alloy results in the strong enhancement of spin splitting. A giant spin-orbit splitting of quantum-well states has also been observed from Bi monolayer on Cu(111) [12]. Based on first-principles calculations, the authors in [12] argued that the huge spin-orbit splitting results from the potential gradient perpendicular to the surface at the interface of the Bi/Cu(111). Overall, these results indicated that atomic structures of Bi in surface alloy or thin films play a critical role in determining surface potential gradient and thus SO splitting.

On the other hand, studies of growth of metals on metallic substrates have been motivated by the demand for high quality thin film metallic heterostructures with sharp interfaces for technological applications. The growth phenomena however can be much more complex at the atomic scale than that predicted by simple thermodynamic considerations based on surface and interface energies of the metal adsorbate film and substrates. Tersoff [13] has shown that surface-confined alloy phases may arise as an alternative to overlayer structures in systems dominated by an atomic size mismatch, even in cases where the metals are immiscible in the bulk. This is particularly the case for the growth of heavy elements like Bi or Pb on light metals such as Cu and Ag [13-14]. We have recently performed a detailed study of the atomic structures of Bi grown on the Ag(111) surface by scanning tunnelling microscopy (STM), low energy electron diffraction (LEED) and *ab-initio* density functional theory (DFT) calculations, including the $(\sqrt{3} \times \sqrt{3})R30°$ surface alloy, Bi-$(p \times \sqrt{3})$ overlayer and Bi(110) thin films [15-17]. In this paper, we extend these structural studies by reporting on the evolution of electronic states of these Bi structures using X-ray/ultraviolet photoemission spectroscopy (XPS/UPS).

3.3 - Experiments and Calculations

The experiments were performed in a standard ultrahigh vacuum surface science chamber consisting of a rear-view low energy electron diffraction (LEED) optics from OCI Vacuum Microengineering, a PSP Vacuum Technology electron energy analyser (angle integrating $\pm10^{\circ}$), dual anode X-ray source and an un-monochromatised He UV source. The LEED optics was either a low current micro-channel plate based optics in the analysis chamber of the UHV system or a standard LEED optics mounted in the

preparation chamber of the same UHV system. The base pressure of the system was less than 2×10^{-10} mbar, with hydrogen as the main residual gas in the chamber. The Ag(111) surface was prepared by cycles of Ar ion bombardment and annealing to approximately 800 K. The sample was considered clean when the LEED pattern showed sharp integer order spots and XPS did not show any traces of contamination. Bi was evaporated using an Omicron electron bombardment evaporator with an integrated flux monitor. This was used to maintain a constant deposition rate of 0.15 ML/min, which was calibrated using XPS. 1 ML (monolayer) is defined as 1 atomic layer of Bi(110), i.e., 9.3×10^{14} cm^{-2}. The Ag substrate was kept at room temperature during deposition. The XPS measurements were carried out with an Al K-alpha source (1486.6 eV), and the energy resolution at full width at half maximum (FWHM) is about 0.8 eV. The overall resolution in the XPS measurements is of the order of 1 eV, therefore we have not deconvoluted the spectra and only measure the binding energy shifts. UPS measurements were performed with a He-I (~21.2 eV) UV lamp and a sample bias, arbitrarily chosen, of -5.0 V. The overall energy resolution in the UPS measurements was about 0.15 eV, which was determined experimentally with the Fermi edge of Ag(111). The spectrometer was calibrated using Au $4f_{7/2}$ at 83.9 eV. For each spectrum the binding energy is referenced to the Fermi level.

We have also performed DFT calculations using Vienna *ab-initio* simulation package (VASP) [18-19] including the projector augmented wave (PAW) potentials [20]. A kinetic energy cut-off of 400 eV was applied to the plane waves, which was found to produce well-converged results for both Ag and Bi. The exchange correlation potential employed the generalized gradient approximation (GGA) of the Perdew-Wang 91 (PW91) [21]. A $10\times8\times1$ Monkhorst-Pack mesh was used for k-point sampling. Bader charge analysis was used to analyse the charge states of Bi and Ag [22-23].

3.4 - Results and discussion

3.4.1 - Structural evolution of Bi on Ag(111)

The structural evolution as a function of Bi coverage is briefly summarized by LEED patterns shown in Figure 3.1. As mentioned above, previously we have used STM, LEED I-V and DFT to perform a detailed study on the nucleation and atomic growth of Bi on the Ag(111) surface from submonolayer up to 3ML coverage [16-18]. Here we briefly review the
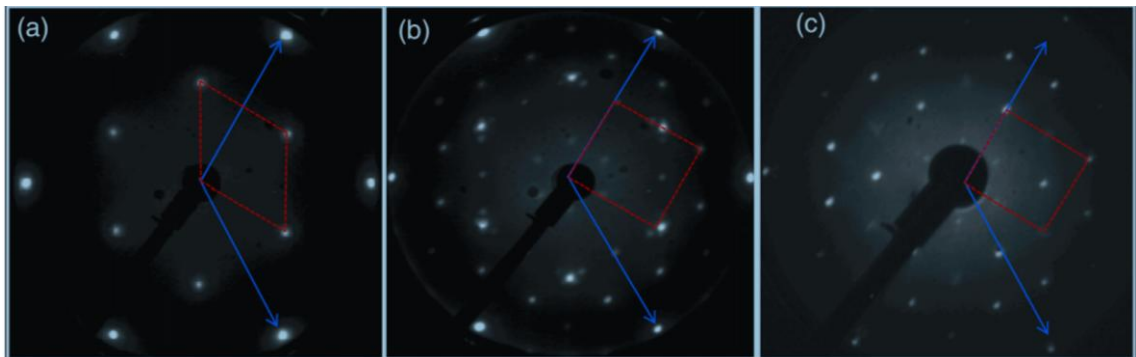
Figure 3.1 - LEED patterns of Bi/Ag(111) surface structures as function of Bi coverage: (a) $(\sqrt{3} \times \sqrt{3})R30°$ Ag₂Bi surface alloy at 0.55 ML (beam energy = 40 eV); (b) Bi-$(p \times \sqrt{3})$ overlayer structure supported on Ag(111) at 0.9 ML (beam energy = 37 eV); (c) Bi(110) thin films on Ag(111) at θ > 1 ML (*beam energy = 77 eV, but with different LEED system*); The unit cell of Ag(111) is indicated by blue line and red dot lines are reserved for different Bi superstructures.

structural evolution of the system. At low coverage (θ < 0.55 ML) deposited Bi atoms can either incorporate into the topmost layer of Ag(111) or react with Ag atoms released during Bi incorporation to form Ag₂Bi alloy embedded or supported on top of Ag(111) surface, referred to as a surface alloying process. At the coverage of θ = 0.55 ML, one atomic layer of ordered $(\sqrt{3} \times \sqrt{3})R30°$Ag₂Bi substitutional surface alloy can

be formed on Ag(111) surface, giving the LEED pattern (beam energy 40 eV) shown in Figure 3.1a. The relief of surface tensile stress of Ag(111) by incorporation of the larger-size Bi atoms into the surface was proposed as a driving force for the surface alloy formation, even though Bi and Ag are not miscible in the bulk phases. When the coverage was increased above 0.55 ML, a surface de-alloying process occurs and the Ag$_2$Bi surface alloy gradually converts into an ordered Bi-$(p \times \sqrt{3})$ overlayer structure supported on Ag(111), which is characterised by the LEED pattern (beam energy 37 eV) shown in Figure 3.1b. The de-alloying process is presumably driven by the high compressive strain induced by incorporation of larger-size Bi atoms into the Ag matrix at a high coverage and the subsequent lack of miscibility of Ag and Bi bulk phases. After completion of the de-alloying process at $\theta = 1$ ML, further Bi deposition leads to Bi(110) thin films grown on top of Ag(111) with a chemically abrupt interface, giving a LEED pattern (beam energy 77 eV) shown in Figure 3.1c.

3.4.2 - XPS measurements

In order to explore the interactions between Bi and Ag(111) at different growth stages, we measured Bi 4f core-level XPS spectra as shown in Figure 3.2a. Bi 4f shows a doublet corresponding to Bi 4$f_{7/2}$ and 4$f_{5/2}$ with a spin-orbit splitting of 5.3 eV. The binding energy of Bi 4$f_{7/2}$ for Ag$_2$Bi (for $\theta < 0.55$ ML) is located at 156.34 eV [24]. Our results show that the binding energy is of this value for θ less than 0.55 ML. This is expected as previous STM results have shown that up to this coverage, only the surface alloy is present on the surface in an ordered structure. With increasing coverage, the binding energy gradually shifts to a higher value and reaches a value of 156.6 eV, (Figure 3.2b), and this is consistent with the de-alloying process that occurs after θ

>0.55 ML. The latter shift is slightly less than the reported bulk value of 156.9 eV [25]. This is reasonable since a large proportion of Bi atoms are located at the surface and Bi/Ag(111) interface. A shift of surface core level binding energy of a few hundred meV is normally observed on metal surfaces as a consequence of the reduced coordination number of surface atoms compared to the bulk atoms [26-27]. For the Bi 4f in the Ag$_2$Bi surface, there is a shift to lower binding energy by ~ 0.3 eV, referred with respect to Bi 4f of Bi(110) film. There are many factors affecting the shift of core level binding energies, including atomic configurations, final state screening and chemical shift [28]. In Ag$_2$Bi surface alloy, Bi atoms embed into the Ag(111) lattice, with each Bi atom surrounded by six in-plane Ag atoms and three Ag atoms underneath. Our recent structural determinations of Ag$_2$Bi alloy by LEED I-V and DFT calculations demonstrated that Bi atoms slightly protrude from the Ag(111) plane and have 0.6 Å outward relaxation [15]. This may result in a reduced effective coordination number of Bi, which gives rise to the lower shift of Bi 4f binding energy. Secondly, electron charge transfer from Ag to Bi seems apparently plausible based on simplistic electronegativity argument, since the electronegativity of Bi is 2.02 eV, while that of Ag is 1.93 eV. However, as discussed in the next section, the change of work function with Bi coverage suggests an opposite electron transfer: from Bi to Ag, which will contradictorily result in an increase of the Bi 4f binding energy. To verify this, we performed DFT calculations using VASP and Bader analysis to analyse the charge states of Bi and Ag. Results show that there is a charge transfer of -0.17|e| from a Bi atom to the surrounding Ag in the $(\sqrt{3} \times \sqrt{3})$ R30° structure. The argument of electron transfer from Bi to Ag is qualitatively in agreement with the recent DFT calculations by Moreshini *et al.* showing that there is -0.82|e| charge transfer from Bi to Ag [29].
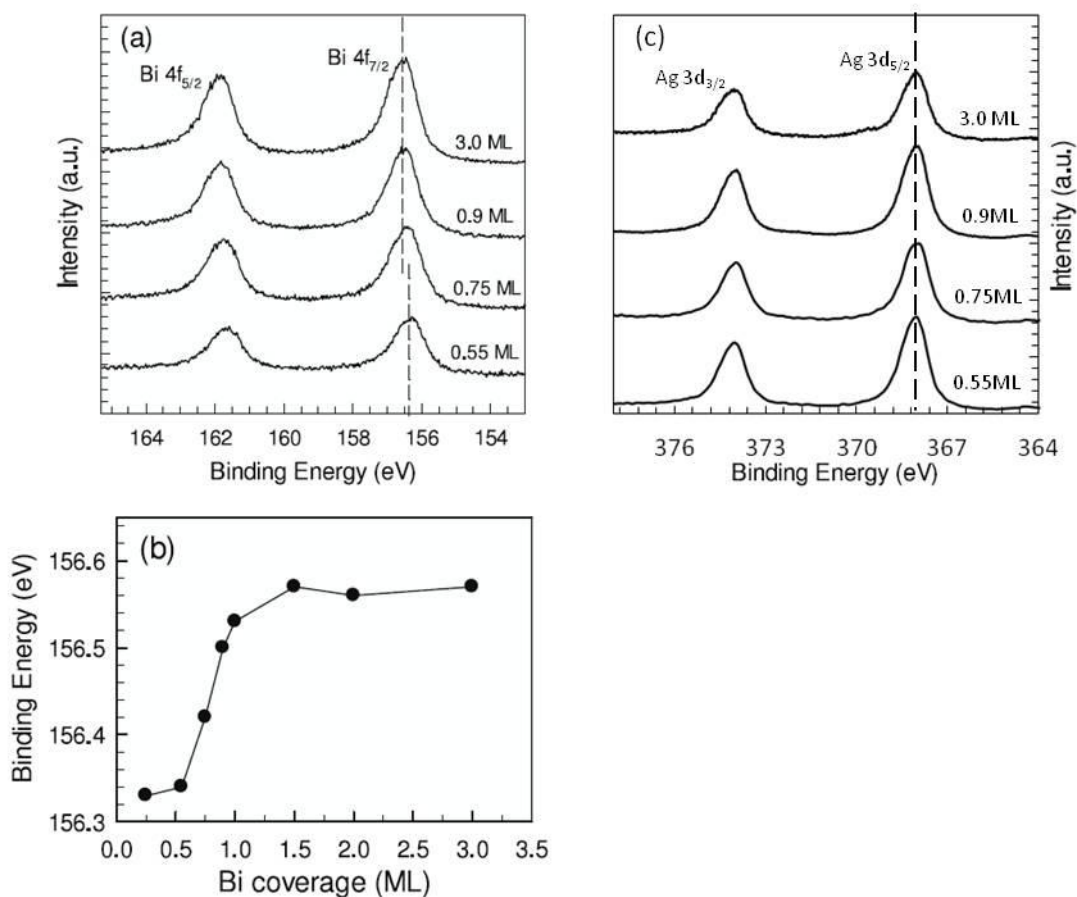
Figure 3.2 - (a) Coverage dependent Bi 4*f* core-level spectra taken by normal emission XPS; (b) change of binding energy as function of Bi coverage; (c) Ag 3d spectra showing no binding energy shift with change in coverage.

The differences in the calculated amounts of charge transfer may result from different atomic relaxations used in the calculations. Nevertheless, the electron transfer from Bi to Ag can induce a reduction in the effective radius of Bi atoms. This could explain the smaller outward relaxation amplitude of Bi (0.6 Å) we observed in the LEED I-V study, compared with the value of 0.84 Å predicted by a simple hard-sphere model based on bulk metallic radii [17]. Lastly, the core hole in Ag_2Bi alloy can be more effectively screened by surrounding free electrons in Ag(111), compared to that of Bi(110) overlayer with more covalent structure, which may be another contribution for

the lower binding energy of Bi in Ag_2Bi. Taken together, it would appear that the core level shift of Bi is a rather complex superposition of the three factors.

3.4.3 - UPS and work function changes

Figure 3.3(a) displays extended valence band spectra of a clean Ag(111) surface and the surface after deposition of 0.55 ML Bi obtained at normal emission, corresponding to Γ point in the surface Brillouin zone. The spectrum for clean Ag(111) is dominated by fully occupied 4d band located at EB > 4 eV with a bandwidth of ~3 eV [30–32], as expected. Weak HeI satellites are present in the HeI radiation He I_β (23.09 eV) and He Iγ (23.74 eV) and these have relative intensities of 1.5% and 0.1% respectively compared to the He I_α line. Background subtraction of satellite structure did not affect the features in the spectra discussed here where we are comparing spectra with respect to that of the clean surface. Therefore, the figure shows raw data, with the weak feature at EB D 2.0–3.5 eV being due to the 4d spectra excited by He I_β (23.09 eV). A broad and flat plateau extending from Fermi energy down to EB ~ 4 eV is derived from indirect transitions from the sp band [32]. Figure 3.3(b) shows expanded UPS spectra in the vicinity of the Fermi level (right panel) and corresponding secondary cutoff energy (left panel) as a function of Bi coverage. The narrow peak (marked as SS) just below Fermi level (E_B D 0:06 eV) on clean Ag(111) is derived from the Shockley surface state [33]. The intensity of this peak decreases rapidly upon Bi deposition. At a coverage of 0.55 ML (red curves), when the surface consists of ordered $\left(\sqrt{3} \times \sqrt{3}\right) R30°$ Ag_2Bi surface alloy,
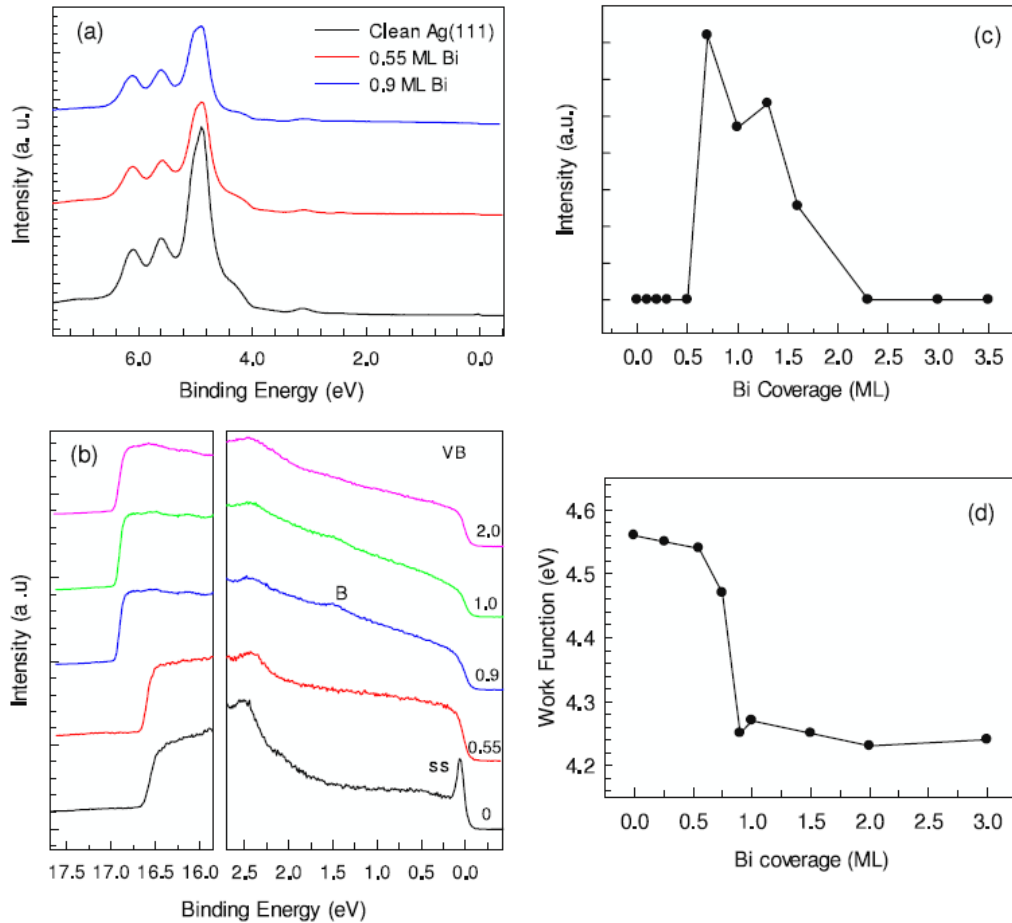
Figure 3.3 - Normal emission UPS valence band spectra of Bi/Ag(111) as a function of Bi coverage: (a) extended region; (b) detailed valence band spectra near Fermi level (right panel); secondary electron cutoff of the photoemissions (left panel). Coverages are indicated in the figure; (c) intensity as a function of coverage of the 'bump' at EB ~ 1:4 eV, ascribed to a surface resonance state of Ag 5sp band; (d) work function as a function of Bi coverage.

the peak corresponding to the Shockley surface state is completely quenched, while instead a clear Fermi step remains. Shockley surface states of Ag are quasi two-dimensional electronic states located in the projected sp-derived band gap along the 0-L line of the bulk band structure, induced by the change of the potential associated with the surface termination. In other words, they appear to be split off from corresponding sp-derived bulk states, with a nearly free electron like (parabolic) dispersion. The Shockley surface states are sensitive to surface

modifications i.e. adsorption of rare gas, metal or molecules, through complex mechanisms of Pauli-repulsion, local potential change, charge transfer and work function change etc [34−36]. Surface alloy formation on noble metal (111) surface often leads to rapid quenching of the surface states, for example Ge and Pb on Ag(111) [37-38], and In on Cu(111) [39]. It has been shown by angle-resolved photoemission spectroscopy (ARPES) and DFT calculations that the Bi atom in the Ag2Bi surface alloy induces a large in-plane potential gradient (possibly accompanied by out-of-plane one due to the outward relaxation of the Bi atom) [11]. The surface electron states are then changed to be dominantly p-like convex dispersion associated with Bi 6p3 valence electrons. The spin degeneracy is in turn strongly lifted by the in-plane gradient of surface potential to give rise to the giant spin–orbital splitting at the Γ point of the surface Brillouin zone [29,40]. The spin split bands cross at about 0.3 eV in normal emission. However, in our measurements we observe a smooth Fermi step with high density of states. This is because our UPS spectra are angle-integrated and the measurements were performed at room temperature. With Bi coverage more than 0.55 ML, Ag_2Bi surface alloy gradually de-alloys into the Bi overlayer on Ag(111). A 'bump' (B) at EB D ~1:4 eV starts to appear. The 'bump' has a maximum intensity at Bi coverage of ~0:9 ML and then decreases as Bi deposition increases above 1 ML (Figure 3.3(c)). It disappears at coverages exceeding 2 ML. Therefore it is reasonable to conclude that this 'bump' originates from electronic states localized at the Ag–Bi interface. Such interface states could have their origin from Ag(111) surface resonance state split off from Ag 5sp band due to change of surface potential by Bi overlayer. Nakagawa et al have performed detailed ARPES studies on the electronic states of heavier p-block metals (which we refer to elements placed at the bottom in group 13−18 in the

periodic table, such as In, Sn, Tl, Pb, Bi) on metal surfaces, such as In/Cu(100) [41] and Bi on Ag(100) [42]. Surface resonance bands running along the edge of the projected sp bulk band have been observed, which can be alternatively understood as split-off bands from metal sp states due to a change of surface potential by In or Bi overlayer absorption. Therefore a similar assignment of the 'bump' as surface resonance states of Ag 5sp band induced by the Bi overlayer is also possible in the current study. Secondly, the 'bump' state may also have its origin from interaction between Bi $6p^3$ and Ag 5sp. The electronic configuration of Bi is 6s26p3. The $6s^2$ subshell is rather deep in energy (called inert pair). The $6p^3$ is just locates at 1–3.5 eV below the Fermi level. Hence, we may infer that interactions at the interface mainly come from Bi $6p^3$ and Ag 5sp, e.g. by hybridization (bonding states) with slight charge transfer as implied by our DFT calculation and UPS work function measurement. We also note that LEED indicates increasing background with coverage, which could be due to disorder in the layer and lead to a decay of the peak. Earlier STM studies [15] had shown well-ordered Bi(110) films but the area probed by LEED and UPS is much larger compared to the STM. The change of work function as a function of Bi coverage is displayed in Figure 3.3(d), deduced from the variation in the secondary cutoff energy in Figure 3.3(b). The measurements were made to an accuracy of ±0:03 eV. The work function of clean Ag(111) is measured to be 4.58 eV, in agreement with the reported value in the literature [43]. The formation of Ag_2Bi alloy (at 0.55 ML Bi deposition) only slightly reduces the work function by less than 0.05 eV. This is consistent with substitutional surface alloy formation in the initial stage. The work function change is minor since the net dipolar component perpendicular to the surface is quite small.

Upon further Bi deposition above 0.55 ML, the work function decreases rapidly,

since at this stage Ag_2Bi alloy demixes and Bi overlayer forms on Ag(111). At ~1 ML coverage, it reaches a plateau value of 4.25 eV, which agrees with the typical value for Bi thin film [44]. The trend for work function change is apparently in agreement with the established charge transfer induced work function change [45] i.e., Bi atoms in the overlayer have a slightly positive charge, as predicted by DFT calculations. Thus there is most likely a small dipole at the interface of Bi overlayer and Ag(111).

3.5 - Conclusions

In summary, we have investigated the coverage dependent electronic states of Bi ultra thin films deposited on Ag(111) by XPS and UPS. The evolution of electronic states is in accordance with our previous structural investigations by STM and LEED. At low Bi coverage (θ < 0:55 ML), Bi atoms intermix with Ag to form Ag_2Bi surface alloy and the sp-derived Shockley surface state on Ag(111) is rapidly quenched. As Bi coverage increases, Bi(110) overlayer forms on Ag(111) and a new state is observed at θ ~ 0:9 ML arising from electronic states localized at the Ag–Bi interface. The core level of Bi 4f for the Ag2Bi alloy are shifted to lower binding energy by ~0:6 eV and ~0:3 eV compared with that of bulk Bi and Bi(110) thin film on Ag(111) respectively. The core level binding energy shifts are associated with a complex superposition effect of outward relaxation of Bi atoms, final state screening and charge transfer from Bi to Ag substrate. Finally we also discuss the change of work function based on Bi structures and charge transfer model.

3.6 - References

[1] Cucka, P. and Barrett, C.S., 1962. The crystal structure of Bi and of solid solutions of Pb, Sn, Sb and Te in Bi. *Acta Crystallographica,* 15(9), pp. 865.

[2] Issi, J.P., 1979. Low Temperature Transport Properties of the Group V Semimetals. *Australian Journal of Physics,* 32, pp. 585.

[3] Shick, A.B., Ketterson, J.B., Novikov, D.L. and Freeman, A.J., 1999. Electronic structure, phase stability, and semimetal-semiconductor transitions in Bi. *Phys. Rev. B,* 60(23), pp. 15484.

[4] Koroteev, Y.M., Bihlmayer, G., Gayone, J.E., Chulkov, E.V., Blügel, S., Echenique, P.M. and Hofmann, P., 2004. Strong Spin-Orbit Splitting on Bi Surfaces. *Phys. Rev. Lett.,* 93(4), pp. 046403.

[5] Hofmann, P., Gayone, J.E., Bihlmayer, G., Koroteev, Y.M. and Chulkov, E.V., 2005. Electronic structure and Fermi surface of Bi(100). *Phys. Rev. B,* 71(19), pp. 195413.

[6] Ast, C.R. and Höchst, H., 2001. Fermi Surface of Bi(111) Measured by Photoemission Spectroscopy. *Phys. Rev. Lett.,* 87(17), pp. 177602.

[7] Hofmann, P., 2006. The surfaces of bismuth: Structural and electronic properties. *Progress in Surface Science,* 81(5), pp. 191-245.

[8] Agergaard,S.,. Sondergaard, C., Li, H., Nielsen,, M. B., Hoffmann, S.V., Li, Z., Hofmann, P., 2001. The effect of reduced dimensionality on a semimetal: the electronic structure of the Bi(110) surface. *New Journal of Physics,* 3, pp. 15.

[9] Bychkov, Y.A. and Rashba, E.I., 1984. Properties of a 2D electron gas with lifted spectral degeneracy. *JETP Lett.,* 39, pp. 66.

[10] LaShell, S., McDougall, B.A. and Jensen, E., 1996. Spin Splitting of an Au(111) Surface State Band Observed with Angle Resolved Photoelectron Spectroscopy. *Phys. Rev. Lett.,* 77(16), pp. 3419.

[11] Ast, C.R., Henk.J., Ernst.A., Moreschini, L., Falub, M.C., Pacilé, D., Bruno, P., Kern, K. and Grioni, M., 2007. Giant Spin Splitting through Surface Alloying. *Phys. Rev. Lett.,* 98(18), pp. 186807.

[12] Mathias, S., Ruffing, A., Deicke, F., Wiesenmayer, M., Sakar, I., Bihlmayer, G., Chulkov, E.V., Koroteev, Y.M., Echenique, P.M., Bauer, M. and Aeschlimann, M., 2010. Quantum-Well-Induced Giant Spin-Orbit Splitting. *Phys. Rev. Lett.,* 104(6), pp. 066802.

[13] Pacilé, D., Ast, C.R., Papagno, M., Da Silva, C., Moreschini, L., Falub, M., Seitsonen, A.P. and Grioni, M.1., 2006. Electronic structure of an ordered Pb⁄Ag(111) surface alloy: Theory and experiment. *Phys. Rev. B,* 73(24), pp. 245429.

[14] Harrison, M.J., Woodruff, D.P. and Robinson, J., 2004. Surface alloys, surface rumpling and surface stress. *Surface Science,* 572(2–3), pp. 309-317.

[15] Zhang, K.H.L., McLeod, I.M., Lu, Y.H., Dhanak, V.R., Matilainen, A., Lahti, M., Pussi, K., Egdell, R.G., Wang, X.S., Wee, A.T.S. and Chen, W., 2011. Observation of a surface alloying-to-dealloying transition during growth of Bi on Ag(111). *Phys. Rev. B,* 83(23), pp. 235418.

[16] Zhang, H.L., Chen, W., Wang, X.S., Yuhara, J. and Wee, A.T.S., 2009. Growth of well-aligned Bi nanowire on Ag(1 1 1). *Applied Surface Science,* 256(2), pp. 460-464.

[17] McLeod, I.M., Dhanak, V.R., Matilainen, A., Lahti, M., Pussi, K. and Zhang, K.H.L., 2010. Structure determination of the Bi−Ag(111) surface alloy using LEED I–V and DFT analyses. *Surface Science,* 604(17–18), pp. 1395-1399.

[18] Kresse, G. and Hafner, J., 1994. Norm-conserving and ultrasoft pseudopotentials for first-row and transition elements. *Journal of Physics: Condensed Matter,* 6(40), pp. 8245-8257.

[19] Kresse, G. and Joubert, D., 1999. From ultrasoft pseudopotentials to the projector augmented-wave method. *Physical Review B - Condensed Matter and Materials Physics,* 59(3), pp. 1758-1775.

[20] Blöchl, P.E., 1994. Projector augmented-wave method. *Physical Review B,* 50(24), pp. 17953-17979.

[21] Perdew, J.P. and Wang, Y., 1992. Accurate and simple analytic representation of the electron-gas correlation energy. *Physical Review B,* 45(23), pp. 13244-13249.

[22] Henkelman, G., Arnaldsson, A. and Jónsson, H., 2006. A fast and robust algorithm for Bader decomposition of charge density. *Computational Materials Science,* 36(3), pp. 354-360.

[23] Tang, W., Sanville, E. and Henkelman, G., 2009. A grid-based Bader analysis algorithm without lattice bias. *Journal of Physics: Condensed Matter,* 21(8), pp. 084204.

[24] Dharmadhikari, V.S., Sainkar, S.R., Badrinarayan, S. and Goswami, A., 1982. Characterisation of thin films of bismuth oxide by X-ray photoelectron spectroscopy. *Journal of Electron Spectroscopy and Related Phenomena,* 25(2), pp. 181-189.

[25] Moulder, J. F., Stickle, W. F., Sobol, P. E. and Bomben, K. D., 1995. Handbook of X-Ray Photoelectron Spectroscopy A Reference Book of Standard Spectra for Identification and Interpretation of XPS Data, Physical Electronics, Inc, 6509 Flying Cloud Drive Eden Prairie, Minnesota 55344 USA.

[26]　　Alden, M., Skriver, H. L., Johansson, B., 1994. Surface core-level shifts for simple metals, *Physical Review B* 50 pp. 12118.

[27] Eastman, D.E., HImpsel, F.J. and Van Der Veen, J. F., 1982. Photoemission studies of surface core - level shifts and their applications. *J. Vac. Sci. Technol.,* 20(3), pp. 609.

[28] Hüfner, S., 2003. *Photoelectron Spectroscopy.* 3rd edn. Berlin: Springer.

[29] Moreschini, L., Bendounan, A., Bentmann, H., Assig, M., Kern, K., Reinert, F., Henk, J., Ast, C.R. and Grioni, M., 2009. Influence of the substrate on the spin-orbit splitting in surface alloys on (111) noble-metal surfaces. *Phys. Rev. B,* 80(3), pp. 035438.

[30] Jepsen, O., Glötzel, D. and Mackintosh, A.R., 1981. Potentials, band structures, and Fermi surfaces in the noble metals. *Phys. Rev. B,* 23(6), pp. 2684.

[31] Wehner, P.S., Williams, R.S., Kevan, S.D., Denley, D. and Shirley, D.A., 1979. Valence-band structure of silver along Λ from angle-resolved photoemission. *Phys. Rev. B,* 19(12), pp. 6164.

[32] Christensen, N.E., 1972. The Band Structure of Silver and Optical Interband Transitions. *physica status solidi (b),* 54(2), pp. 551-563.

[33] Kevan, S.D. and Gaylord, R.H., 1987. High-resolution photoemission study of the electronic structure of the noble-metal (111) surfaces. *Phys. Rev. B,* 36(11), pp. 5809.

[34] Forster, F., Nicolay, G., Reinert, F., Ehm, D., Schmidt, S. and Hüfner, S., 2003. Surface and interface states on adsorbate covered noble metal surfaces. *Surface Science,* 532–535(0), pp. 160-165.

[35] Lindgren, S.A. and Walldén, L., 1980. Photoemission of electrons at the Cu(111)/Na interface. *Solid State Communications,* 34(8), pp. 671-673.

[36] Lindgren, S.A. and Walldén, L., 1980. Electronic structure of clean and oxygen-exposed Na and Cs monolayers on Cu (111). *Phys. Rev. B,* 22(12), pp. 5967.

[37] Oughaddou, H., Sawaya, S., Goniakowski, J., Aufray, B., Le Lay, G., Gay, J.M., Tréglia, G., Bibérian, J.P., Barrett, N., Guillot, C., Mayne, A. and Dujardin, G., 2000. Ge/Ag(111) semiconductor-on-metal growth: Formation of an Ag_2Ge surface alloy. *Phys. Rev. B,* 62(24), pp. 16653.

[38] Dalmas, J., Oughaddou, H., Le Lay, G., Aufray, B., Tréglia, G., Girardeaux, C., Bernardini, J., Fujii, J. and Panaccione, G., 2006. Photoelectron spectroscopy study of Pb/Ag(1 1 1) in the submonolayer range. *Surface Science,* 600(6), pp. 1227-1230.

[39] Wang, P., Gao, X., Xun, K., Jia, J.F., Qian, H.J., Liu, F.Q., Ibrahim, K., Zhou, Y.M., Xue, Q.K. and Wu, S.C., 2003. Atomic and electronic structure of (3×3)R 30°-In phase on Cu(111). *Solid State Communications,* 125(9), pp. 509-514.

[40] Bihlmayer, G., Blügel, S. and Chulkov, E.V., 2007. Enhanced Rashba spin-orbit splitting in Bi∕Ag(111) and Pb∕Ag(111) surface alloys from first principles. *Phys. Rev. B,* 75(19), pp. 195414.

[41] Nakagawa, T., Mitsushima, S., Okuyama, H., Nishijima, M. and Aruga, T., 2002. Evolution of geometric and electronic structure in ultrathin In films on Cu(001). *Phys. Rev. B,* 66(8), pp. 085402.

[42] Nakagawa, T., Saito, Y., Ohgami, O., Okuyama, H., Nishijima, M. and Aruga, T., 2005. Evolution of geometric and electronic structure at the Bi∕Ag(001) interface. *Phys. Rev. B,* 72(16), pp. 165405.

[43] Chelvayohan, M. and Mee, C.H.B., 1982. Work function measurements on (110), (100) and (111) surfaces of silver. *Journal of Physics C: Solid State Physics Email alert RSS feed,* 15(10), pp. 2305.

[44] Apker, L., Taft, E. and Dickey, J., 1949. Some Semimetallic Characteristics of the Photoelectric Emission from As, Sb, and Bi. *Phys. Rev.,* 76(2), pp. 270.

[45] Lüth, H., 2001. *Solid Surfaces, Interfaces and Thin Films.* 4th edn edn. Berlin: Springer.

Chapter 4

Observation of a surface alloying-to-dealloying transition during

growth of Bi on Ag(111)

4.1 - Abstract

The atomic structures that develop as a function of coverage during deposition of Bi on Ag(111) have been studied using low-temperature scanning tunneling microscopy, low energy electron diffraction, and ab initio calculations. The growth process involves two sequential stages. At low coverage, Bi atoms are incorporated into the topmost layer of Ag(111), resulting in the formation of an Ag_2Bi alloy confined to the surface and ordered $(\sqrt{3} \times \sqrt{3})R30°$ Ag_2Bi islands supported on Ag(111). This mode of accommodation of Bi was found to be energetically favorable based on ab initio total-energy calculations. At coverage above a critical value of 0.55 monolayers, the Ag_2Bi alloy phase gradually converts into an ordered Bi $(p \times \sqrt{3})$ overlayer structure supported on Ag(111). We postulate that the dealloying transition is likely driven by compressive strain induced by incorporation of large-size Bi atoms into Ag at a high coverage and the subsequent lack of miscibility of Ag and Bi bulk phases. After completion of the dealloying process, Bi(110) thin films can be grown epitaxially on top of Ag(111) with a chemically abrupt interface.

4.2 - Introduction

The study of the heteroepitaxial growth of metals on metallic substrates has been motivated by the demand for high- quality thin metallic heterostructures with sharp interfaces in technological applications such as magnetic data storage and spintronics.[1–3] It is becoming clear that a wealth of complex phenomena may arise at an atomic scale that are not predicted from simple thermodynamic considerations of the respective surface and interface energies of the metal adatoms and the substrates.[4–7] Tersoff has predicted that surface-confined alloy phases may arise as an alternative to overlayer structures as a means to relieve the surface stress in systems dominated by an atomic size mismatch, even in cases where the metals are immiscible in the bulk.[8] This is particularly the case for the growth of comparatively heavier elements such as lead (Pb), antimony (Sb), and bismuth (Bi) on noble-metal surfaces.[8–13] Surface alloying is a powerful way of developing unique physical and chemical properties in alloys that do not have a bulk counterpart.[14–16] Elegant examples include the exceptionally large spin-orbit splittings of surface states in surface alloys between heavy elements such as Bi or Pb on light metals such as Cu and Ag, which opens potential applications in the area of spintronics.[17,18]

Bi is a typical group-V element and adopts a rhombohedra A7 lattice belonging to the space group R3m. There are two atoms per unit cell, which can also be described by a hexagonal basis.[19] The band structure of Bi is that of a semimetal with an overlap of ~ 40 meV between valence and conduction bands that arises due to a slight distortion along the trigonal axis, which is (111) in the rhombohedra basis or (0001) in the hexagonal basis. Bi possesses an unusual array of physical properties, including low carrier density, a long Fermi wavelength (~ 40 nm at room temperature), and high

carrier mobility. Most interestingly, the low-index surfaces of Bi such as Bi(111), Bi(100), and Bi(110) show very different electronic properties from the bulk associated with spin-orbit (SO) splitting at the surface due to the breakdown of inversion symmetry (the so-called Rashba-Bychkov effect).[19–21]

It has been recently reported that submonolayer Bi on Ag(111) forms a $(\sqrt{3} \times \sqrt{3})R30°$ surface alloy.[17] The $(\sqrt{3} \times \sqrt{3})R30°$ structure is of particular interest because the inter- mixing of the size mismatched atoms and the corresponding in- plane potential variations lead to giant SO splitting, which has implications for spintronics applications.[17,22,23] Nonetheless, a detailed investigation of the atomic structures of these two- dimensional (2D) surface alloys is still lacking, even though such structural information plays a critical role in determining the in-plane potential gradient, and thus the SO splitting of the surface alloys.[24] Furthermore, a similar class of electronic states evolves by the quantum confinement of electrons in ultrathin films with a thickness comparable to the electron coherence length, to give so-called quantum well states. It has been recently reported that a giant SO splitting of quantum well states has been observed within a Bi monolayer on Cu(111).[25] Based on first-principles calculations, the authors argued that the huge SO splitting originated from the perpendicular potential at the surface and interface of the ultrathin Bi film. This finding opens the possibility of controlling the SO splitting by tuning the nanostructure of the ultrathin film.

In the present work, we present a detailed study of the nucleation of Bi on Ag(111), the subsequent development of the Ag_2Bi surface alloy, and the growth of a Bi thin film on Ag(111) using scanning tunneling microscopy (STM) and ab initio total-energy calculations. We show that in the initial stages of deposition Bi atoms are incorporated

into the topmost Ag(111) layer by exchanging with the surface Ag atoms to form a substitutional surface alloy. This mode of incorporation was found to be energetically favourable based on ab initio total-energy calculations. However, a surface dealloying process ensues with increasing Bi coverage, presumably driven by the high compressive strain induced by incorporation of larger-size Bi atoms into the Ag matrix at high concentrations. For coverages above 1 monolayer (ML), the Ag_2Bi surface alloy demixes and a highly ordered Bi(110) monolayer is formed on top of Ag(111).

4.3 - Experimental and Computational Methods

The experiments were carried out in a homebuilt multi- chamber ultrahigh vacuum (UHV) system with a base pressure of better than 2×10^{-10} mbar incorporating an Omicron low-temperature scanning tunneling microscope (LT-STM) stage.[26] The STM was operated with a Nanonis controller (Nanonis, Switzerland). Ag(111) substrates were cleaned by repeated cycles of Ar+ sputtering and annealing at 800 K. The cleanliness and surface order of the samples was checked by LT-STM images, which in the final stages of cleaning showed sharp step edges and smooth terraces without obvious signs of impurities. Bi was thermally evaporated from a Knudsen cell in a growth chamber with a base pressure of better than 3×10^{-10} mbar. The Bi deposition rate was calibrated using a quartz microbalance (QCM) and was set at 0.05 ML/min, where 1 ML is defined as 1 atomic layer of Bi(110), i.e., 9.3×10^{14} atoms cm^{-2}. STM images were obtained at 77 K in constant-current mode with a chemically etched tungsten tip. Additional low-energy electron diffraction (LEED) experiments were performed in a standard UHV surface science chamber with rear view LEED optics from OCI Vacuum Microengineering.

The static calculations of total energies were performed using density functional theory (DFT) as implemented in the Vienna ab initio simulation package (VASP),[27,28] including the projector augmented-wave (PAW) potentials.[29] A kinetic energy cutoff of 400 eV was applied to the plane waves, which was found to produce well-converged results for both Ag and Bi. The exchange correlation potential employed the generalized gradient approximation (GGA) of the Perdew-Wang 91 (PW91) [30]. A 10×8×1 Monkhorst-Pack mesh was used for k-point sampling.[31] The Ag surface was modelled using a supercell approach with thin slabs separated by vacuum spacings. Periodic boundary conditions were applied to the central supercell so that it was reproduced periodically throughout xy space. The periodic slab was modelled with six layers of Ag atoms. A region of $\sim$ 10 Å of vacuum was inserted in the z direction to prevent interactions between periodic images. The SO coupling has not been switched on in the VASP calculation. We have tested that the SO coupling did not have significant effect on the resulting structures. The bottommost layer of the surface slab was frozen during the geometry relaxation. An Ag lattice constant of 4.17 Å was used, which was obtained from bulk cell optimization using the same computational parameters.

4.4 - Results and Discussion

4.4.1 – Surface Alloying at Low Coverage

Figure 4.1(a) shows a large-area STM image following deposition of 0.2 ML of Bi on a clean Ag(111) surface at room temperature. It reveals dispersed protrusions (marked P), large meandering two-dimensional (2D) islands (marked LI), and small compact islands (marked SI). The high-resolution STM image of Figure 4.1(b) indicates that the protrusions have a spherical shape with a diameter of $\sim$ 4 Å. The apparent height

between the protrusion and the surrounding Ag terrace is ∼ 0.3 Å, as seen by the line profile in Figure 4.1(c). These features are associated with Bi atoms incorporated into the topmost layer of Ag(111) by an exchange process which involves substitution of substrate Ag atoms by Bi atoms. The surface Bi protrusion is expected on the basis of a simple hard-sphere picture because the bulk metallic radii of Bi (1.56 Å) is larger than that of Ag (1.44 Å). This process results in the formation of a Bi-Ag alloy confined in
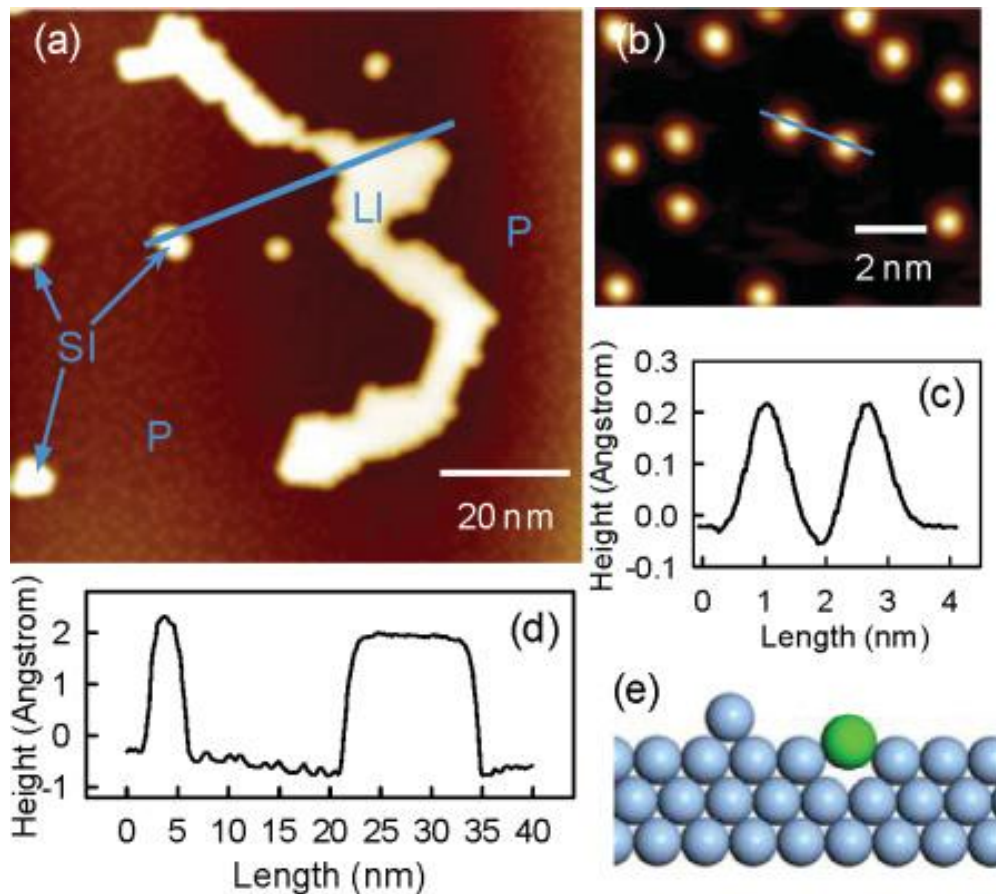
Figure 4.1 - (a) An overview of large-scale STM images of 0.2 ML Bi deposited on Ag(111) (Vs =− 1.8 V, It = 0.2 nA), showing dispersed protrusions (marked P), large meandering islands (marked LI), and small compact islands (marked SI). (b) High-resolution STM image of the disperse protrusions. (c) A line profile along the line in (b). (d) A line profile along the line in (a). (e) Schematic model for the incorporation of Bi (green) in an Ag lattice (navy).

the surface. It is noted that the substitutional Bi atoms are randomly distributed among the available Ag lattice sites. In contrast, the line profiles in Figure 4.1(d) indicate that the apparent topographic height of the meandering islands (LI) and small islands (SI) is 2.5 Å, corresponding to the height of an island one atomic layer thick. Atomically resolved STM images such as those shown in Figure 4.2(a) reveal that both islands have an ordered hexagonal lattice with a $(\sqrt{3} \times \sqrt{3})R30°$ superstructure (a ~ 5 A°), where the periodicity is defined in terms of the Ag(111) substrate surface. Based on these observations, we speculate that these islands contain a 2D Bi-Ag alloy layer and that the alloy layer is formed from Ag atoms that are displaced from the surface layer by Bi atoms along with nonembedded Bi adatoms found on the Ag(111) surface. A schematic model of the proposed structure is shown in Figure 4.3(a). The formation of this structure involves the following steps. First, deposited Bi atoms embed themselves
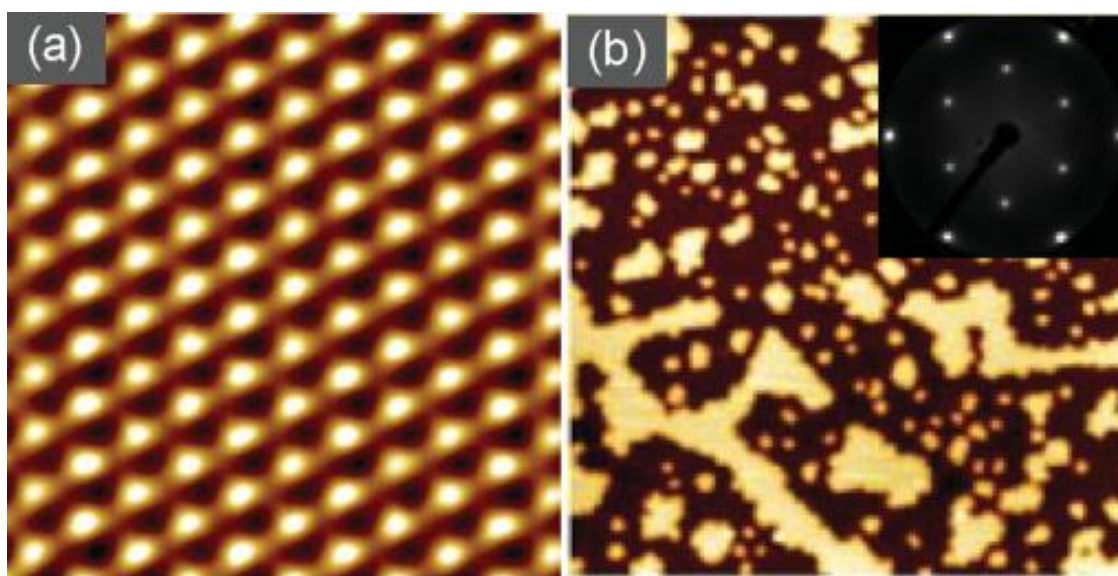
Figure 4.2 - (a) High-resolution 5 nm × 5 nm STM image (Vs = 1.2 V and It = 0.18 nA) from the top of a large meandering island, showing the supported Ag2Bi surface alloy with an ordered $(\sqrt{3} \times \sqrt{3})R30°$ superstructure (the bright spots are associated with Bi atoms). (b) Large-scale STM image (100 nm×100 nm) of 0.4 ML Bi deposited on Ag(111). The inset shows the LEED pattern of the $(\sqrt{3} \times \sqrt{3})R30°$ structure with an electron beam energy of 42 eV.

into the topmost Ag layer to form a dilute substitutional alloy. One Ag atom is displaced out of the surface for each Bi atom that is incorporated. The Ag adatoms then diffuse andcoalesce with nonembedded Bi adatoms to form the ordered Ag_2Bi alloy islands on top of Ag(111). We did not observe any pure Ag islands formed by nucleation of the displaced Ag adatoms, which indicates that these adatoms are stabilized in the form of ordered $(\sqrt{3} \times \sqrt{3})R30°$ islands. Hence one might expect a direct correlation between the numbers of embedded Bi atoms and the surface area covered by $(\sqrt{3} \times \sqrt{3})R30°$ islands, given that each $(\sqrt{3} \times \sqrt{3})R30°$ unit cell contains one Bi and two ejected Ag atoms. Indeed, statistical analysis reveals that the density of substitutional Bi atoms is roughly identical to the density of Ag atoms in the ordered alloy islands. Furthermore, both the density of the embedded Bi atoms and the surface area of $(\sqrt{3} \times \sqrt{3})R30°$ islands increase linearly with the amount of Bi deposited. As shown in Figure 4.2(b), with 0.4-ML Bi deposition most of the Ag surface is covered with Ag2Bi surface alloy islands. At this stage a well-defined $(\sqrt{3} \times \sqrt{3})R30°$ LEED pattern can be observed, as shown in the inset of Figure 4.2(b).

The phenomenon of alloy formation confined to a surface layer has been identified in many other heteroepitaxial systems, including those where there is bulk miscibility such as Ag/Cu(100),32 In/Cu(100),[33] and Au/Fe(100),[34] as well as in systems where the two components are immiscible in the bulk such as Au/Ni(110) [4] and Sb/Ag(111).[11] According to the theoretical study by Tersoff,[8] for systems dominated by atomic size mismatch, surface strain effects can favour alloying on a surface even though strain suppresses intermixing in the bulk. Clean metallic surfaces are normally under tensile stress due to broken bonds at the surface.[34] Thus the incorporation of large atoms into the surface is an efficient way to relieve the surface

tensile stress. Theoretical calculations based on the embedded atom method (EAM)

indicated that Ag(111) has a tensile surface stress of 0.6 eV Å^{-2}.[35] Therefore, the
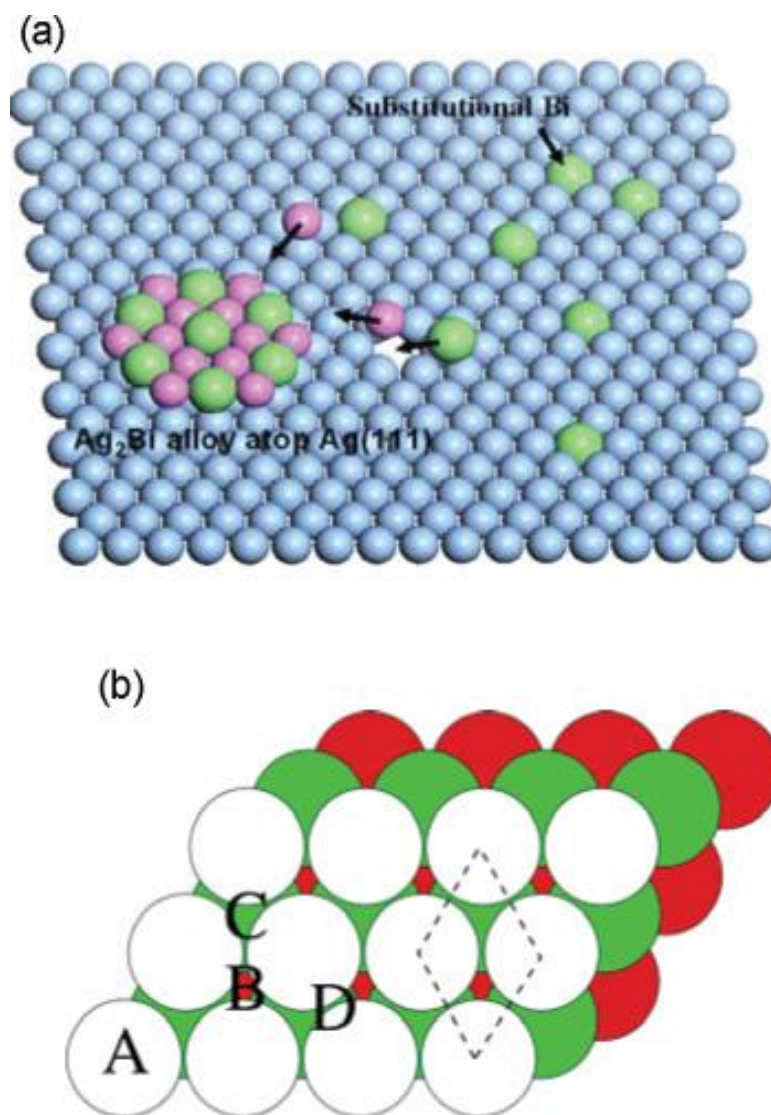
Figure 4.3 - (a) Schematic of the formation of the Ag2Bi surface alloy: Ag lattice (navy), Bi atoms (green), and squeezed Ag atoms (pink). (b) The four adsorption sites (A = top, B and C = hollow, and D = bridge) considered in DFT calculations. The corresponding adsorption energies are given in Table 4.1. The white spheres represent the first Ag layer, the green spheres represent the layer, and the red spheres represent the third layer.

tensile surface stress can be effectively relaxed by the incorporation of the large Bi atom (metallic radii = 1.56 Å) into the Ag (1.44 Å) lattice. This is despite the fact that the surface energy for Bi(110), $\gamma_{Bi}(110) = 0.541$ J m^{-2}, is much smaller than the surface energy for Ag(111), $\gamma_{Ag}(111) = 1.17$ J m^{-2}, which would appear to favour formation of a Bi overlayer structure on Ag(111).[36] Similar considerations also explain the preference for substitutional Bi atoms to be distributed within the Ag lattice without any clustering. Because of the larger size of Bi, the incorporation of Bi atoms into the Ag lattice can induce local strain fields, which causes two nearest-neighbour embedded atoms to repel each other in the surface. Thus the embedded Bi atoms never have Bi nearest neighbours. Recent ab initio studies of the 3d transition metals on Au(100) also showed a repulsive interaction between nearest-neighbour embedded atoms, thus explaining the random distribution of the embedded impurities.[37] By contrast, the local strain can be effectively relieved in the Ag$_2$Bi alloy overlayer because of the finite size of the alloy islands supported on the Ag substrate.

However, the model proposed by Tersoff takes into account only the strain energy of the system.[8] The equilibrium structure will be determined by minimization of the total energy and not just the surface strain energy. Therefore, we performed first-principles DFT calculations to compare the energies of adsorption and incorporation for Bi on Ag(111) at various sites, including on-top, hollow, and bridge adsorption sites as well substitutional sites, as indicated in Figure 4.3(b). [38] The adsorption energies of Bi atom are defined as;

$$E_{ads} = \frac{1}{N_{Bi}}(E_{tot} - E_{clean} - N_{Bi}E_{Bi}) \qquad (4.1)$$

where E_{tot} is the total energy of a relaxed Ag/Bi supercell; E_{clean} is the total energy of the relaxed clean Ag slab; N_{Bi} is the number of Bi atoms and E_{Bi} is the energy of one

atom in the bulk of the Bi metal. For substitutional alloy structures the adsorption energy is defined as

$$E_{ads} = \frac{1}{N_{Bi}}(E_{tot} - E_{clean} - N_{Bi}E_{Bi} + N_{Bi}E_{Ag-bulk}) \qquad (4.2)$$

where EAg-bulk is the total energy of an Ag bulk atom.

The adsorption energies for each site of the models that showed convergence in the calculations are listed in Table 4.1. The fcc hollow site B is the most favourable for absorption, albeit with a small energy difference between the two possible hollow sites and the bridge sites. However, the substitutional surface alloy structure was found to be the most stable configuration, with an absorption energy of −0.353 eV. There is thus a clear preference for the occupation of substitutional sites in the surface layer. The DFT calculations also indicate that the "rumpling" of the surface alloy has an amplitude of 0.6 Å, with the Bi atoms sitting above the underlying Ag surface atoms. This is in good agreement with a recent structural determination of the $(\sqrt{3} \times \sqrt{3})R30°$ surface

Adsorption site	Adsorption energy (eV)
Top (A)	0.414
Hollow (B)	0.198
Hollow (C)	0.234
Bridge (D)	0.208
Surface alloy	−0.353

Table 4.1 -. Adsorption energies for different adsorption sites as indicated in Figure 4.3(b).
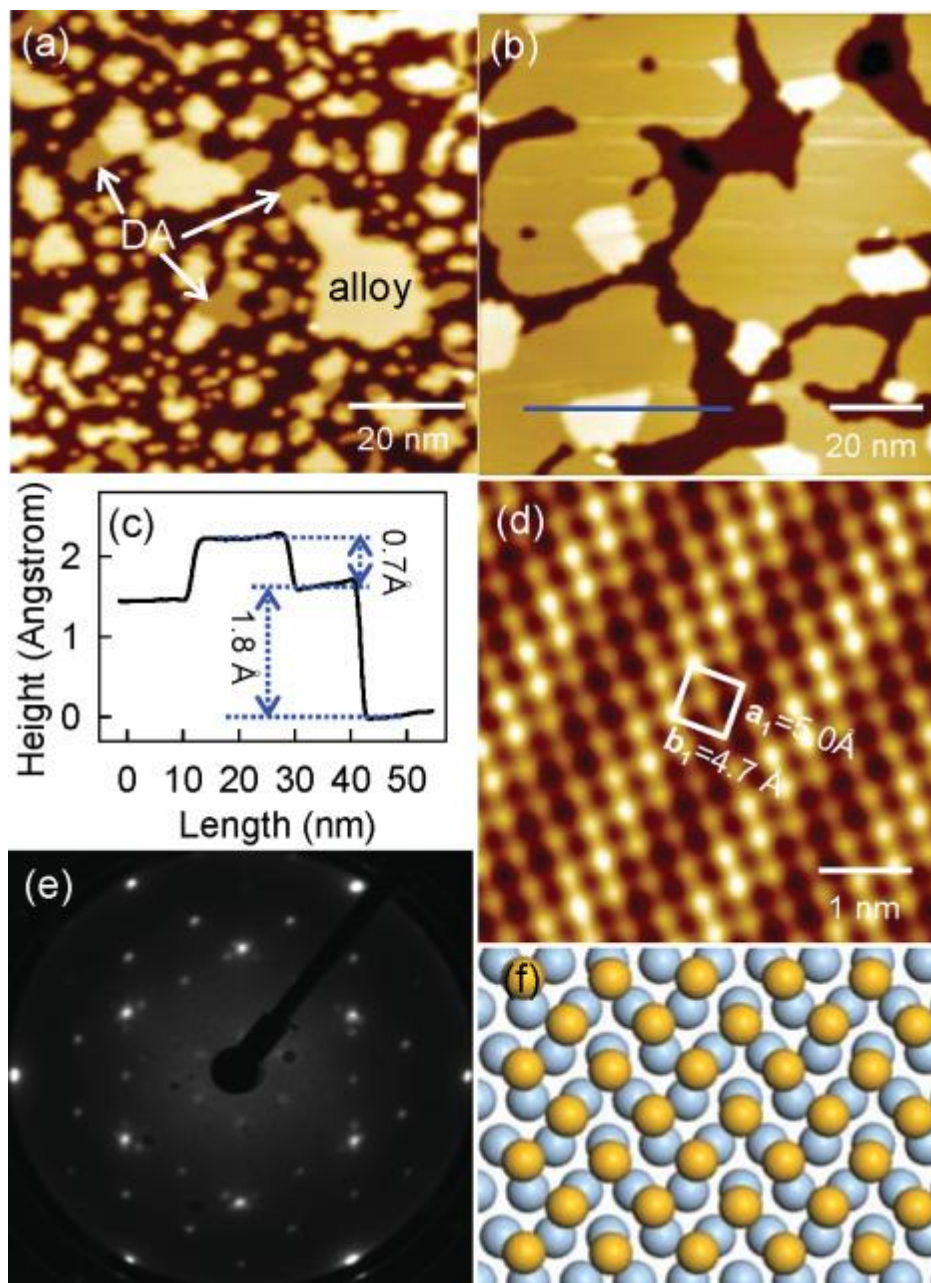
Figure 4.4 - (a) Large-scale STM image of 0.6 ML Bi deposited on Ag(111), showing the appearance of (p × √3) overlayers with a low height at the step edges of (√3 × √3)R30∘ islands (labelled as "DA"). (b) The coverage of the (p × √3) overlayers increases as 0.75 ML Bi was deposited on Ag(111). (c) A line profile along the line in (b), indicating that the height of the (p × √3) overlayer is 1.8 A° with respect to the substituted surface alloy and 0.7 A° lower than that of the (√3x√3)R30∘ islands. (d) Atomic structure of the (p × 3) overlayer structure with lattice constants of a1 = 5.0 A° , b1 = 4.7 A° . (e) LEED pattern (with an electron energy of 38 eV) for the (p√3) overlayer. (f) Schematic model for the (p ×3) Bi overlayers (yellow) on Ag(111) (navy).

structure of the Ag_2Bi alloy layer by the analysis of LEED curves.[38] The rumpling amplitude is larger than the apparent protrusion height measured by STM. This can be explained by the fact that the apparent height in a STM image depends on both the topographic height and the density of electronic states near the Fermi level. This amplitude is, however, smaller by $\sim$ 0.24 Å than that predicted by a simple hard-sphere model based on bulk metallic radii of 1.44 Å for Ag and 1.56 Å for Bi. This suggests a reduction in the effective radii that is similar to that found by Quinn et al.[12] in their LEED study of the substitutional surface alloy structure for the Pb-Ni(111) system. It has been suggested that the reduction in the effective radii may be attributed to the influence of valence electron charge smoothing and associated surface stress effects. A similar effect is possibly the case for the Bi-Ag(111) structure in our study.

4.4.2 - Dealloying and the Bi Overlayer Structure

The Bi surface alloy saturates at coverage of 0.5 ML, which corresponds to 0.33 ML if defined in terms of atomic layers of Ag(111) with a sheet density of 1.38×1015 cm^{-2}. With additional Bi deposition, the Bi-Ag system undergoes a dealloying process. Figures 4.4(a) and 4.4(b) show STM images which trace the evolution of the dealloying process as the Bi coverage increases. In Figure 4.4(a) the Bi coverage is slightly above the saturation limit, and a different type of island begins to appear with a lower height above the surface than the $(\sqrt{3} \times \sqrt{3})R30°$ alloy islands. These are labelled DA in the figure. As will be discussed below, these different islands have √3 periodicity along the Ag[11$\underline{2}$] direction, but are incommensurate in the orthogonal direction. Following notation introduced by Chen et al.,[39] this structure is designated as (p × √3). The authors used an electrochemical deposition technique and found that p depended on the

deposition potential, hence the choice of this letter. The switchover of the structure developed further as the Bi coverage was increased to 0.75 ML [Figure 4.4(b)]. Clearly, both the island size and the total coverage by the $(p \times \sqrt{3})$ overlayer islands increase dramatically, whereas the area of the $(\sqrt{3} \times \sqrt{3})R30°$ islands and substitutional surface alloy decreases. Figure 4.4(c) shows a height profile along the line marked in Figure 4.4(b), indicating that the apparent height of the $(p \times \sqrt{3})$ overlayer is 1.8 Å with respect to the substituted surface alloy and is thus 0.7 Å lower than that of the $(\sqrt{3} \times \sqrt{3})R30°$ islands. A high-resolution image is shown in Figure 4.4(d). This reveals the atomic structure within the $(p \times \sqrt{3})$ islands and suggests that this overlayer is based on a rectangular nonprimitive unit cell. The unit cell vectors are $a_1 = 5.0$ Å along the Ag[11$\underline{2}$] direction and $b_1 = 4.7$ Å along the Ag[1$\underline{1}$0] direction. Figure 4.4(e) shows a LEED pattern measured with an electron energy of 38 eV for the $(p \times \sqrt{3})$ overlayer. It further confirms that the a_1 direction of the Bi overlayer structure is commensurate with the Ag(111) surface along the Ag[11$\underline{2}$] direction ($a_1 = a_{Ag}\sqrt{3}$), but incommensurate along the Ag[11$\underline{0}$] direction. Because of the threefold symmetry of the Ag(111) surface, there are three coexisting domains of the rectangular structures rotated 120° and 240° with respect to each other. The $(p \times \sqrt{3})$ overlayer structure is similar to a Bi $(p \times \sqrt{3})$ overlayer structure on Au(111) formed by electrochemical deposition.[39] The lattice constants are slightly larger than those found in the Bi(110) planes of elemental bismuth, where ($a_2 = 4.74$ Å , $b_2 = 4.54$ Å), so that the atomic density of 8.0×10^{14} cm^{-2} is also lower than in the Bi metal. A modulation with an amplitude of 0.2 Å is seen to be superimposed on the ordered Bi overlayer structures along the Ag[1$\underline{1}$0] direction. This modulation is straightforwardly explained as a moire´ pattern arising from the interference between the Bi overlayer and the Ag substrate along the [110]

direction. We thereby identify the (p × √3) islands as pure Bi overlayers formed during the dealloying process sitting on top of Ag(111). A structural model for the (p × √3) overlayer based on the atomic resolution image is proposed in Figure 4.4(f). At a coverage of 0.9 ML, we found that there is complete coverage of the surface by the (p × √3) overlayer so that the dealloying process is complete.

Dealloying transitions similar to those found here have been observed in several other systems including Pd/Cu(111),[40] In/Cu(100),[32] Mn/Cu(001),[41] and Au/Ni(110).[42] Relief of the compressive energy is proposed as one of the driving forces for the dealloying process. In the Au/Ni(110) system,[42] Au atoms initially alloy into the Ni(110) surface at low coverage but dealloy into a vacancy- stabilized Au
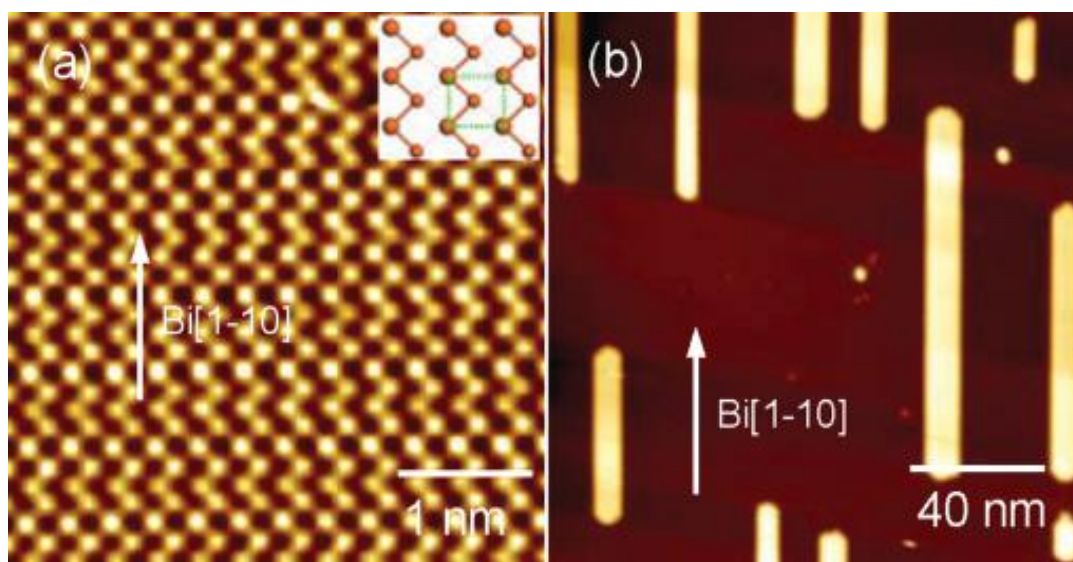

Figure 4.5 - (a) Atomic resolution STM image of 1 ML Bi deposited on Ag(111), showing the formation of a Bi monolayer with the Bi(110) plane. The inset shows the atomic configuration of the Bi(110) plane. (b) STM image of 1.5 ML Bi deposition on Ag(111), showing the elongated growth along the Bi[11̄0] direction.

dimer-trimer chain structure at Au coverages larger than 0.4 ML. Based on total-energy calculations it was shown that the surface compressive stress induced by the substituted Au drives the surface alloy to dealloy above a critical coverage. Similarly, in the present Ag-Bi system, the tensile stress of the clean Ag surface is originally relieved by the incorporation of large-sized Bi atoms into the Ag lattice. However, above a critical coverage, further incorporation of Bi turns the tensile stress into compressive stress. Hence, as the Bi coverage increases above the critical limit, a dealloying process is favoured.

We suggest a possible mechanism for the dealloying process and formation of the ($p \times \sqrt{3}$) overlayer based on the following steps. First, starting at the step edges, the deposited Bi atoms replace the Ag atoms in the ($\sqrt{3} \times \sqrt{3}$)R30° islands on Ag(111) to form the ($p \times \sqrt{3}$) overlayer. Second, the displaced Ag atoms diffuse onto the substrate terraces and displace Bi atoms from the substitutional sites, thereby recovering the original pure Ag(111) surface. The displaced Bi atoms can add to the ($p \times \sqrt{3}$) island, playing a role similar to that of the deposited Bi atoms. We did not observe any ($p \times \sqrt{3}$) structures embedded into the terraces during STM scanning. Thus the possibility that deposited Bi atoms can replace Ag atoms in the substitutional alloy to form an embedded Bi layer can be ruled out. As a result of these processes a chemically abrupt interface can be recovered by the dealloying process.

4.4.3 - Bi(110) Overlayers

The Bi ($p \times \sqrt{3}$) overlayer phase shows a further structural transition with increasing coverage. As shown in Figure 4.5(a), after deposition of 1 ML of Bi, the lattice constants decrease compared to those discussed in Sec. III B and a rectangular unit cell

with a_2 = 4.74 Å and b_2 = 4.54 Å can be identified in the image. The atomic density has increased to a value of 9.3×10^{14} cm^{-2}. The surface unit cell contains two atoms, and the central atom in the cell is offset to the short edge of the unit cell to give a structure containing zigzag chains. The com- pressed overlayer structure is basically that found on the (110) surface of elemental Bi. Based on STM and LEED observations, the epitaxial relationship between Bi(110) and Ag(111) is determined to be Bi[1$\underline{1}$0] ∥ Ag[1$\underline{1}$0] and Bi[001] ∥ Ag[11$\underline{2}$] with $7|a_{Bi[1\underline{1}0]}|$ = $11|a_{Ag[1\underline{1}0]}|$ and $20|a_{Bi[001]}|$ = $19|a_{Ag[11\underline{2}]}|$.[43] This is similar to the adsorption structure of Bi(110) thin films electrodeposited on Au(111).[44] In a simple model, the phase transition from the (p × √3) structure to Bi(110) is determined by two competing interactions, namely, Ag-Bi substrate-overlayer interactions and Bi-Bi overlayer-overlayer interactions. In the loosely packed (p × √3) overlayer, the Ag-Bi interaction dominates over the Bi-Bi interaction. This statement is corroborated by the fact that the (p × √3) is locked pseudomorphically to the [11$\underline{2}$] direction of the Ag substrate. The relatively strong Ag-Bi interaction causes the Bi atoms to adopt positions determined by the Ag substrate lattice. However, with increasing Bi coverage, Bi-Bi interactions become more important and gradually become the major determinant of surface structure. Thus Bi-Bi interaction drives Bi to adopt its own lattice structure, giving rise to an incommensurate Bi(110) monolayer.

Increasing the Bi coverage to beyond 1 ML promotes the growth of Bi ribbon bilayers elongated along the [1$\underline{1}$0] direction, as shown in Figure 4.5(b).[43] The preferential growth of Bi ribbons elongated along this direction results from the preferential attachment of Bi atoms to the ends of the ribbons. Bulk Bi has highly anisotropic bonding[19] and the surface structure of Bi(110) is characterized by zigzag covalently bonded atomic chains running along the [1$\underline{1}$0] direction, with weaker bonds in the

orthogonal direction [the inset in Figure 4.5(a)]. Therefore, Bi adatoms on the surface preferentially attach to the ends of the ribbons, resulting in preferential growth along the Bi [1$\underline{1}$0] direction. Furthermore, the growth of Bi ribbons is quantized into double (110) layers units with a width of 6.6 Å , and the growth exhibits an even-number layer stability. This is consistent with recent observations of "magic" thicknesses in ultrathin Bi films on the Si(111) surface, where Bi(110) 2D islands with an even number of layers are dominant.[45] This stability is attributed to the energetically preferred pairing of two neighbouring layers. On a bulk-terminated Bi(110) surface, 50% of surface atoms have pz dangling bonds. In a film with an even number of (110) layers, the dangling bonds are completely saturated by pairing with a neighbouring layer. All the atoms are then threefold coordinated, leading to stabilization of the (110) surface. In contrast, films with an odd number of layers are not stable since the dangling bonds of the top layer are unable to be saturated by layer pairing.

4.5 - Conclusions

In summary, we have investigated the coverage-dependent growth of Bi on Ag(111) and have identified a number of atomically ordered structures. The system exhibits an alloying and dealloying process that is typical for metal-on-metal systems where the individual components are not miscible as bulk phases. It is energetically favourable for the initially deposited Bi atoms to be incorporated into the topmost Ag(111) layer by exchanging with surface Ag atoms to form a dilute array of substitutional Bi atoms within the Ag matrix as well as an adlayer of the Ag_2Bi surface alloy. Since the incorporation of larger-sized Bi atoms presumably induces a compressive strain, a surface dealloying process ensues when the Bi coverage is reaches a critical value.

Future stress measurements or kinetic Monte Carlo calculations are required to elucidate the mechanisms and driving force for the dealloying process. Nevertheless the Ag2Bi alloy phase gradually converts into an ordered (p × √3) overlayer structure with a rectangular lattice 2D surface cell with $a_1 = 5.0$ Å , $b_1 = 4.7$ Å supported on Ag(111). After the dealloying process is complete, Bi(110) thin films can be finally grown epitaxially on Ag(111) with a chemically abrupt interface. The "rumpling" of the surface alloy determined from experimental and ab initio calculations may provide additional information necessary to understand the giant spin splitting recently observed in the Bi/Ag(111) surface alloy system, which was believed to originate from a strong in-plane gradient of the crystal potential in the surface layer. This also provides a model system to envision the alloying process in other systems such as Pb on Ag(111), which exhibit a large Rashba effect. The ultrathin Bi films on Ag(111) may exhibit unusual properties originating from quantum confinement effects coupled with the unique properties of the Bi surface, opening up potential applications in spintronic devices.[19,25] As an elegant example, the quantum well state confinement by the ultrathin Bi film can induce a huge SO splitting. From a fundamental point of view, the results contribute further to the understanding of surface and interface phenomena in heteroepitaxial growth in materials.

4.6 - References

[1]   Wuttig, M. and Liu, X., 2004. *Ultrathin Metal Films.* New York: Springer.

[2] Shchukin, V.A. and Bimberg, D., 1999. Spontaneous ordering of nanostructures on crystal surfaces. *Rev. Mod. Phys.,* 71(4), pp. 1125.

[3] Barth, J.V., Costantini, G. and Kern, K., 2005. Engineering atomic and molecular nanostructures at surfaces. *Nature,* 437, pp. 671.

[4] Pleth Nielsen, L., Besenbacher, F., Stensgaard, I. and Laegsgaard, E., 1993. Initial growth of Au on Ni(110): Surface alloying of immiscible metals. *Phys. Rev. Lett.,* 71(5), pp. 754.

[5]   Röder, H., Hahn, E., Brune, H., Bucher, J. and Kern, K., 1993. Building one- and two-dimensional nanostructures by diffusion-controlled aggregation at surfaces. *Nature,* 366, pp. 141.

[6] Meyerheim, H.L., Sander, D., Negulyaev, N.N., Stepanyuk, V.S., Popescu, R., Popa, I. and Kirschner, J., 2008. Buried Ni/Cu(001) Interface at the Atomic Scale. *Phys. Rev. Lett.,* 100(14), pp. 146101.

[7] Venables, J.A., Spiller, G.D.T. and Hanbucken, M., 1984. Nucleation and growth of thin films. *Reports on Progress in Physics,* 47(4), pp. 399.

[8] Tersoff, J., 1995. Surface-Confined Alloy Formation in Immiscible Systems. *Phys. Rev. Lett.,* 74(3), pp. 434.

[9] Dalmas, J., Oughaddou, H., Léandri, C., Gay, J., Le Lay, G., Tréglia, G., Aufray, B., Bunk, O. and Johnson, R.L., 2005. Ordered surface alloy formation of immiscible metals: The case of Pb deposited on Ag(111). *Phys. Rev. B,* 72(15), pp. 155424.

[10] Xiao, H.Y., Zu, X.T., He, X. and Gao, F., 2006. Sb adsorption on Cu(1 1 0), (1 0 0), and (1 1 1) surfaces. *Chemical Physics,* 325(2–3), pp. 519-524.

[11]   De Vries, S.A., Huisman, W.J., Goedtkindt, P., Zwanenburg, M.J., Bennett, S.L., Robinson, I.K. and Vlieg, E., 1998. Surface atomic structure of the (3×3)R30°-Sb reconstructions of Ag(111) and Cu(111). *Surface Science,* 414(1–2), pp. 159-169.

[12]   Quinn, P.D., BIttencourt, C. and Woodruff, D.P., 2002. Tensor LEED analysis of the Ni(111)($\sqrt{3}\times\sqrt{3}$)R30°-Pb surface. *Phys. Rev. B,* 65(23), pp. 233404

[13]   Bihlmayer, G., Blügel, S. and Chulkov, E.V., 2007. Enhanced Rashba spin-orbit splitting in Bi⁄Ag(111) and Pb⁄Ag(111) surface alloys from first principles. *Phys. Rev. B,* 75(19), pp. 195414.

[14] Besenbacher, F., Chorkendorff, I., Clausen, B.S., Hammer, B., Molenbroek, A.M., Nørskov, J.K. and Stensgaard, I., 1998. Design of a Surface Alloy Catalyst for Steam Reforming. *Science,* 279, pp. 1913.

[15]   Plummer, M.J., Van Ek, J. and Weller, D., 2001. *The Physics of Ultra-High-Density Magnetic Recording.* New York: Springer.

[16]   Stamenkovic, V.R., Mun, B.J., Arenz, M., Mayrhofer, K.J.J., LUCAS, C.A., WANG, G., ROSS, P.N. and MARKOVIC, N.M., 2007. Trends in electrocatalysis on extended and nanoscale Pt-bimetallic alloy surfaces. *Nature Materials,* 6, pp. 241.

[17]   Ast, C.R., Henk.J., Ernst.A., Moreschini, L., Falub, M.C., Pacilé, D., Bruno, P., Kern, K. and Grioni, M., 2007. Giant Spin Splitting through Surface Alloying. *Phys. Rev. Lett.,* 98(18), pp. 186807.

[18]   Moreschini, L., Bendounan, A., Bentmann, H., Assig, M., Kern, K., Reinert, F., Henk, J., Ast, C.R. and Grioni, M., 2009. Influence of the substrate on the spin-orbit splitting in surface alloys on (111) noble-metal surfaces. *Phys. Rev. B,* 80(3), pp. 035438.

[19]   Hofmann, P., 2006. The surfaces of bismuth: Structural and electronic properties. *Progress in Surface Science,* 81(5), pp. 191-245.

[20]   Koroteev, Y.M., Bihlmayer, G., Gayone, J.E., Chulkov, E.V., Blügel, S., Echenique, P.M. and Hofmann, P., 2004. Strong Spin-Orbit Splitting on Bi Surfaces. *Phys. Rev. Lett.,* 93(4), pp. 046403.

[21]   Hirahara, T., Nagao, T., Matsuda, I., Bihlmayer, G., Chulkov, E.V., Koroteev, Y.M., Echenique, P.M., Saito, M. and Hasegawa, S.1., 2006. Role of Spin-Orbit Coupling and Hybridization Effects in the Electronic Structure of Ultrathin Bi Films. *Phys. Rev. Lett.,* 97(14), pp. 146803.

[22]   Ast, C.R., Wittich, G., Wah, P., Vogelgesang, R., Pacilé, D., Falub, M.C., Moreschini, L., Papagno, M., Grioni, M. and Kern, K., 2007. Local detection of spin-orbit splitting by scanning tunneling spectroscopy. *Phys. Rev. B,* 75(20), pp. 201401.

[23] Mirhosseini, H., Henk, J., Ernst, A., Ostanin, S., Chiang, C.T., Yu, P., Winkelmann, A. and Kirschner, J., 2009. Unconventional spin topology in surface alloys with Rashba-type spin splitting. *Phys. Rev. B,* 79(14), pp. 245428.

[24]   Gierz1, I., Stadtmüller, B., Vuorinen, J., LIndroos, M., Meier, F., Hugo Dil, J., Kern, K. and Ast, C.R., 2010. Structural influence on the Rashba-type spin splitting in surface alloys. *Phys. Rev. B,* 81(24), pp. 245430.

[25]   Mathias, S., Ruffing, A., Deicke, F., WIesenmayer, M., Sakar, I., Bihlmayer, G., Chulkov, E.V., Koroteev, Y.M., Echenique, P.M., Bauer, M. and Aeschlimann, M., 2010. Quantum-Well-Induced Giant Spin-Orbit Splitting. *Phys. Rev. Lett.,* 104(6), pp. 066802.

[26] Zhang, K.H.L., Li, H., Mao, H., Huang, H., Ma, J., Wee, A.T.S. and Chen, W., 2010. Control of Two-Dimensional Ordering of $F_{16}CuPc$ on Bi/Ag(111): Effect of Interfacial Interactions. *J. Phys. Chem.,* 114, pp. 11234.

[27] Kresse, G. and Hafner, J., 1994. Norm-conserving and ultrasoft pseudopotentials for first-row and transition elements. *Journal of Physics: Condensed Matter,* 6(40), pp. 8245-8257.

[28] Kresse, G. and Joubert, D., 1999. From ultrasoft pseudopotentials to the projector augmented-wave method. *Physical Review B - Condensed Matter and Materials Physics,* 59(3), pp. 1758-1775.

[29] Blöchl, P.E., 1994. Projector augmented-wave method. *Physical Review B,* 50(24), pp. 17953-17979.

[30] Perdew, J.P. and Wang, Y., 1992. Accurate and simple analytic representation of the electron-gas correlation energy. *Physical Review B,* 45(23), pp. 13244-13249.

[31] Monkhorst, H.J. and Pack, J.D., 1976. Special points for Brillouin-zone integrations. *Phys. Rev. B,* 13(12), pp. 5188.

[32] Sprunger, P.T., Lægsgaard, E. and Besenbacher, F., 1996. Growth of Ag on Cu(100) studied by STM: From surface alloying to Ag superstructures. *Phys. Rev. B,* 54(11), pp. 8163.

[33] Nakagawa, T., Mitsushima, S., Okuyama, H., Nishijima, M. and Aruga, T., 2002. Evolution of geometric and electronic structure in ultrathin In films on Cu(001). *Phys. Rev. B,* 66(8), pp. 085402.

[34] Bischoff, M.M.J., Yamada, T., Quinn, A.J., Van Der Kraan, R.G.P. and Van Kempen, H., 2001. Direct Observation of Surface Alloying and Interface Roughening: Growth of Au on Fe(001). *Phys. Rev. Lett.,* 87(24), pp. 246102.

[35] Cammarata, R.C., 1994. Surface and interface stress effects in thin films. *Progress in Surface Science,* 46(1), pp. 1-38.

[36] Vitos, L., Ruban, A.V., Skriver, H.L. and Kollár, J., 1998. The surface energy of metals. *Surface Science,* 411(1–2), pp. 186-202.

[37] Stepanyuk, V.S. and Hergert, W., 2000. Energetics of surface alloying: 3*d* adatoms on the Au(100) surface. *Phys. Rev. B,* 62(11), pp. 7542.

[38] McLeod, I.M., Dhanak, V.R., Matilainen, A., Lahti, M., Pussi, K. and Zhang, K.H.L., 2010. Structure determination of the Bi−Ag(111) surface alloy using LEED I–V and DFT analyses. *Surface Science,* 604(17–18), pp. 1395-1399.

[39] Chen, C.H., Kepler, K.D., Gewirth, A.A., Ocko, B.M. and Wang, J., 1993. Electrodeposited bismuth monolayers on gold (111) electrodes: comparison of surface

x-ray scattering, scanning tunneling microscopy, and atomic force microscopy lattice structures. *J. Phys. Chem.,* 97, pp. 7290.

[40]   Nagl, C., Haller, O., Platzgummer, E., Schmid, M. and Varga, P., 1994. Submonolayer growth of Pb on Cu(111): surface alloying and de-alloying. *Surface Science,* 321(3), pp. 237-248.

[41]   Pan, W., Popescu, R., Meyerheim, H.L., Sander, D., Robach, O., Ferrer, S., Lin, M.T. and Kirschner, J., 2005. Stress and structure of $c(2\times2)$ and $p2gg(4\times2)$ Mn/Cu(001) surface alloys. *Phys. Rev. B,* 71(17), pp. 174439.

[42]   Pleth Nielsen, L., Besenbacher, F., Stensgaard, I., Lægsgaard, E., Engdahl, C., Stoltze, P. and Nørskov, J.K., 1995. "Dealloying" Phase Separation during Growth of Au on Ni(110). *Phys. Rev. Lett.,* 74(7), pp. 1159.

[43]   Zhang, H.L., Chen, W., Wang, X.S., Yuhara, J. and Wee, A.T.S., 2009. Growth of well-aligned Bi nanowire on Ag(1 1 1). *Applied Surface Science,* 256(2), pp. 460-464.

[44] Jeffrey, C.A., Zheng, S.H., Bohannan, E., Harrington, D.A. and Morin, S., 2006. X-ray characterization of as-deposited, epitaxial films of Bi(0 1 2) on Au(1 1 1). *Surface Science,* 600(1), pp. 95-105.

[45] Nagao, T., Sadowski, J.T., Saito, M., Yaginuma, S., Fujikawa, Y., Kogure, T., Ohno, T., Hasegawa, Y., Hasegawa, S. and Sakurai, T., 2004. Nanofilm Allotrope and Phase Transformation of Ultrathin Bi Film on Si(111)-7×7. *Phys. Rev. Lett.,* 93, pp. 105501.

Chapter 5

Structure Determination of the $p(\sqrt{3} \times \sqrt{3})R30°$ Bi-Ag(111) Surface Alloy Using LEED I-V and DFT Analysis

5.1 - Abstract

The deposition of 1/3 of a monolayer of Bi on Ag(111) leads to the formation of $BiAg_2$ surface alloy with a long range ordered $(\sqrt{3} \times \sqrt{3})R30°$ superstructure. A detailed analysis of this structure using LEED I-V measurements together with DFT calculations is presented. We find strong correlation between experimental and calculated LEED I-V data, with the fit between the two data sets having a Pendry's reliability factor of 0.16. The Bi atom is found to replace one top layer Ag atom in each unit cell, forming a substitutional $BiAg_2$ surface alloy, with the Bi atoms residing approximately 0.6 Å above the Ag atoms due to their size difference. DFT calculations are in good agreement with the LEED results.

5.2 - Introduction

The understanding of the growth of thin metallic films on metallic substrates has been the subject of much research over the last few years. Whilst these systems are of interest from the view point of technological applications, the growth processes can be complex, offering a range of interesting phenomena at the atomic level. This is particularly the case for the growth of semi-metal overlayers, such as Pb, Sb and Bi on metal surfaces [1-6]. Bismuth is a particularly attractive adsorbate material due to its small electron effective mass, anomalously high values of electron mean free path and mobility, highly anisotropic Fermi surface as well as having a long Fermi wavelength at room temperature, and small overlap between the conduction and valence bands [7-10]. Furthermore, the growth of Bi nanowires by vapour deposition on Ag(111) was recently reported in an STM study [11]. Such nanostructures are expected to exhibit interesting effects due to quantum confinement and finite size effects.

The Bi-Ag(111) system is very similar to that of the much studied case of Pb-Ag(111) [12-16]. Since neither Bi nor Pb are miscible with Ag, it is expected that the growth process would occur by formation of dense islands on the Ag(111) surface. However, in both cases, it is found that at 1/3 ML coverage, a $\left(\sqrt{3} \times \sqrt{3}\right)R30°$ superstructure is observed as a result of surface alloy formation, which represents a new class of materials, and is similar to what has been observed for Sb and Bi on Cu(111), Sb on Ag(111) and Pb on Ni(111) [17-25]. At higher coverages, above some critical value, a de-alloying process occurs and the monolayer growth leads to a dense plane above the Ag(111) surface. The $\left(\sqrt{3} \times \sqrt{3}\right)R30°$ structure observed for Bi and Pb on Ag(111) is of particular interest as a new class of material because the two dimensional alloy structure in both cases appears to behave like a 2-D electron gas with quantum

confinement leading to spin-orbit coupling, known as the Rashba effect, which has implications for spintronics applications [26-28]. Recently, a structural study of the $(\sqrt{3} \times \sqrt{3})R30°$ Pb-Ag(111) system using surface X-ray diffraction (SXRD) [14] and photoemission [15] has shown that the Pb atoms are embedded into the Ag top layer, forming a well ordered $PbAg_2$ surface alloy and a similar structure has been suggested for the Bi-Ag(111) system [27]. Nevertheless, a detailed investigation on the atomic structures of these 2-D surface alloys is still lacking, even though such information plays a critical role in determining the electronic structures of the surface alloys.

As mentioned above, the $(\sqrt{3} \times \sqrt{3})R30°$ surface alloy structure has also been observed for adsorbates on other fcc (111) systems and studied using a variety of techniques. In particular, Vries et al [17] used SXRD to investigate this structure for Sb-Cu(111) and Sb-Ag(111) system. The latter system has also been studied using quantitative low energy electron diffraction (LEED) [18] and impact-collision ion scattering spectroscopy [19]. Bailey et al [20] and Quinn et al [21] studied the Sb-Cu(111) and Sb-Ag(111) structures, respectively using Medium-energy ion scattering (MEIS). In these cases it was found that the correct structure was a surface alloy with a slightly 'rumpled' surface layer in which all the surface atoms occupy 'hcp' hollow sites, directly above second layer substrate atoms, rather than the 'fcc' hollow sites, confirming a stacking fault in the interface region between the top surface alloy layer and the substrate. These findings were supported by a DFT (density functional theory) total energy calculation although it was noted that there was negligible energy difference between the faulted and unfaulted surface alloy structures [22]. It was further noted that for Sb on Ag(111), the MEIS study showed that it was possible to form both the faulted and unfaulted surface structures, depending on the Sb dosing history, implying a subtle influence of subsurface Sb [21]. On the other hand, MEIS and LEED

investigation of this structure for the Pb-Ni(111) system [23,6], and a SXRD study of Bi-Cu(111) system [24] showed that the correct structure was not the faulted surface alloy but the substitutional alloy structure. The latter result was further supported by a recent DFT calculation [25].

In this paper we present a detailed atomic structure of the $(\sqrt{3} \times \sqrt{3})R30°$ Bi-Ag(111) structure using a combined LEED I-V and DFT analysis. The results show that a Bi atom is found to replace one top layer Ag atom in each unit cell, forming a substitutional unfaulted $BiAg_2$ surface alloy, with the larger Bi atoms residing about 0.6 Å above the Ag atoms due to the size difference.

5.3 - Experiment

The experiments were made in a standard ultra high vacuum (UHV) surface science chamber consisting of a PSP Vacuum Technology electron energy analyser, dual anode X-ray source, rear view LEED optics from OCI Vacuum Microengineering and an Omicron STM-1. The base pressure of the system was less than 2×10^{-10} mBar, with Hydrogen as the main residual gas in the chamber. The Ag(111) surface was prepared by cycles of Ar ion bombardment and annealing to approximately 800 K. The sample was considered clean when the LEED pattern showed sharp integer order spots and XPS did not show any traces of contamination.

Bi was deposited onto the clean Ag(111) surface from a well degassed Omicron K-cell. During deposition the Ag sample was kept at room temperature and the vacuum pressure did not exceed 3×10^{-10} mBar. The Bi was deposited at a constant rate of 0.1 ML/min until a sharp $(\sqrt{3} \times \sqrt{3})R30°$ structure was observed.

The intensity of the diffraction spots as a function of the energy of the incident electrons (LEED I-V spectra) was measured at normal incidence of the primary beam. The spectra were background subtracted and normalised with respect to the primary beam current. The intensities of the symmetrically equivalent spots were averaged in order to reduce experimental noise.

5.4 - Results and Discussion

The data set utilized consisted of 9 beams (5 integer and 4 fractional order beams) ranging from 30 eV to 330 eV and recorded at 300 K (Figure 3.1). The cumulative energy range was 1640 eV. The dynamical LEED calculations were done using the Barbieri/Van Hove SATLEED package [29]. The relativistic phase shifts were calculated using the phase shift program [30] that was packaged with SATLEED. Pendry's reliability factor, R_p, was used to quantify the agreement between experimental and calculated data and the error bars quoted were calculated using the Pendry RR-function [31]. Three different sets of phase shifts were used; one for bismuth, one for top layer Ag atoms and one for the Ag atoms in deeper layers. At the beginning of the analysis the Debye temperatures were set to 120 K and 225 K for bismuth and silver respectively, the l_{max} value was set to 8 and the imaginary part of inner potential was set to -5 eV. These values were optimized at the final stage of the analysis. The real part of the inner potential is independent of energy and was allowed to relax as is the normal procedure in the LEED analysis.
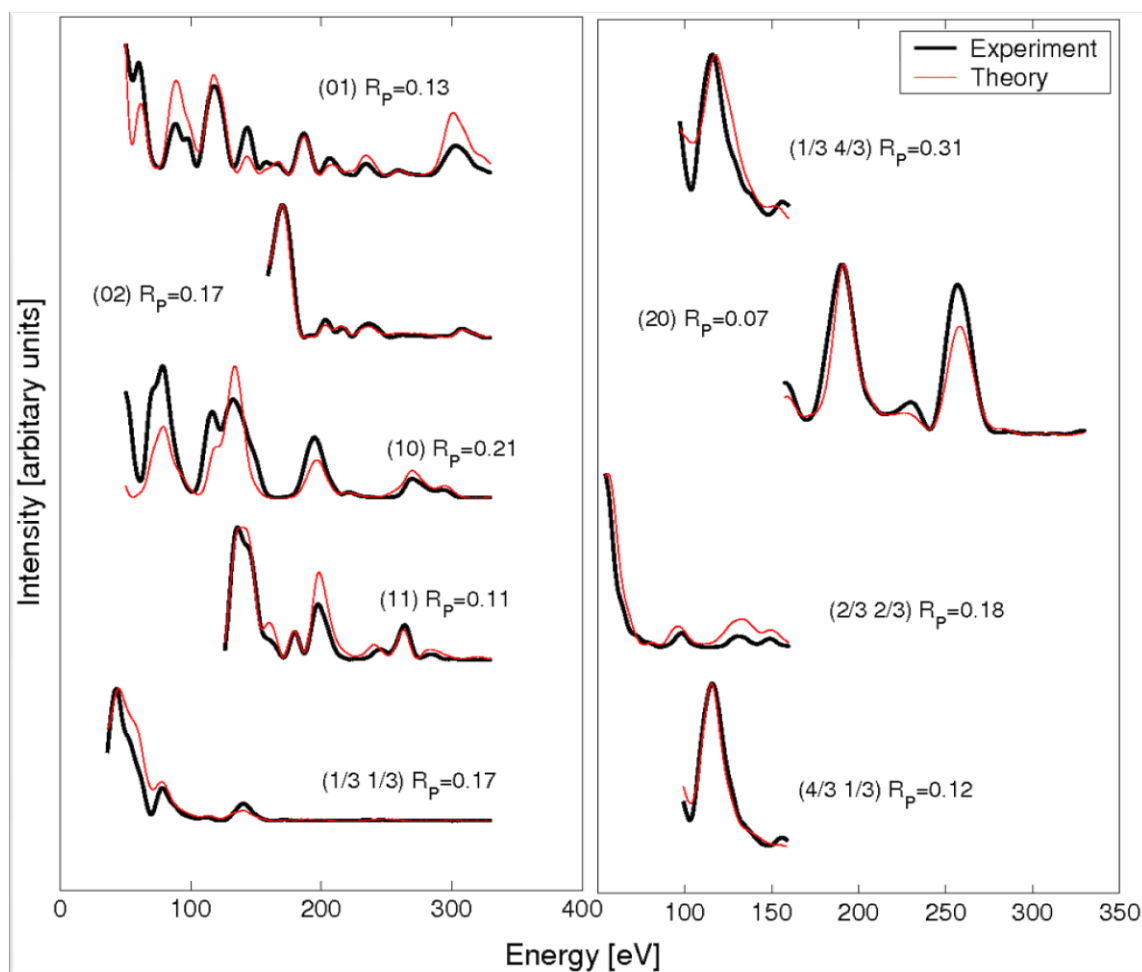
Figure 5.1 - I-V curves for the best fit structure compared with experimental data. Individual beam R-factors are shown.

Six different structural models were considered in the LEED calculations. These included four high symmetry adsorption geometries, namely the top (A) and hollows (B and C, for fcc and hcp hollows, respectively), as well as the bridge site (D), as shown in Figure 2. Adsorption at bridge site (D) lowers the symmetry of the surface, which means that proper domain averaging has to be taken into account in the LEED analysis. As well as these adsorption sites, two high symmetry substitutional alloy structures were also considered.
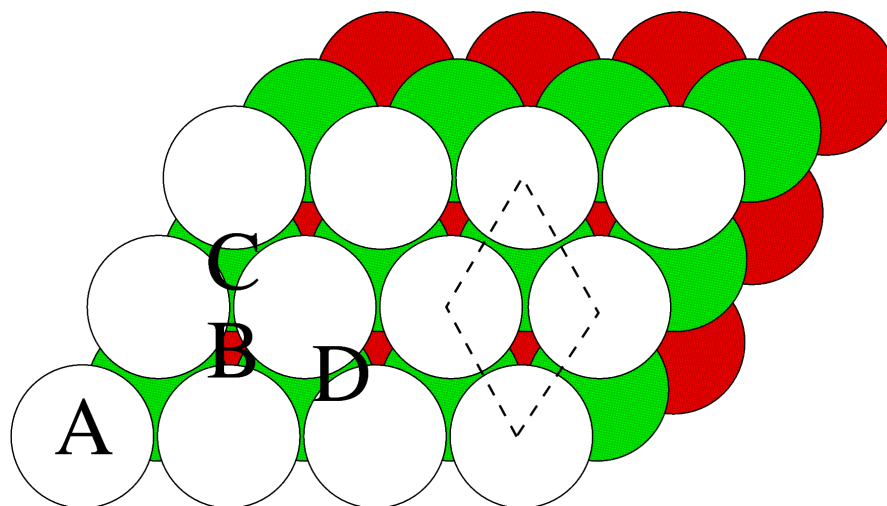
Figure 5.2 - Adsorption sites: A = top, B and C = hollow and D = bridge. Top three layers of the substrate are shown. (1x1) unit cell is shown with dashed line.

The first of these was formed by placing one Bi atom per unit cell in a substitutional position over an essentially unperturbed Ag(111) surface layer to give the $(\sqrt{3} \times \sqrt{3})R30°$ superstructure. The second was a similar surface alloy but with all the surface atoms displaced to the 'hcp' hollow sites, the so-called faulted surface alloy structure [20-22]. In Figure 5.2, the "hcp" hollow site is indicated by "C".

At the first stage of the analysis the substrate atom positions were kept fixed and the only parameters varied were the perpendicular distance between the bismuth and substrate atoms, and the real part of the inner potential. In the second stage of the analysis the bismuth atom and top five layers of the substrate were allowed to relax. In the final state of the analysis the non-structural parameters (Debye temperatures, l_{max} and imaginary part of inner potential) were optimized.

The Pendry R-factors from different stages of analysis are listed in Table 5.1. After each stage, structures that have a Pendry R-factor less than the sum of the minimum R-factor

Adsorption site	R-factor (1st stage)	R-factor (final)	Adsorption energy (eV)
Top (A)	0.52		0.414
Hollow (B)	0.54		0.198
Hollow (C)	0.50		0.234
Bridge (D)	0.41		0.208
Faulted Surface alloy	0.58		-0.354
Surface alloy	**0.27**	**0.16**	**-0.353**
Pendry variance	*0.04*		

Table 5.1 - Pendry R-factors from LEED analysis and adsorption energies from DFT calculations, for different adsorption geometries. Positive adsorption energy indicates that the adsorption is unfavourable, whilst a negative value indicates that adsorption is likely, with the lowest value being the most stable. Letters in parentheses refer to the Bi atom adsorption sites shown in Figure 5.1.

and Pendry variance were selected to be optimized further. The substitutional surface alloy model was clearly most favourable after the 1st stage, consistent with the structure previously suggested by C.R. Ast *et al.* [27], rendering it unnecessary to further optimize the other structures. The faulted surface alloy in which all the surface atoms

occupy 'hcp' hollow sites was found to be the least favourable structure. Structural and non-structural parameters for the alloyed structure are listed in Table 2 together with the results from our DFT analysis (see below). Top and side views of the structure are shown in Figure 5.3. The corresponding best fit I-V curves are shown in Figure 5.1. The final R-factor reached was 0.16. It is also noted that the optimized structure incorporates a slight buckling of the fourth layer of the silver substrate. This is interesting because for the similar $\left(\sqrt{3} \times \sqrt{3}\right)R30°$ Pb/Ag(111) structure, Dalmas *et al* [14] suggest a slight out of plane distortion of the Ag atoms in the top surface layer based on STM and SXRD measurements. They attribute this to a possible Peierls type distortion, although they do note that this distortion could be an effect of their measurements. The overall structure remains bulk like with a small contraction of the top layers.

First-principles DFT calculations were performed for the bismuth on Ag(111) system to verify and analyze the experimental results presented in this paper. The static calculations for total energies were performed using the Vienna ab-initio simulation package (VASP) [32-35] including the projector augmented wave (PAW) [36] potentials. A kinetic energy cut-off of 400 eV was applied for the plane waves, which was found to produce converged results for both Ag and Bi, for all the structures. For the exchange correlation potential the generalized gradient approximation (GGA) of the Perdew-Wang 91 (PW91) [37] was employed. The 10 x 8 x 1 Monkhorst- Pack mesh [38] was used for k-point sampling. The Ag surface was modelled using the supercell approach, where periodic boundary conditions are applied to the central supercell so that it is reproduced periodically throughout xy-space. The surface slab was modelled with 6 layers of Ag atoms. A region
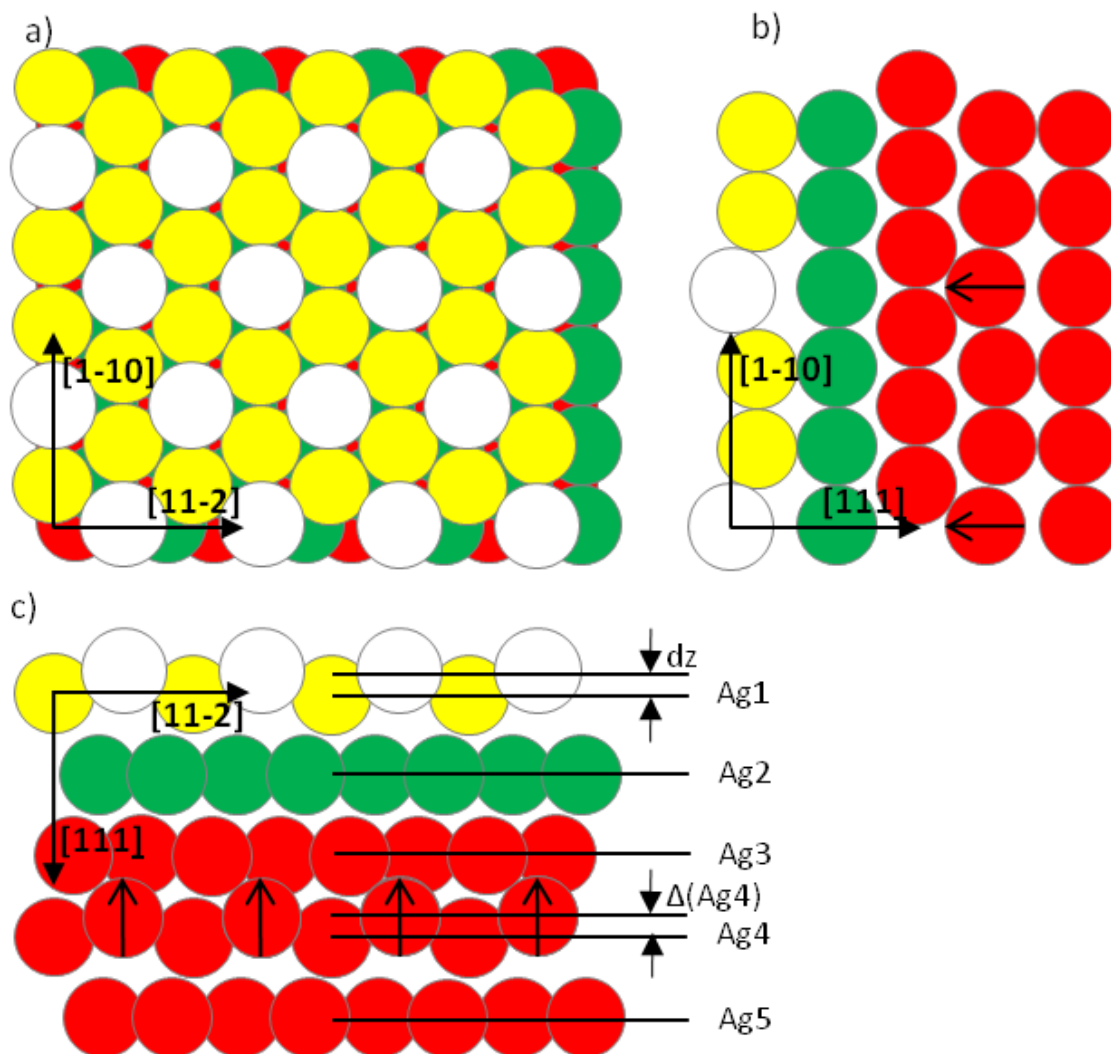
Figure 5.3 - Large white circles represent the Bi atoms that substitute Ag atoms in the top layer. (a) Top view of the favoured structure. Top three layers of the slab are shown. (b, c) Side views showing the top five layers. The arrows show the buckling in the 4th substrate layer as the Ag atoms directly below the Bi are displaced vertically up.

of approximately 10 Å of vacuum was inserted in the z direction to prevent interactions occurring between periodic images. The bottommost layer of the surface slab was frozen during the geometry relaxation.

Adsorption energies of Bi atom are defined as:

$$E_{ads} = 1/N_{Bi} \times (E_{tot} - E_{clean} - N_{Bi} \times E_{Bi}) \quad (5.1)$$

Where E_{tot} is total energy of relaxed Ag/Bi supercell, E_{clean} is the total energy of the relaxed clean Ag slab, N_{Bi} is the number of Bi atoms and E_{Bi} is the energy of one atom in the Bi bulk.

For substitutional alloy structures the adsorption energy is defined as:

$$E_{ads} = 1/N_{Bi} \times (E_{tot} - E_{clean} - N_{Bi} \times E_{Bi} + N_{Bi} \times E_{Ag\text{-}bulk}) \qquad (5.2)$$

where, $E_{Ag\text{-}bulk}$ is the total energy of an Ag bulk atom.

An Ag lattice constant of 4.17 Å was used, which was obtained from bulk cell optimization using the same computational parameters. The six structural models used in the LEED I-V analysis were considered in the DFT analysis. The adsorption energies for each site for the models that showed convergence in the calculations are listed in Table 5.1. Of the overlayer geometries, the fcc hollow site is the most favourable, albeit with small energy difference between the two hollows and the bridge sites. On the other hand, both the substitutional and faulted surface alloy structures were found to be the most stable with an adsorption energy of -0.353 eV. The geometrical parameters for the relaxed substitutional surface alloy structure are listed in Table 5.2 and compare well with the LEED data.

While the LEED analysis unambiguously favours the unfaulted substitutional surface alloy, the DFT calculations only confirm that the structure is a surface alloy and does not distinguish between the faulted structure, where all the top surface atoms (Bi and Ag) have moved into hcp hollow sites, and the unfaulted surface alloy, where the surface atoms remain in fcc hollow sites. One possible reason why our DFT calculations fail to distinguish between the two structures is the use of the finite size of the slab (6 layers).

Parameter	LEED	DFT
d(Ag-Bi) [Å]	2.95±0.05	3.01
dz(Ag-Bi) [Å]	0.57±0.05	0.61
dz/dz$_{bulk}$(Ag1-Ag2) [%]	-1±1	-1
dz/dz$_{bulk}$(Ag2-Ag3) [%]	-1±1	0
dz/dz$_{bulk}$(Ag3-Ag4) [%]	-1±2	-1
dz/dz$_{bulk}$(Ag4-Ag5) [%]	-1±2	0
Δ (Ag4) [Å]	0.02±0.05	0.02
Debye T (Bi) [K]	80	
Debye T (Ag1) [K]	160	
Debye T (Ag bulk) [K]	225	
V$_{imaginary}$ [eV]	-4.5	
l$_{max}$	13	
Ag bulk lattice constant [Å]	4.09	4.17

Table 5.2 - Structural and non-structural parameters from LEED and DFT analysis. d(Bi-Ag) is the bond length between Bi and Ag atoms in the first layer, dz(Ag-Bi) is the vertical distance between the 1st layer Ag atoms and the Bi atoms (Bi is above Ag), dz/dz$_{bulk}$(Ag i -Ag j) is the change in the vertical distance between the centres of mass of Ag layers i and j (negative means contraction). Δ (Ag4) is the buckling in the 4th substrate layer where the Ag atoms directly below the Bi atoms are pulled up a slightly. Using a bulk interlayer spacing for clean Ag(111) of 2.35Å, the LEED results show that the overall structure remains bulk like within the errors.

Indeed, in an earlier DFT calculation by Woodruff and Robinson [22] for the Sb-Ag(111) system, they find that the stacking fault energy is sensitive to the slab thickness and suggest that these calculations are only realistic using much larger scale parallel computing systems beyond our means. It is also worth noting that even for the clean Ag(111) surface, they find that there is a negligible difference in energy between the surface faulted and unfaulted structures. Our calculation for the clean Ag(111) shows that the energy difference between the faulted and unfaulted Ag surface is only 20 meV, similar to what has previously been reported [22]. This implies that on Ag(111), a stacking fault surface structure could easily be facilitated. In fact for Sb on Ag(111), both faulted and unfaulted $(\sqrt{3} \times \sqrt{3})R30°$ structures have been found, as well as evidence for subsurface stacking faults, attributed to some subtle influence of subsurface Sb. For the Bi on Ag(111) case, we have only found the unfaulted $(\sqrt{3} \times \sqrt{3})R30°$ structure, suggesting perhaps that Bi, with its larger atomic size compared to Sb, does not easily diffuse into the subsurface region. Another factor could be that there is a thermal activation barrier in moving all the surface atoms from the fcc hollow sites to the hcp hollow sites. In fact the Sb on Ag(111) structures were formed by dosing and annealing to elevated temperatures while in our case, sharp $(\sqrt{3} \times \sqrt{3})R30°$ Bi on Ag(111) structure was readily formed by dosing at room temperature.

The substitutional and faulted surface alloy structures were further investigated theoretically by molecular dynamics calculations. The calculations were performed by fixing the surface temperature at 300 K, and the ionic moves were performed with the interval of 1 fs. The total duration of molecular dynamics runs was 1 ps. The relaxed atomic positions were used as initial coordinates for the molecular dynamics. In the beginning of each molecular dynamics run, random velocities were assigned to the slab

atoms according to the temperature distribution. The bottommost atoms of the slab were kept fixed. The results of the molecular dynamics show that both of the structures, surface alloy and faulted surface alloy, are stable at room temperature, as found in the DFT calculations. Both calculations were tested with several random velocities for the slab atoms, and the results remained the same. Moreover, the adsorption energies stayed within the same interval in both cases during the molecular dynamics run.

Both the LEED and DFT analysis show that in the stable substitutional surface alloy structure, there is a slight 'rumpling' of the surface due to the larger Bi atoms located about 0.6 Å above the surface plane of the Ag atoms. This amplitude of the 'rumpling' is smaller by about 0.24 Å than that predicted by a simple touching hard-spheres model based on bulk metallic radii (1.44 Å for Ag and 1.56 Å for Bi). This suggests a reduction in the effective radii similar to that found by Quinn *et al* [6] in their LEED study of the substitutional surface alloy structure for the Pb-Ni(111) system. It has been suggested that the reduction in the effective radii may be attributed to the influence of valance electron charge smoothing and associated surface stress effects [6,21,23]. A similar effect is possibly the case for the Bi-Ag(111) structure in our study.

5.5 - Conclusions

There is very good agreement between the geometrical parameters extracted from LEED I-V and DFT analyses. LEED analysis shows that the Bi atoms are found to replace one top layer Ag atom in each unit cell, forming a substitutional unfaulted surface alloy. DFT calculations show that the stable $(\sqrt{3} \times \sqrt{3})R30°$ structure is a surface alloy, but does not distinguish between a faulted and unfaulted structure,

possibly due to limitation of using a finite size slab. Because of the size difference between the Ag and Bi atoms (Bi is approximately 5% larger than Ag), the top layer is corrugated such that the Bi atoms reside about 0.6 Å above the Ag atoms. The amplitude of this 'rumpling' is smaller than what would be predicted on a simple touching hard-spheres model. The interlayer spacings, calculated with respect to the centres of mass of the Ag atoms, remain bulk like in both DFT and LEED analyses.

5.6 – References

[1] Li, D.F., Xiao, H.Y., Zu, X.T. and Dong, H.N., 2007. First-principles study of the Ni(1 1 1)()R30°–Pb surface. *Physica B: Condensed Matter,* 392(1–2), pp. 217-220.

[2] J Nie, J.L., Xiao, H.Y., Zu, X.T. and Gao, F., 2006. First principles calculations on Na and K-adsorbed diamond(1 0 0) surface. *Chemical Physics,* 326(2–3), pp. 308-314.

[3] Xiao, H.Y., Zu, X.T., He, X. and Gao, F., 2006. Sb adsorption on Cu(1 1 0), (1 0 0), and (1 1 1) surfaces. *Chemical Physics,* 325(2–3), pp. 519-524.

[4] Nascimento, V.B., Paniago, R., De Siervo, A., De Castilho, C.M.C., landers, R., Soares, E.A. and De Carvalho, V.E., 2004. Structural study of the Ag(1 1 0)c(2 × 2)–Sb phase by low energy electron diffraction. *Surface Science,* 572(2–3), pp. 337-346.

[5] Krupski, A. and Mróz, S., 2003. Leed Investigation of the Pb And Sb Ultrathin Layers Deposited On The Ni(111) face at T=150–900 K. *Surface Review and Letters,* 10(06), pp. 843-848.

[6] Quinn, P.D., Bittencourt, C. and Woodruff, D.P., 2002. Tensor LEED analysis of the Ni(111)($\sqrt{3}\times\sqrt{3}$)R30°-Pb surface. *Phys. Rev. B,* 65(23), pp. 233404

[7] Hofmann, P., 2006. The surfaces of bismuth: Structural and electronic properties. *Progress in Surface Science,* 81(5), pp. 191-245.

[8] Xu, J.H., Wang, E.G., Ting, C.S. and Su, W.P., 1993. Tight-binding theory of the electronic structures for rhombohedral semimetals. *Phys. Rev. B,* 48(23), pp. 17271.

[9] Yang, F.Y., Liu, K., Hong, K., Reich, D.H., Searson, P.C. and Chien, C.L., 1999. Large Magnetoresistance of Electrodeposited Single-Crystal Bismuth Thin Films. *Science,* 284(5418), pp. 1335-1337.

[10] Black, M.R., Hagelstein, P.L., Cronin, S.B., Lin1, Y.M. and Dresselhaus, M.S., 2003. Optical absorption from an indirect transition in bismuth nanowires. *Phys. Rev. B,* 68(23), pp. 235417

[11] Zhang, H.L., Chen, W., Wang, X.S., Yuhara, J. and Wee, A.T.S., 2009. Growth of well-aligned Bi nanowire on Ag(1 1 1). *Applied Surface Science,* 256(2), pp. 460-464.

[12] Takayanagi, K., Kolb, D.M., Kambe, K. and LehmpfuhL, G., 1980. Deposition of monolayer and bulk lead on Ag(111) studied in vacuum and in an electrochemical cell. *Surface Science,* 100(2), pp. 407-422.

[13] Rolland, A., Bernardini, J. and Barthes-Labrousse, M.G., 1984. Vapour deposition of lead on Ag(111) and equilibrium surface segregation from Ag☐Pb(111) solid solutions: A leed-aes comparative study. *Surface Science,* 143(2–3), pp. 579-590.

[14] Dalmas, J., Oughaddou, H., Léandri, C., Gay, J., Le Lay, G., Tréglia, G., Aufray, B., Bunk, O. and Johnson, R.L., 2005. Ordered surface alloy formation of immiscible metals: The case of Pb deposited on Ag(111). *Phys. Rev. B,* 72(15), pp. 155424.

[15] Dalmas, J., Oughaddou, H., Le Lay, G., Aufray, B., Tréglia, G., Girardeaux, C., Bernardini, J., Fujii, J. and Panaccione, G., 2006. Photoelectron spectroscopy study of Pb/Ag(1 1 1) in the submonolayer range. *Surface Science,* 600(6), pp. 1227-1230.

[16] Pacilé, D., Ast, C.R., Papagno, M., Da Silva, C., Moreschini, L., Falub, M., Seitsonen, A.P. and Grioni, M.1., 2006. Electronic structure of an ordered Pb∕Ag(111) surface alloy: Theory and experiment. *Phys. Rev. B,* 73(24), pp. 245429.

[17] De Vries, S.A., Huisman, W.J., Goedtkindt, P., Zwanenburg, M.J., Bennett, S.L., Robinson, I.K. and Vlieg, E., 1998. Surface atomic structure of the (3×3)R30°-Sb reconstructions of Ag(111) and Cu(111). *Surface Science,* 414(1–2), pp. 159-169.

[18] Soares, E.A., Bittencourt, C., Nascimento, V.B., De Carvalho, V.E., De Castilho, C.M.C., McConville, C.F., De Carvalho, A.V. and Woodruff, D.P., 2000. Structure determination of Ag(111)(v3× v3)R30°-Sb by low-energy electron diffraction. *Physical Review B - Condensed Matter and Materials Physics,* 61(20), pp. 13983-13987.

[19] Noakes, T.C.Q., Hutt, D.A., McConville, C.F. and Woodruff, D.P., 1997. Structural investigation of ordered Sb adsorption phases on Ag(111) using coaxial impact collision ion scattering spectroscopy. *Surface Science,* 372(1–3), pp. 117-131.

[20] Bailey, P., Noakes, T.C.Q. and Woodruff, D.P., 1999. A medium energy ion scattering study of the structure of Sb overlayers on Cu(111). *Surface Science,* 426(3), pp. 358-372.

[21] Quinn, P.D., Brown, D., Woodruff, D.P., Bailey, P. and Noakes, T.C.Q., 2002. Structural study of the adsorption of Sb on Ag(1 1 1) using medium energy ion scattering. *Surface Science,* 511(1–3), pp. 43-56.; see also Woodruff, D.P., Muñoz-Márquez, M.A. and Tanner, R.E., 2003. Structural studies at metallic surfaces and interfaces using MEIS. *Current Applied Physics,* 3(1), pp. 19-24.

[22] Woodruff, J.P. and Robinson, J., 2000. Sb-induced surface stacking faults at Ag(111) and Cu(111) surfaces: density-functional theory results. *Journal of Physics: Condensed Matter,* 12(35), pp. 7699.

[23] Brown, D., Quinn, P.D., Woodruff, D.P., Bailey, P. and Noakes, T.C.Q., 2000. Medium-energy ion scattering structural study of the Ni(111)(v3×v3)R30°-Pb surface phase. *Physical Review B - Condensed Matter and Materials Physics,* 61(11), pp. 7706-7715.

[24] Kaminski, D., Poodt, P., Aret, E., Radenovic, N. and vlieg, E., 2006. Observation of a Liquid Phase with an Orthorhombic Orientational Order. *Phys. Rev. Lett.,* 96(5), pp. 056102.

[25] Li, D.F., Xiao, H.Y., Zu, X.T. and Dong, H.N., 2007. First-principles study of the Ni(1 1 1)()R30°–Pb surface. *Physica B: Condensed Matter,* 392(1–2), pp. 217-220.

[26] Meier, F., Dil, H., Lobo-Checa, J., Patthey, L. and Osterwalder, J., 2008. Quantitative vectorial spin analysis in angle-resolved photoemission: Bi∕Ag(111) and Pb∕Ag(111). *Phys. Rev. B,* 77(16), pp. 165431.

[27] Ast, C.R., Henk, J., Ernst, A., Moreschini, L., Falub, M.C., Pacilé, D., Bruno, P., Kern, K. and Grioni, M., 2007. Giant spin splitting through surface alloying. *Physical Review Letters,* 98(18), pp. 186807.

 [28] He, K., Hirahara, T., Okuda, T., Hasegawa, S., Kakizaki, A. and Matsuda, I., 2008. Spin Polarization of Quantum Well States in Ag Films Induced by the Rashba Effect at the Surface. *Phys. Rev. Lett.,* 101(10), pp.107604.

[29] Van Hove, M.A., Moritz, W., Over, H., Rous, P.J., Wander, A., Barbieri, A., Materer, N., Starke, U. and Somorjai, G.A., 1993. Automated determination of complex surface structures by LEED. *Surface Science Reports,* 19(3-6), pp. 191-229.

[30] A. Barbieri and M. A. Van Hove, private communication.

[31] Pendry, J.B., 1980. Reliability factors for LEED calculations. *Journal of Physics C: Solid State Physics,* 13(5), pp. 937-944.

[32] Kresse, G. and Hafner, J., 1994. Norm-conserving and ultrasoft pseudopotentials for first-row and transition elements. *Journal of Physics: Condensed Matter,* 6(40), pp. 8245-8257.

[33] Kresse, G. and Furthmüller, J., 1996. Efficiency of ab-initio total energy calculations for metals and semiconductors using a plane-wave basis set. *Computational Materials Science,* 6(1), pp. 15-50.

[34] Kresse, G. and Furthmüller, J., 1996. Efficient iterative schemes for *ab initio* total-energy calculations using a plane-wave basis set. *Phys. Rev. B,* 54(16), pp. 11169.

[35] Kresse, G. and Joubert, D., 1999. From ultrasoft pseudopotentials to the projector augmented-wave method. *Physical Review B - Condensed Matter and Materials Physics,* 59(3), pp. 1758-1775.

[36] Blöchl, P.E., 1994. Projector augmented-wave method. *Physical Review B,* 50(24), pp. 17953-17979.

[37] Perdew, J.P. and Wang, Y., 1992. Accurate and simple analytic representation of the electron-gas correlation energy. *Physical Review B,* 45(23), pp. 13244-13249.

[38] Monkhorst, H.J. and Pack, J.D., 1976. Special points for Brillouin-zone integrations. *Phys. Rev. B,* 13(12), pp. 5188.

Chapter 6

LEED I-V and DFT Structure Determination of the

(√3x√3)R30° Pb-Ag(111) Surface Alloy

6.1 - Abstract

The deposition of 1/3 of a monolayer of Pb on Ag(111) leads to the formation of PbAg$_2$ surface alloy with a long range ordered $(\sqrt{3} \times \sqrt{3})R30°$ superstructure. A detailed analysis of this structure using LEED I-V measurements together with DFT calculations is presented. We find strong correlation between experimental and calculated LEED I-V data, with the fit between the two data sets having a Pendry's reliability factor of 0.21. The Pb atom is found to replace one top layer Ag atom in each unit cell, forming a substitutional PbAg$_2$ surface alloy, as expected, with the Pb atoms residing approximately 0.4 Å above the Ag atoms due to their size difference. DFT calculations are in good agreement with the LEED results.

6.2 - Introduction

The formation of surface alloys when a metal is deposited on a metal substrate is by no means an unusual phenomenon. In fact, even where the two metals in question are immiscible in the bulk, the formation of a surface alloy is not uncommon, giving rise to both interesting and useful properties, particularly in the case of post-transition metals such as Pb, Sb and Bi [1-7]. These properties include potential applications in catalysis, corrosion resistance, surface hardening or for their electronic properties which can lead to novel effects such as spin splitting. As such, they have received considerable interest in recent years and continue to do so. Pb thin film growth is also of interest for use as a surfactant to promote 2D layer by layer growth as has been reported in numerous recent studies [8-11]. Furthermore, as an adsorbate at higher coverage, the growth of Pb films can lead to the formation of nano-sized structures due to quantum confinement and finite size effects which in turn can lead to some novel effects [12-14].

The deposition of Pb on Ag(111) gives rise to a $(\sqrt{3} \times \sqrt{3})R30°$ surface alloy at approximately 1/3 monolayer (ML) coverage, then, after some critical coverage a de-alloying process occurs. Here we focus our attention on the $(\sqrt{3} \times \sqrt{3})R30°$ structure. This $(\sqrt{3} \times \sqrt{3})R30°$ structure is seen in other systems on fcc(111) substrates [15-21] and in fact Ast *et al* [22] recently identified these surface alloys between heavy metals and noble metals as a new class of materials having long range order and exhibiting large spin splitting of their surface states. The main factors leading to their formation are the relative surface energy of the pure elements, their relative atomic size and the interactions between adsorbate-adsorbate and adsorbate-substrate atoms [23]. The alloys are formed by a direct substitution of every third atom in the surface layer by an adsorbate atom meaning the unit cell of the surface layer contains three atoms instead

of one, as previously the case. In instances where the adsorbate atoms are significantly larger than those of the substrate, a 'rumpling' of the surface layer is seen with the adsorbate atoms slightly raised above those of the substrate due to their size mismatch. It is worth noting that this rumpling is often less than that predicted using a hard spheres model based on atomic radii. In addition to this, in some systems, such as the $\left(\sqrt{3} \times \sqrt{3}\right)R30°$ Sb-Cu(111), Sb-Ag(111) [24], a stacking fault is induced by the alloy formation. This so called stacking fault is where the whole top layer of atoms moves from the fcc hollow sites to the hcp hollows. It is not clear why a stacking fault manifests in some of these systems but possibly there is a role played by sub-surface species of adatoms [24].

The case of Pb/Ag(111) has, in fact, been the subject of recent studies both from a structural and electronic point of view [25-26]. Interestingly, Dalmas *et al.* [27] reported a rumpling not only between the Pb and Ag atoms in the surface layer but also between the two Ag atoms in the unit cell of this surface layer, as seen with scanning tunneling microscopy (STM). They speculated this phenomenon was induced by a Pierls type distortion although such an effect has not been seen in any similar systems. Given the interest in these materials for properties such as the Rashba effect and the fact that Rashba energies can be tuned with small changes in surface composition and structure [28-29], as well as the unusual nature of the rumpling, we have carried out this further structural study on the system.

In this paper we present a detailed atomic structure of the $\left(\sqrt{3} \times \sqrt{3}\right)R30°$ Pb-Ag(111) structure using a combined LEED I-V and DFT analysis. The results show that a Pb atom is found to replace one top layer Ag atom in each unit cell, forming a substitutional unfaulted $PbAg_2$ surface alloy, with the larger Pb atoms residing about

0.4 Å above the Ag atoms due to the size difference. The results also indicate that the Dalmas model with surface Ag rumpling is slightly less favourable than the model where the Ag atoms remain in their normal positions relative to one another.

6.3 - Experiment

The experiments were conducted in a standard ultra high vacuum (UHV) surface science chamber consisting of a PSP Vacuum Technology electron energy analyser, dual anode X-ray source, rear view LEED optics from OCI Vacuum Microengineering and an Omicron STM-1. The base pressure of the system was less than 2×10^{-10} mBar, with Hydrogen as the main residual gas in the chamber. The Ag(111) surface was prepared by cycles of Ar^+ ion bombardment and annealing to approximately 750 K. The sample was considered clean when the LEED pattern showed sharp integer order spots and XPS did not show any traces of contamination.

Pb was deposited onto the clean Ag(111) surface from a well degassed Omicron K-cell. During deposition the Ag sample was kept at room temperature and the vacuum pressure did not exceed 3×10^{-10} mBar. The Pb was deposited at a constant rate of 0.1 ML/min.

The intensity of the diffraction spots as a function of the energy of the incident electrons (LEED I-V spectra) was measured at normal incidence of the primary beam with the sample cooled to around 150 K. The spectra were background subtracted and normalised with respect to the primary beam current. The intensities of the symmetrically equivalent spots were averaged in order to reduce experimental noise.

6.4 - Results and Discussion

The data set utilized consisted of 9 beams (5 integer and 4 fractional order beams) ranging from 30 eV to 400 eV and recorded at 150 K (Figure 6.1). The cumulative energy range was 1738 eV. The dynamical LEED calculations were done using the Barbieri/Van Hove SATLEED package [30]. The relativistic phase shifts were calculated using the phase shift program [31] that was packaged with SATLEED. Pendry's reliability factor, R_p, was used to quantify the agreement between experimental and calculated data and the error bars quoted were calculated using the Pendry RR-function [32]. Three different sets of phase shifts were used; one for lead, one for top layer Ag atoms and one for the Ag atoms in deeper layers. At the beginning of the analysis the Debye temperatures were set to 105 K and 225 K for lead and silver respectively, the l_{max} value was set to 11 and the imaginary part of inner potential was set to -5 eV. These values were optimized at the final stage of the analysis. The real part of the inner potential is independent of energy and was allowed to relax as is the normal procedure in the LEED analysis.

Six different structural models were considered in the LEED calculations. These included four high symmetry adsorption geometries, namely the top (A) and hollows (B and C, for fcc and hcp hollows, respectively), as well as the bridge site (D), as shown in Figure 6.2. Adsorption at bridge site (D) lowers the symmetry of the surface, which means that proper domain averaging has to be taken into account in the LEED analysis. As well as these adsorption sites, two high symmetry substitutional alloy structures were also considered. The first of these was formed by placing one Pb atom per unit cell in a substitutional position over an essentially unperturbed Ag(111) surface layer to
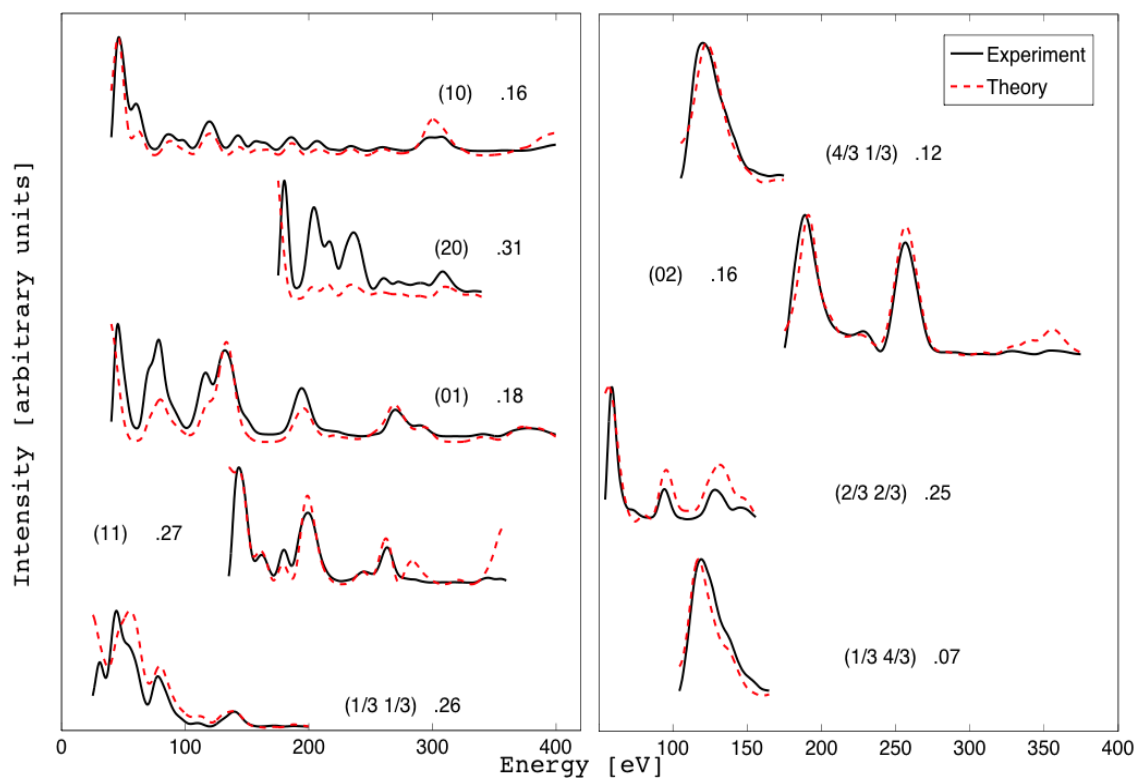
Figure 6.1 - I-V curves for the best fit structure compared with experimental data. Individual beam R-factors are shown.

give the $(\sqrt{3}x\sqrt{3})R30°$ superstructure. The second was a similar surface alloy but with all the surface atoms displaced to the 'hcp' hollow sites, the so-called faulted surface alloy structure [5,7]. In Figure 6.2, the "hcp" hollow site is indicated by "C".

At the first stage of the analysis the substrate atom positions were kept fixed and the only parameters varied were the perpendicular distance between the lead and substrate atoms, and the real part of the inner potential. In the second stage of the analysis the lead atom and top five layers of the substrate were allowed to relax. In the third stage of the analysis the non-structural parameters (Debye temperatures, l_{max} and imaginary part of inner potential) were optimized. Finally, in order to test the Dalmas model, the Ag

Figure 6.2 - Adsorption sites: A = top, B =HCP hollow, C = FCC hollow and D = bridge. Top three layers of the substrate are shown. Arrow show atoms shifted into the HCP stacking fault position.
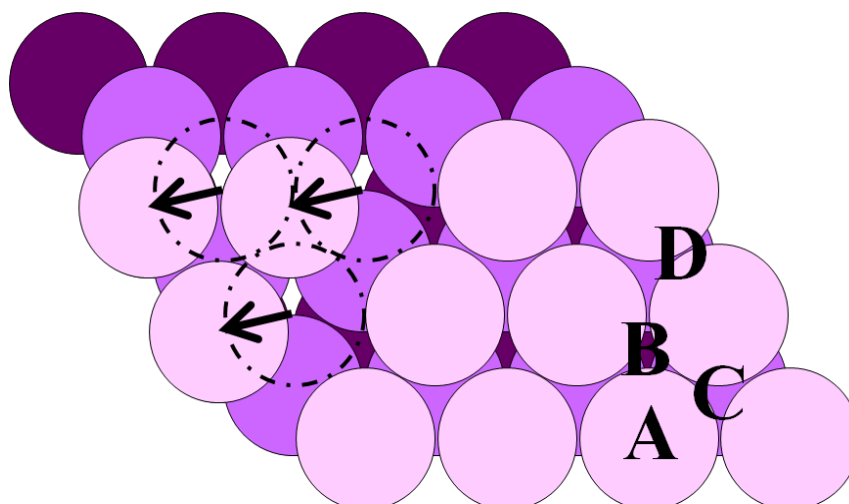
atoms in the unit cell of the surface layer were allowed to move independently of one another.

The Pendry R-factors from different stages of analysis are listed in Table 6.1. After each stage, structures that have a Pendry R-factor less than the sum of the minimum R-factor and Pendry variance were selected to be optimized further. The substitutional surface alloy model was clearly most favourable after the 1st stage, consistent with the structure suggested by previous studies [25-26] rendering it unnecessary to further optimize the other structures. Once the favoured structure was optimized the Ag atoms in the unit cell of the surface layer were allowed to move independently of one another. Since the model with surface Ag rumpling is lower symmetry there are more free parameters and hence one would expect to see a lower R-factor. In fact, allowing the Ag atoms to move independently, the program gave a 0.06 Å rumpling between the Ag atoms as the optimum structure. However, the R-factor for this structure is the same as for the un-rumpled structure (0.21). Based on LEED I-V one cannot really categorically say if the Dalmas model is real or not. One thing that must be remembered is that if the

Adsorption site	R-factor (1st stage)	R-factor (final)	Adsorption energy (eV)
Top (A)	0.55		0.335
Hollow (B)	0.58		0.092
Hollow (C)	0.54		0.215
Bridge (D)	0.46		0.140
Faulted Surface alloy	0.57		-0.275
Surface alloy	**0.25**	**0.21**	**-0.290**
Pendry variance	*0.04*		

Table 6.3- Pendry R-factors from LEED analysis and adsorption energies from DFT calculations, for different adsorption geometries. Positive adsorption energy indicates that the adsorption is unfavourable, whilst a negative value indicates that adsorption is likely, with the lowest value being the most stable. Letters in parentheses refer to the Pb atom adsorption sites shown in Figure 6.1.

Dalmas model were real, that would require domain averaging (the LEED pattern should be a combination of two domains related by a mirror plane). Structural and non-structural parameters for the unrumpled, alloyed structure are listed in Table 6.2 together with the results from our DFT analysis (see below).

Top and side views of the structure are shown in Figure 6.3 along with a LEED image of the structure. The corresponding best fit I-V curves are shown in Figure 6.1. The final R-factor reached was 0.21. It is also noted that the optimized structure incorporates a slight buckling of the fourth layer of the silver substrate. The overall structure remains bulk like with a small contraction of the top layers.

First-principles DFT calculations were performed for the lead on Ag(111) system to verify and analyze the experimental results presented in this paper. The static

calculations for total energies were performed using the Vienna ab-initio simulation package (VASP) [33-36] including the projector augmented wave (PAW) [37] potentials.

Parameter	LEED	DFT
d(Ag-Pb) [Å]	2.90±0.06	3.01
dz(Ag-Pb) [Å]	0.42±0.06	0.59
dz/dz_{bulk}(Ag1-Ag2) [%]	0±1	-1
dz/dz_{bulk}(Ag2-Ag3) [%]	0±1	0
dz/dz_{bulk}(Ag3-Ag4) [%]	-1±2	0
dz/dz_{bulk}(Ag4-Ag5) [%]	-1±3	0
Δ (Ag4) [Å]	0.02±0.10	0.02
Debye T (Pb) [K]	85	
Debye T (Ag1) [K]	160	
Debye T (Ag bulk) [K]	225	
$V_{imaginary}$ [eV]	-5	
l_{max}	11	
Ag bulk lattice constant [Å]	4.09	4.17

Table 6.4 - **Structural and non-structural parameters from LEED and DFT analysis. d(Pb-Ag) is the bond length between Pb and Ag atoms in the first layer, dz(Ag-Pb) is the vertical distance between the 1st layer Ag atoms and the Pb atoms (Pb is above Ag), dz/dz_{bulk}(Ag i -Ag j) is the change in the vertical distance between the centres of mass of Ag layers i and j (negative means contraction). Δ (Ag4) is the buckling in the 4th substrate layer where the Ag atoms directly below the Pb atoms are pulled up a slightly. Using a bulk interlayer spacing for clean Ag(111) of 2.35Å, the LEED results show that the overall structure remains bulk like within the errors.**
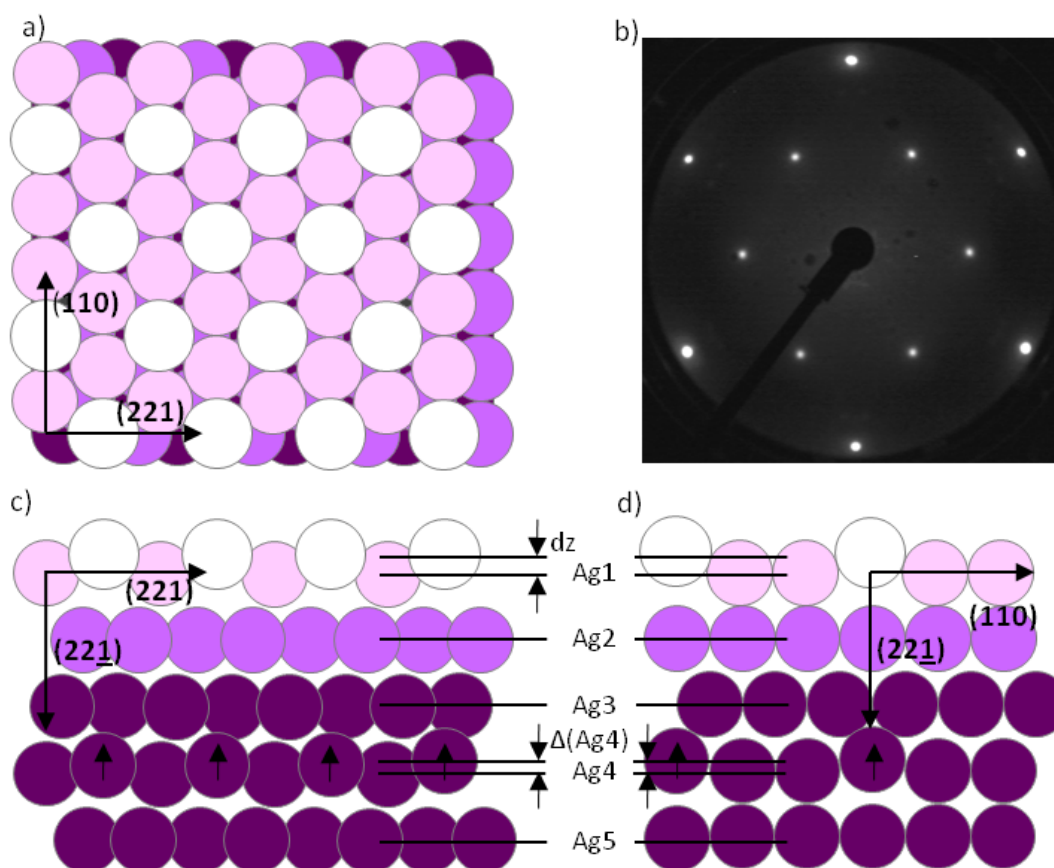
Figure 6.3 - Large white circles represent the Pb atoms that substitute Ag atoms in the top layer. *(a)* Top view of the favoured structure. Top three layers of the slab are shown. *(b)* Corresponding LEED image taken at 46 eV. The outer spots are the (1,0) and (0,1) substrate spots and the inner spots are the (1/3,1/3) adsorbate spots. *(c, d)* Side views showing the top five layers. The arrows show the buckling in the 4th substrate layer as the Ag atoms directly below the Pb are displaced vertically upwards.

A kinetic energy cut-off of 400 eV was applied for the plane waves, which was found to produce converged results for both Ag and Pb, for all the structures. For the exchange correlation potential the generalized gradient approximation (GGA) of the Perdew-Wang 91 (PW91) [38] was employed. The 10 x 8 x 1 Monkhorst- Pack mesh [39] was used for k-point sampling. The Ag surface was modelled using the supercell approach, where periodic boundary conditions are applied to the central supercell so that it is reproduced periodically throughout xy-space. The surface slab was modelled

with 6 layers of Ag atoms. A region of approximately 10 Å of vacuum was inserted in the z direction to prevent interactions occurring between periodic images. The bottommost layer of the surface slab was frozen during the geometry relaxation.

Adsorption energies of Pb atom are defined as:

$$E_{ads} = 1/N_{Pb} \times (E_{tot} - E_{clean} - N_{Pb} \times E_{Pb}) \tag{6.1}$$

where E_{tot} is total energy of relaxed Ag/Pb supercell, E_{clean} is the total energy of the relaxed clean Ag slab, N_{Pb} is the number of Pb atoms and E_{Pb} is the energy of one atom in the Pb bulk.

For substitutional alloy structures the adsorption energy is defined as:

$$E_{ads} = 1/N_{Pb} \times (E_{tot} - E_{clean} - N_{Pb} \times E_{Pb} + N_{Pb} \times E_{Ag\text{-}bulk}) \tag{6.2}$$

where, $E_{Ag\text{-}bulk}$ is the total energy of an Ag bulk atom.

An Ag lattice constant of 4.17 Å was used, which was obtained from bulk cell optimization using the same computational parameters. The six structural models used in the LEED I-V analysis were considered in the DFT analysis. The adsorption energies for each site for the models that showed convergence in the calculations are listed in Table 6.1. Of the overlayer geometries, the hcp hollow site is the most favourable but the substitutional and faulted surface alloy structures were by far the most stable with the unfaulted structure having an adsorption energy of -0.290 eV. The geometrical parameters for the relaxed substitutional surface alloy structure are listed in Table 6.2 and compare well with the LEED data.

Like the LEED analysis, DFT also favours the unfaulted substitutional surface alloy (-0.290 eV) although faulted alloy structure where all the top surface atoms (Pb and Ag)

have moved into hcp hollow sites is only marginally less favourable (-0.275 eV). One possible reason why our DFT calculations fail to clearly distinguish between the two structures is the use of the finite size of the slab (6 layers). Indeed, in an earlier DFT calculation by Woodruff and Robinson [7] for the Sb-Ag(111) system, they find that the stacking fault energy is sensitive to the slab thickness and suggest that these calculations are only realistic using much larger scale parallel computing systems beyond our means. It is also worth noting that even for the clean Ag(111) surface, they find that there is a negligible difference in energy between the surface faulted and unfaulted structures. Our calculation for the clean Ag(111) shows that the energy difference between the faulted and unfaulted Ag surface is only 20 meV, similar to what has previously been reported [7]. This implies that on Ag(111), a stacking fault surface structure could easily be facilitated. In fact for Sb on Ag(111), both faulted and unfaulted ($\sqrt{3}$x$\sqrt{3}$)$R30°$ structures have been found, as well as evidence for subsurface stacking faults, attributed to some subtle influence of subsurface Sb. For the Pb on Ag(111) case, we have only found the unfaulted $\left(\sqrt{3} \times \sqrt{3}\right)R30°$ structure, suggesting perhaps that Pb, with its larger atomic size compared to Sb, does not easily diffuse into the subsurface region. Another factor could be that there is a thermal activation barrier in moving all the surface atoms from the fcc hollow sites to the hcp hollow sites. In fact the Sb on Ag(111) structures were formed by dosing and annealing to elevated temperatures while in our case, sharp $\left(\sqrt{3} \times \sqrt{3}\right)R30°$ Pb on Ag(111) structure was readily formed by dosing at room temperature.

Dz [Å]	Adsorption Energy [eV]
0.00	-0.290
0.04	-0.273
0.07	-0.273
0.13	-0.277
0.15	-0.275

Table 6.3 - Changes in adsorption energy resulting from a change in height of top layer Ag atom.

DFT was also used to test the rumpled model suggested by Dalmas et al. Table 6.3 shows the adsorption energies starting with no rumpling and increasing to a maximum value of 0.15 Å between the two Ag atoms in the surface unit cell as measured perpendicular to the surface. In fact the total change in adsorption energy over this range was only 0.015 Å, coincidently the same as for the faulted structure. Although the unrumpled model is favored, given the previously stated limitations of this technique it cannot be absolutely stated which model is correct.

Both the LEED and DFT analysis show that in the stable substitutional surface alloy structure, there is a slight 'rumpling' of the surface due to the larger Pb atoms located about 0.4 Å above the surface plane of the Ag atoms. This amplitude of the 'rumpling' is smaller by about 1 Å than that predicted by a simple touching hard-spheres model based on bulk metallic radii (1.44 Å for Ag and 1.80 Å for Pb). This suggests a reduction in the effective radii similar to that found by Quinn *et al* [6] in their LEED

study of the substitutional surface alloy structure for the Pb-Ni(111) system. It has been suggested that the reduction in the effective radii may be attributed to the influence of valance electron charge smoothing and associated surface stress effects [5,6,13]. A similar effect is possibly the case for the Pb-Ag(111) structure in our study.

6.5 - Conclusions

There is very good agreement between the geometrical parameters extracted from LEED I-V and DFT analyses. LEED analysis shows that the Pb atoms are found to replace one top layer Ag atom in each unit cell, forming a substitutional unfaulted surface alloy. DFT calculations show that the stable $\left(\sqrt{3} \times \sqrt{3}\right)R30°$ structure is a surface alloy, but does not clearly distinguish between a faulted and unfaulted structure, possibly due to limitation of using a finite size slab. Because of the size difference between the Ag and Pb atoms (Pb is approximately 25% larger than Ag), the top layer is corrugated such that the Pb atoms reside about 0.4 Å above the Ag atoms. The amplitude of this 'rumpling' is smaller than what would be predicted on a simple touching hard-spheres model. The interlayer spacings, calculated with respect to the centres of mass of the Ag atoms, remain bulk like in both DFT and LEED analyses. Both LEED and DFT marginally favour the structure with no rumpling between the surface Ag atoms although given the small size of any possible distortion and the limitations of the techniques the rumpled structure cannot be ruled out.

6.6 - References

[1] Li, D.F., Xiao, H.Y., Zu, X.T. and Dong, H.N., 2007. First-principles study of the Ni(1 1 1)()R30°–Pb surface. *Physica B: Condensed Matter,* 392(1–2), pp. 217-220.

[2] Nie, J.L., Xiao, H.Y., Zu, X.T. and Gao, F., 2006. First principles calculations on Na and K-adsorbed diamond(1 0 0) surface. *Chemical Physics,* 326(2–3), pp. 308-314.

[3] Xiao, H.Y., Zu, X.T., He, X. and Gao, F., 2006. Sb adsorption on Cu(1 1 0), (1 0 0), and (1 1 1) surfaces. *Chemical Physics,* 325(2–3), pp. 519-524.

[4] Nascimento, V.B., Paniago, R., De Siervo, A., De Castilho, C.M.C., Landers, R., Soares, E.A. and De Carvalho, V.E., 2004. Structural study of the Ag(1 1 0)c(2 × 2)–Sb phase by low energy electron diffraction. *Surface Science,* 572(2–3), pp. 337-346.

[5] Quinn, P.D., Brown, D., Woodruff, D.P., Bailey, P. and Noakes, T.C.Q., 2002. Structural study of the adsorption of Sb on Ag(1 1 1) using medium energy ion scattering. *Surface Science,* 511(1–3), pp. 43-56.

[6] Quinn, P.D., Bittencourt, C. and Woodruff, D.P., 2002. Tensor LEED analysis of the Ni(111)($\sqrt{3}\times\sqrt{3}$)*R*30°-Pb surface. *Phys. Rev. B,* 65(23), pp. 233404

[7] Woodruff, J.P. and Robinson, J., 2000. Sb-induced surface stacking faults at Ag(111) and Cu(111) surfaces: density-functional theory results. *Journal of Physics: Condensed Matter,* 12(35), pp. 7699.

[8] Xu, M.C., Qian, H.J., Liu, F.Q., Krash, I., Lai, W.Y. and Wu, S.C., 2000. Pb Surfactant-Assisted Co Film Growth on Cu (111). *Chinese Physics Letters,* 17(8), pp. 595.

[9] Prieto, J.E., Rath, C., Müller, S., Hammer, L., Heinz, K. and Miranda, R., 2000. Surfactant action in heteroepitaxy: Growth of Co on (4×4)Pb/Cu(111) studied by LEED and STM. *Phys. Rev. B,* 62(8), pp. 5144.

[10] Gómez, L. and Ferrón, J., 2001. Surfactant effect in heteroepitaxial growth: The Pb-Co/Cu(111) case. *Phys. Rev. B,* 64(3), pp. 033409.

[11] Farias, D., Nino, M.A., De Miguel, J.J., Miranda, R., Morse, J. and Bozzolo, G., 2003. Growth of Co and Fe on Cu(1 1 1): experiment and BFS based calculations. *Applied Surface Science,* 219(1–2), pp. 80-87.

[12] Ayuela, A., Ogando, E. and Zabala, N., 2007. Quantum size effects of Pb overlayers at high coverages. *Applied Surface Science,* 254(1), pp. 29-31.

[13] Wei, C.M. and Chou, M.Y., 2002. Theory of quantum size effects in thin Pb(111) films. *Phys. Rev. B,* 66(23), pp. 233408.

[14] Ogando, E., Zabala, N., Chulkov, E.V. and Puska, M.J., 2005. Self-consistent study of electron confinement to metallic thin films on solid surfaces. *Phys. Rev. B,* 71(20), pp. 205401.

[15] Van Gastel, R., Kaminski, D., Vlieg, E. and Poelsema, B., 2009. Surface alloying and anomalous diffusion of Bi on Cu(1 1 1). *Surface Science,* 603(22), pp. 3292-3296.

[16] De Vries, S.A., Huisman, W.J., Goedtkindt, P., Zwanenburg, M.J., Bennett, S.L., Robinson, I.K. and Vlieg, E., 1998. Surface atomic structure of the (v3 × v3)R30°-Sb reconstructions of Ag (111) and Cu (111). *Surface Science,* 414(1-2), pp. 159-169.

[17] McLeod, I.M., Dhanak, V.R., Matilainen, A., Lahti, M., Pussi, K. and Zhang, K.H.L., 2010. Structure determination of the Bi–Ag(111) surface alloy using LEED I–V and DFT analyses. *Surface Science,* 604(17–18), pp. 1395-1399.

[18] Brown, D., Quinn, P.D., Woodruff, D.P., Bailey, P. and Noakes, T.C.Q., 2000. Medium-energy ion scattering structural study of the Ni(111)(v3×v3)R30°-Pb surface phase. *Physical Review B - Condensed Matter and Materials Physics,* 61(11), pp. 7706-7715.

[19] Xu, M.C., Qian, H.J., Liu, F.Q., Ibrahim, K., Lai, W.Y. and Gao, H.J., 2005. Surface alloying of Pb as a surfactant during epitaxial growth on Cu(1 1 1). *Surface Science,* 589(1–3), pp. 1-7.

[20] Wider, H., Gimple, V., Evenson, W., Schatz, G., Jaworski, J., Prokop, J. and Marszałek, M., 2003. Surface alloying of indium on Cu(111). *Journal of Physics: Condensed Matter,* 15(12), pp. 1909.

[21] Soares, E.A., Bittencourt, C., Lopes, E.L., De Carvalho, V.E. and Woodruff, D.P., 2004. LEED structure determination of the Ni(1 1 1)(√3×√3)R30°-Sn surface. *Surface Science,* 550(1–3), pp. 127-132.

[22] Mathias, S., Ruffing, A., Deicke, F., Wiesenmayer, M., Sakar, I., Bihlmayer, G., Chulkov, E.V., Koroteev, Y.M., Echenique, P.M., Bauer, M. and Aeschlimann, M., 2010. Quantum-Well-Induced Giant Spin-Orbit Splitting. *Phys. Rev. Lett.*, 104(6), pp. 066802.

[23] Dalmas, J., Oughaddou, H., Léandri, C., Gay, J.-., Le Lay, G., Tréglia, G., Aufray, B., Bunk, O. and Johnson, R.L., 2006. Formation of an unexpected ordered two-dimensional Ag2Pb surfacealloy on Ag(111): A SXRD and STM study. *Journal of Physics and Chemistry of Solids,* 67(1–3), pp. 601-604.

[24] Woodruff, D.P., Muñoz-Márquez, M.A. and Tanner, R.E., 2003. Structural studies at metallic surfaces and interfaces using MEIS. *Current Applied Physics,* 3(1), pp. 19-24.

[25] Pacilé, D., Ast, C.R., Papagno, M., Da Silva, C., Moreschini, L., Falub, M., Seitsonen, A.P. and Grioni, M.1., 2006. Electronic structure of an ordered Pb∕Ag(111) surface alloy: Theory and experiment. *Phys. Rev. B,* 73(24), pp. 245429.

[26] Dalmas, J., Oughaddou, H., Léandri, C., Gay, J., Le Lay, G., Tréglia, G., Aufray, B., Bunk, O. and Johnson, R.L., 2005. Ordered surface alloy formation of immiscible metals: The case of Pb deposited on Ag(111). *Phys. Rev. B,* 72(15), pp. 155424.

[27] Dalmas, J., Oughaddou, H., Le Lay, G., Aufray, B., Tréglia, G., Girardeaux, C., Bernardini, J., Fujii, J. and Panaccione, G., 2006. Photoelectron spectroscopy study of Pb/Ag(1 1 1) in the submonolayer range. *Surface Science,* 600(6), pp. 1227-1230.

[28] Ast, C.R., Pacilé, D., Moreschini, L., Falub, M.C., Papagno, M., Kern, K. and Grioni, M., 2008. Spin-orbit split two-dimensional electron gas with tunable Rashba and Fermi energy. *Phys. Rev. B,* 77(8), pp. 081407.

[29] Meier, F., Petrov, V., Guerrero, S., Mudry, C., Patthey, L., Osterwalder, J. and Hugo Dil, J., 2009. Unconventional Fermi surface spin textures in the $Bi_xPb_{1-x}/Ag(111)$ surface alloy. *Phys. Rev. B,* 79, pp. 241408(R).

[30] Van Hove, M.A., Moritz, W., Over, H., Rous, P.J., Wander, A., Barbieri, A., Materer, N., Starke, U. and Somorjai, G.A., 1993. Automated determination of complex surface structures by LEED. *Surface Science Reports,* 19(3-6), pp. 191-229.

[31] A. Barbieri and M. A. Van Hove, private communication.

[32] Pendry, J.B., 1980. Reliability factors for LEED calculations. *Journal of Physics C: Solid State Physics,* 13(5), pp. 937-944.

[33] Kresse, G. and Hafner, J., 1994. Norm-conserving and ultrasoft pseudopotentials for first-row and transition elements. *Journal of Physics: Condensed Matter,* 6(40), pp. 8245-8257.

[34] Kresse, G. and Furthmüller, J., 1996. Efficiency of ab-initio total energy calculations for metals and semiconductors using a plane-wave basis set. *Computational Materials Science,* 6(1), pp. 15-50.

[35] Kresse, G. and Furthmüller, J., 1996. Efficient iterative schemes for *ab initio* total-energy calculations using a plane-wave basis set. *Phys. Rev. B,* 54(16), pp. 11169.

[36] Kresse, G. and Joubert, D., 1999. From ultrasoft pseudopotentials to the projector augmented-wave method. *Physical Review B - Condensed Matter and Materials Physics,* 59(3), pp. 1758-1775.

[37] Blöchl, P.E., 1994. Projector augmented-wave method. *Physical Review B,* 50(24), pp. 17953-17979.

[38] Perdew, J.P. and Wang, Y., 1992. Accurate and simple analytic representation of the electron-gas correlation energy. *Physical Review B,* 45(23), pp. 13244-13249.

[39] Monkhorst, H.J. and Pack, J.D., 1976. Special points for Brillouin-zone integrations. *Phys. Rev. B,* 13(12), pp. 5188.

Chapter 7

Structure Determination of the $p(\sqrt{3} \times \sqrt{3})R30°$ Pb-Ag(111)

Surface Alloy Using MEIS

7.1 - Abstract

Using the technique of medium energy ion scattering (MEIS), we examine the growth of Pb on Ag(111) up to the coverage of 1/3 ML. As has been shown previously, the deposition of 1/3 of a monolayer of Pb on Ag(111) leads to the formation of $BiAg_2$ surface alloy with a long range ordered $\left(\sqrt{3} \times \sqrt{3}\right)R30°$ superstructure. We find strong correlation between our experimental data and previous studies. The Pb atom is found to replace one top layer Ag atom in each unit cell, forming a substitutional $BiAg_2$ surface alloy, with the Pb atoms residing approximately 0.6 Å above the Ag atoms due to their size difference.

7.2 - Introduction

Surface alloying of thin metallic films is a common phenomenon and has been studied for numerous systems using a variety of techniques [1-5]. Not only do we see alloying in systems where the elements are miscible in the bulk such as Cu-Au and Au-Ag [6,7], but we also see alloying in the first monolayer of normally immiscible metals such as Au on Ni(110) [8] or Ag on Pt(111) [9].

In instances where the radii of deposited atoms are larger than those of substrate atoms, the result is usually the formation of a substitutional surface alloy with a rumpled surface. However, typically the rumpling magnitude is less than that prediction from a simple hard-sphere model [10–14].

The technique of MEIS has successfully been used to study a range of similar systems and provided information on both atomic arrangement and surface rumpling.[15-18]

Interest in the adsorption of Pb on many surfaces arises, at least in part, from its role as a surfactant to promote 2D layer by layer growth as has been reported in numerous recent studies [19-22]. At higher coverage, the growth of Pb films can lead to the formation of nano-sized structures due to quantum confinement and finite size effects which in turn can lead to some novel effects [23-25]. Furthermore, there has been recent interest in these materials for their electronic properties such as the Rashba effect and the fact that Rashba energies can be tuned with small changes in surface composition and structure [26-27].

Given the interest in this material and its uses, a detailed structural knowledge of the structure is of great importance. There have been a number of recent studies into this system although the outcomes are not so clear cut. There is general consensus that at a

coverage of around 1/3 ML there is a formation of a $\sqrt{3}\times3\sqrt{}$ $R30°$ superstructure with Pb atoms embedded into the silver top surface layer to form an ordered Ag_2Pb surface alloy. A recent STM and SXRD study [28] suggested there was a rumpling, not only of the embedded Pb atom but also between the two Ag atoms of the surface unit cell. They suggested this was a Pierls type distortion although it might just have been an effect of the STM measurement process. It is an unusual result not yet reported in any similar systems and so further examination of the structure using LEED I-V and DFT was undertaken [29]. Although the results did not favour a rumpling of Ag atoms, the fact that any such distortion was likely to be so small meant that it could not categorically be ruled out.

We present here a detailed structural study of this surface structure using MEIS. The results show that a Pb atom is found to replace one top layer Ag atom in each unit cell, forming a substitutional unfaulted $PbAg_2$ surface alloy, with the larger Pb atoms residing about 0.4 Å above the Ag atoms due to the size difference. The results also indicate that the Dalmas model with surface Ag rumpling is slightly less favourable than the model where the Ag atoms remain in their normal positions relative to one another.

7.3 - Experiment

The experiments were all performed at the MEIS facility based at Daresbury laboratory, Cheshire, UK. The facility has been described in detail elsewhere [30]. Sample preparation and data collection were carried out at room temperature in ultra high vacuum conditions (UHV).

The Ag(111) surface was cleaned with cycles of Ar^+ sputtering and annealing to 700 K. LEED was used to check the cleanliness and quality of the surface and to calibrate the deposition rate . Pb was deposited onto the clean Ag(111) surface from a well degassed Omicron K-cell until LEED showed a $(\sqrt{3}x\sqrt{3})R30°$ pattern. During deposition the Ag sample was kept at room temperature and the vacuum pressure did not exceed 3 x 10^{-10} mBar. The Pb was deposited at a constant rate of 0.1 ML/min.

The MIES study was done using H^+ ions with a beam energy of 100 keV. Data was taken at incident angles [110], [211] and [123].

7.4 – Analysis and Discussion

Data was collected for three different incident angles. The ranges of scattering angles for each incident angle are shown in Table 7.1. The experiment was performed twice and each date set was initially analysed separately and compared with a variety of theoretical models.

Six different structural models were considered. These were four high symmetry adsorption geometries, namely the top (1) and hollows (2 and 3, for fcc and hcp hollows, respectively), as well as the bridge site (4), as shown in Figure 7.1.

Incident Angle	Scattering Angles
[110]	60.25^o - 123.25^o
[211]	79.75^o - 119.75^o
[123]	97.25^o - 122.25^o

Table 7.1 – Range of angles over which data was collected for each incident angle.

As well as these adsorption sites, two high symmetry substitutional alloy structures were also considered. The first of these was formed by placing one Pb atom per unit cell in a substitutional position over an essentially unperturbed Ag(111) surface layer to give the $(\sqrt{3} \times \sqrt{3})R30°$ superstructure. The second was a similar surface alloy but with all the surface atoms displaced to the 'hcp' hollow sites, the so-called faulted surface alloy structure [5].

In order to produce 'blocking curves', regions of the data tiles were selected and their intensities were extracted. A sample of raw data taken from [110] scan is shown in Figure 7.2 along with the areas used to provide the bulk and surface data. Bulk data was used to calibrate scan angles against known blocking angles for Ag(111).
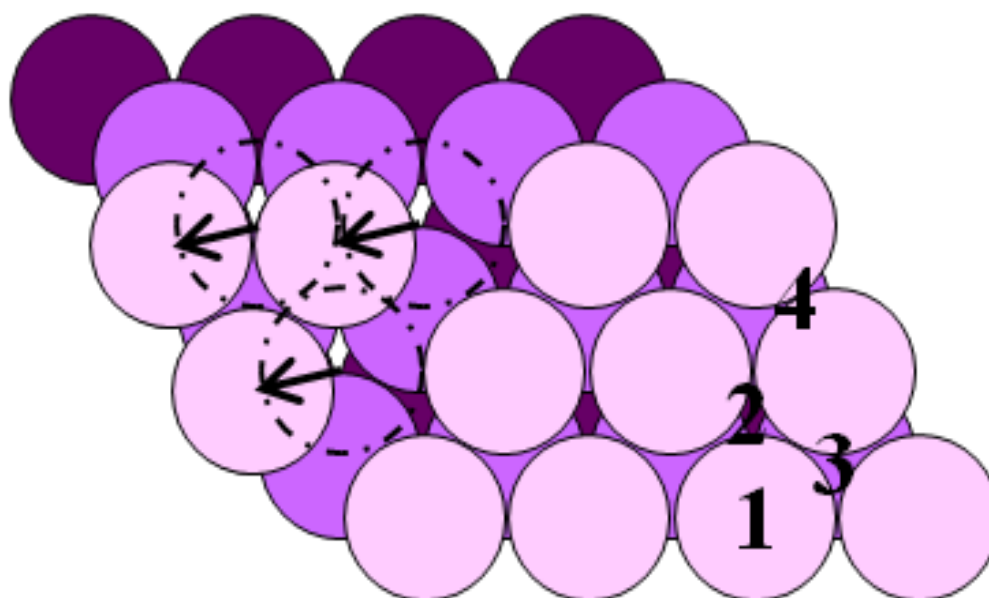

Figure 7.1 - Adsorption sites: A = top, B =HCP hollow, C = FCC hollow and D = bridge. Top three layers of the substrate are shown. Arrow show atoms shifted into the HCP stacking fault position.
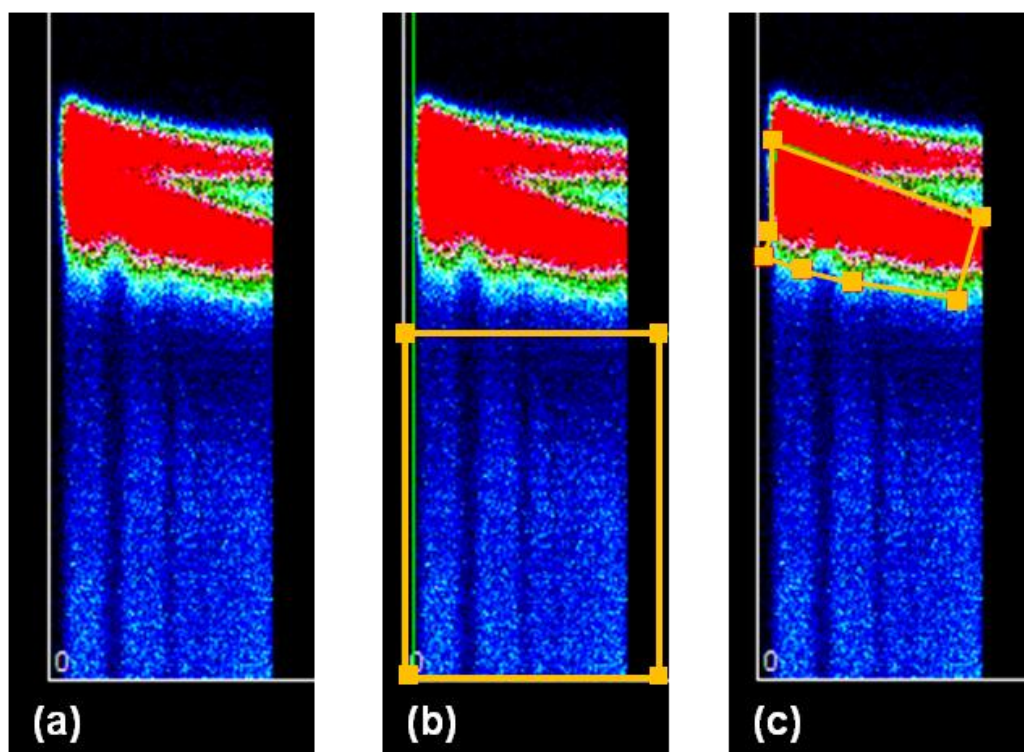
Figure 7.2 – (a) A sample of raw data taken from [110] scan, (b) Selected bulk region outlined in yellow, (c) Selected surface region outlined in yellow

The simulations were produced using the programme VEGAS which has been developed specifically to simulate MEIS data [31]. The theoretical curves were done with 0.5° angular step size and the extracted intensities from the experimental data were binned into corresponding step sizes. Table 7.2 shows the R values for each of the six structures for the first [110] data set.

After the R values were calculated the data from the first and second runs were compared with one another and any anomalous data points were removed. This was done using χ^2 fit where any values of χ^2 greater than 3 were considered to be unreliable and removed in order to smooth the data. The two data sets were then averaged before the final R values were obtained. Both before and after the anomalies were removed the surface alloy structure was clearly favoured.

Atomic Arrangement	R Values, data set 1 (As Extracted)	R Values, data set 1 (Anomalies removed)
Top (1)	10.066	12.097
Hollow (2)	10.109	12.174
Hollow (3)	3.729	3.975
Bridge (4)	5.258	4.630
Surface Alloy	**2.697**	**1.239**
Faulted Surface Alloy	17.479	22.597

Table 7.2 - The R values for each of the six structures for the first [1̲1̲0] data set, as extracted and with anomalous values removed.

Due to the larger size of the Pb atoms relative to the Ag, a surface rumpling was expected for both of the surface alloy structures. The initial value of this rumpling was set at 0.4 Å based on previously published results. [29]

For the [1̲2̲3] data set we see a similar story with the surface alloy structure clearly favoured. The results from the average of the two data sets are shown below in Table 7.3. The case for the data from the [211] incident angle was not so clear cut. It can be seen in Table 7.3 that the lowest R factor is that of the top site, labelled '1' in Figure 7.1, however, its R factor of 2.694 is only marginally better than that of the surface alloy structure at 2.764. In cases where R factors are within 10% of one another for MEIS simulations it is not possible to categorically say which structure is favoured. In

Atomic Arrangement	R Factor For Averaged Data [123]	R Factor For Averaged Data [211]
Top (1)	2.997	**2.694**
Hollow (2)	3.445	4.911
Hollow (3)	2.977	6.319
Bridge (4)	3.018	4.626
Surface Alloy	**2.370**	**2.764**
Faulted Surface Alloy	3.704	9.380

Table 7.3 - The R values for each of the six structures for the [123] and [211] averaged data sets.

fact, the difference between these two results is only in the order of about 3%. If we look at the results graphically, Figure 7.3, we can see there is little to separate them. It is worth noting, however, that the relative intensities are not as important as the actual positions of the blocking dips although this is not taken into account in the calculation of the R factor. Based on the results from the previous two incident angles it is reasonable to rule out the possibility of the top site being the real structure.

Next we varied the interlayer spacings for the top four layers, one layer at a time. In each case, a 2% change in interlayer spacing with respect to the bulk values resulted in a minimum of 8% worsening in the R factors leading us to conclude that interlayer spacing, in fact, remains bulk like to within 1% of its value.

We now turn our attention to the claims of Dalmas et al, as to there being a rumpling of the two Ag atoms in the surface layer unit cell. It has been previously noted that MEIS is not particularly precise when defining surface rumpling [5]. The reason suggested for this is that a small value of rumpling is similar to the effect of enhanced vibration amplitude of surface atoms. MEIS is unable to distinguish between static disorder and displacements. In order to improve the accuracy of our results when measuring this supposed rumpling we will take an average of the six data sets (two data sets for each of the three incident geometries). Rather than take a straight average of the results we have chosen to give the [110] incident data a 50% weighting as this orientation is by far the most surface sensitive of the three. The actual value assigned to the weighting is somewhat arbitrary.
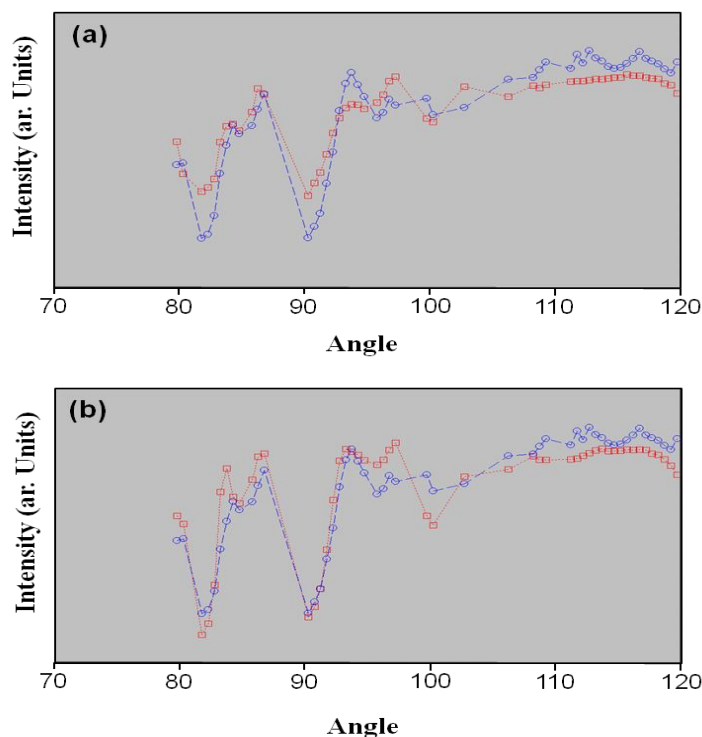

Figure 7.3 – Comparison of experimental data for the [211] incident scan with (a) surface alloy model, (b) top site model.

Initially simulations were performed with no rumpling between the two Ag atoms of the surface unit cell and the rumpling height of the Pb atom was varied. Once the optimum Pb height was determined the value was set in the model and a rumpling in one of the two Ag atoms was simulated. The results of both are shown in Table 7.4.

Displacement of atom, Å	Averaged R Factor	
	Pb atom	Ag Atom
0	2.167	2.014
0.05	2.040	2.040
0.10	2.057	2.006
0.15	2.142	2.031
0.20	2.125	2.091
0.25	2.006	2.065
0.30	2.040	2.082
0.35	2.048	2.048
0.40	2.014	2.167
0.45	2.014	2.116
0.50	2.006	2.057
0.55	2.133	2.142
0.60	2.091	2.125
0.65	2.065	2.082
0.70	2.082	2.040

Table 7.4 – Averaged R values for different rumpling heights of both the Pb atom and one Ag atom of the surface unit cell.

Initially simulations were performed with no rumpling between the two Ag atoms of the surface unit cell and the rumpling height of the Pb atom was varied. Once the optimum Pb height was determined the value was set in the model and a rumpling in one of the two Ag atoms was simulated. The results of both are shown in Table 7.4.

The data in Table 7.5 is plotted in Figure 7.4. Even after averaging six data sets it appears the trend is heavily masked in the general 'noise'. Although not shown here, simulations were also done for a situation where the Ag atom dipped into the surface rather than protruded above it with similar scattered results.
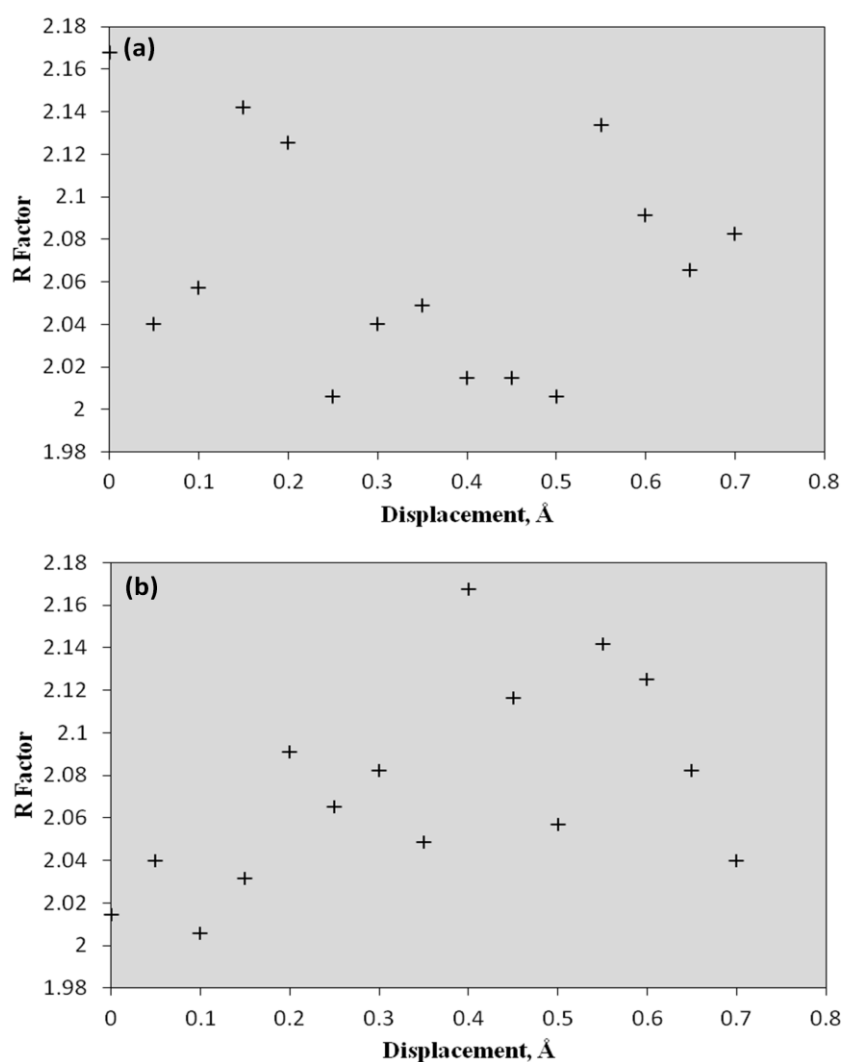

Figure 7.4 – R values for different rumpling heights of (a) Pb atoms and (b) Ag atoms of the surface layer .

For the Pb rumpling, a second order polynomial was fitted to the data in such a way as to minimise the χ^2 value. Based on this fit we obtained a rumpling value of 3.6 Å, although the error on this value could well be as much as $\pm$ 50%.

As for the rumpling of the Ag atoms, the trend appears to be favouring no rumpling between the atoms but with any actual value of rumpling likely to be so small it is not possible to say any more based solely on these results.

7.5 - Conclusion

There is very good agreement between the geometrical parameters extracted from MEIS data and previous studies. MEIS analysis shows that the Pb atoms are found to replace one top layer Ag atom in each unit cell, forming a substitutional unfaulted surface alloy. Because of the size difference between the Ag and Pb atoms (Pb is approximately 25% larger than Ag), the top layer is corrugated such that the Pb atoms reside about 0.4 Å above the Ag atoms. The amplitude of this 'rumpling' is smaller than what would be predicted on a simple touching hard-spheres model. The interlayer spacings, calculated with respect to the centres of mass of the Ag atoms, remain bulk like. The results marginally favour the structure with no rumpling between the surface Ag atoms although given the small size of any possible distortion and the limitations of the techniques the rumpled structure cannot be ruled out.

7.6 – References

[1] Li, D.F., Xiao, H.Y., Zu, X.T. and Dong, H.N., 2007. First-principles study of the Ni(1 1 1)()R30°–Pb surface. *Physica B: Condensed Matter*, 392(1–2), pp. 217-220.

[2] Nie, J.L., Xiao, H.Y., Zu, X.T. and Gao, F., 2006. First principles calculations on Na and K-adsorbed diamond(1 0 0) surface. *Chemical Physics*, 326(2–3), pp. 308-314.

[3] Xiao, H.Y., Zu, X.T., He, X. and Gao, F., 2006. Sb adsorption on Cu(1 1 0), (1 0 0), and (1 1 1) surfaces. *Chemical Physics*, 325(2–3), pp. 519-524.

[4] Nascimento, V.B., Paniago, R., De Siervo, A., De Castilho, C.M.C., Landers, R., Soares, E.A. and De Carvalho, V.E., 2004. Structural study of the Ag(1 1 0)c(2 × 2)–Sb phase by low energy electron diffraction. *Surface Science*, 572(2–3), pp. 337-346.

[5] Quinn, P.D., Brown, D., Woodruff, D.P., Bailey, P. and Noakes, T.C.Q., 2002. Structural study of the adsorption of Sb on Ag(1 1 1) using medium energy ion scattering. *Surface Science*, 511(1–3), pp. 43-56.;

[6] Chambliss, D.D. and Chiang, S., 1992. Surface alloy formation studied by scanning tunneling microscopy: Cu(100) + Au−c(2 × 2).

[7] Rousset, S., Chiang, S., Fowler, D.E. and Chambliss, D.D., 1992. Intermixing and three-dimensional islands in the epitaxial growth of Au on Ag(110). *Phys. Rev. Lett.*, 69(3200).

[8] Pleth Nielsen, L., Besenbacher, F., Stensgaard, I. and Laegsgaard, E., 1993. Initial growth of Au on Ni(110): Surface alloying of immiscible metals. *Phys. Rev. Lett.*, 71(5), pp. 754.

[9] Röder, H., Schuster, R., Brune, H. and Kern, K., 1993. Monolayer-confined mixing at the Ag-Pt(111) interface. *Phys. Rev. Lett.*, 71, pp. 2086.

[10] Brown, D., Noakes, T.C.Q., Woodruff, D.P., Bailey, P. and Goaziou, Y.L., 1999. Structure determination of the $Cu(100)c(2 \times 2)-Mn$ and $Cu(100)c(2 \times 2)-Au$ surface alloy phases by medium-energy ion scattering. Journal *of Physics: Condensed Matter*, 11, pp. 1889.

[11] Caputi, L.S., Marsico, R., Scalese, S., Cupolillo, A., Chiarello, G., Colavita, E. and Papagno, L., 2000. Structural study of Ni(100)-c(2×2)-Sn, by electron-energy-loss holography. *Surface Science*, 444(1–3), pp. 61-65.

[12] Quinn, P.D., BIttencourt, C., Brown, D., Woodruff, D.P., Noakes, T.C.Q. and Bailey, P., 2002. Tensor low energy electron diffraction and medium energy ion scattering determination of the Ni(110)c(2×2)-Sn surface structure. *Journal of Physics: Condensed Matter*, 14, pp. 665.

[13] Overbury, S.H. and Ku, Y., 1992. Formation of stable, two-dimensional alloy-surface phases: Sn on Cu(111), Ni(111), and Pt(111). *Phys. Rev. B*, 46, pp. 7868.

[14] Li, Y.D., Jiang, L.Q. and Koel, B.E., 1994. Surface alloy formation and the structure of c(2×2)-Sn/Ni(100) determined by low-energy alkali-ion scattering. *Phys. Rev. B*, 49, pp. 2813.

[15] Soares, E.A., Leatherman, G.S., Diehl, R.D. and Van Hove, M.A., 2000. Low-energy electron diffraction study of the thermal expansion of Ag(111). *Surface Science*, 468(1–3), pp. 129-136.

[16] Bailey, P., Noakes, T.C.Q. and Woodruff, D.P., 1999. A medium energy ion scattering study of the structure of Sb overlayers on Cu(111). *Surface Science*, 426(3), pp. 358-372.

[17] Quinn, P.D., Brown, D., Woodruff, D.P., Bailey, P. and Noakes, T.C.Q., 2002. Structural study of the adsorption of Sb on Ag(1 1 1) using medium energy ion scattering. *Surface Science*, 511(1–3), pp. 43-56.

[18] Brown, D., Quinn, P.D., Woodruff, D.P., Bailey, P. and Noakes, T.C.Q., 2000. Medium-energy ion scattering structural study of the Ni(111)(v3×v3)R30°-Pb surface phase. *Physical Review B - Condensed Matter and Materials Physics,* 61(11), pp. 7706-7715.

[19] Xu, M.C., Qian, H.J., Liu, F.Q., Krash, I., Lai, W.Y. and Wu, S.C., 2000. Pb Surfactant-Assisted Co Film Growth on Cu (111). *Chinese Physics Letters,* 17(8), pp. 595.

[20] Prieto, J.E., Rath, C., Müller, S., Hammer, L., Heinz, K. and Miranda, R., 2000. Surfactant action in heteroepitaxy: Growth of Co on (4×4)Pb/Cu(111) studied by LEED and STM. *Phys. Rev. B*, 62(8), pp. 5144.

[21] Gomez, L. and Ferron, J., 2001. Surfactant effect in heteroepitaxial growth: The Pb-Co/Cu(111) case. *Phys. Rev. B*, 64(3), pp. 033409.

[22] Farias, D., Nino, M.A., De Miguel, J.J., Miranda, R., Morse, J. and Bozzolo, G., 2003. Growth of Co and Fe on Cu(1 1 1): experiment and BFS based calculations. *Applied Surface Science*, 219(1–2), pp. 80-87.

[23] Ayuela, A., Ogando, E. and Zabala, N., 2007. Quantum size effects of Pb overlayers at high coverages. *Applied Surface Science*, 254(1), pp. 29-31.

[24] Wei, C.M. and Chou, M.Y., 2002. Theory of quantum size effects in thin Pb(111) films. *Phys. Rev. B*, 66(23), pp. 233408.

[25] Ogando, E., Zabala, N., Chulkov, E.V. and Puska, M.J., 2005. Self-consistent study of electron confinement to metallic thin films on solid surfaces. *Phys. Rev. B*, 71(20), pp. 205401.

[26] Ast, C.R., Pacilé, D., Moreschini, L., Falub, M.C., Papagno, M., Kern, K. and Grioni, M., 2008. Spin-orbit split two-dimensional electron gas with tunable Rashba and Fermi energy. *Phys. Rev. B*, 77(8), pp. 081407.

[27] Meier, F., Petrov, V., Guerrero, S., Mudry, C., Patthey, L., Osterwalder, J. and Hugo Dil, J., 2009. Unconventional Fermi surface spin textures in the BixPb1−x/Ag(111) surface alloy. *Phys. Rev. B*, 79, pp. 241408(R).

[28] Dalmas, J., Oughaddou, H., Léandri, C., Gay, J., Le Lay, G., Tréglia, G., Aufray, B., Bunk, O. and Johnson, R.L., 2005. Ordered surface alloy formation of immiscible metals: The case of Pb deposited on Ag(111). *Phys. Rev. B*, 72(15), pp. 155424.

[29] McLeod, I.M., Dhanak, V.R., Lahti, M., Matilainen, A., Pussi, K. and Zhang, K.H.L., 2011. LEED I–V and DFT structure determination of the Pb−Ag(111) surface alloy. *Journal of Physics: Condensed Matter*, 23, pp. 265006.

[30] Bailey, P., Noakes, T.C.Q. and Woodruff, D.P., 1999. A medium energy ion scattering study of the structure of Sb overlayers on Cu(111). *Surface Science*, 426(3), pp. 358-372.

[31] Woodruff, D.P., 2007. MEIS investigations of surface structure. *Nuclear Instruments and Methods in Physics Research Section B: Beam Interactions with Materials and Atoms*, 256(1), pp. 293-299.

Chapter 8

Templated three-dimensional growth of quasicrystalline lead

8.1 - Abstract

Quasicrystals, materials with aperiodic long-range order, have been found in intermetallics, soft materials such as colloids and supermolecules, and also in two-dimensional monolayer films. Here we present the first example of three-dimensional growth of a single-element quasicrystalline film. Using a hitherto unexplored template, the icosahedral Ag-In-Yb quasicrystal, and various experimental techniques combined with theoretical calculations of adsorption energies, we find that lead atoms deposited on the surface occupy the positions of atoms in the rhombic triacontahedral cluster, the building block of the substrate, and thus grow in layers with different heights and adsorption energies. We show that the adlayer– adlayer interaction is crucial for stabilizing this epitaxial quasicrystalline structure. The finding opens an avenue for further investigation of the impact of the aperiodic atomic order over periodic order on the physical and chemical properties of materials.

8.2 - Introduction

Since their discovery [1], quasicrystalline phases have been found in >100 intermetallic compounds, liquid crystals [2], polymers [3], colloids [4] and perovskite thin films [5], and are recognized as universal phases of matter. A very important breakthrough was the discovery of stable intermetallic phases [6], which enabled detailed experimental studies, including the determination of accurate atomic structures of quasicrystals and investigation of quasicrystalline surfaces and overlayers (reference [7] and references therein).

A universal pseudogap in the electronic density of states near the Fermi energy is characteristic of quasicrystals and related compounds [8], and semiconducting electronic transport has been reported for many systems [9]. This unique electronic structure in turn affects physical and chemical properties of quasicrystal surfaces, resulting in unexpected surface properties such as non-stickiness and low friction [10, 11].

Because of their unusual structure and rotational symmetry, quasicrystals provide unique templates for the exploration of new epitaxial phenomena. Several interesting results have been observed in adsorption on surfaces of the Al-based quasicrystals (reference [7] and references therein), which include pseudomorphic monolayers of Bi [12,13], Sb [12], Pb [14,15] and Sn [16], quasiperiodically modulated multilayer structures of Cu [17,18] and Co [19], fivefold twinned islands with magic heights influenced by quantum size effects [20] and a non-fcc structure of Ag [21].

In this study, we demonstrate the formation of a novel form of quasicrystalline structure, which is formed by a single element grown on a template. Using the fivefold

surface of the icosahedral (i-) Ag-In-Yb quasicrystal as a substrate, we have succeeded in growing a quasicrystalline film of a single element where the adatoms occupy multiple sites at different levels, which correspond to the completion of the rhombic triacontahedral (RTH) bulk clusters truncated by the surface. This finding adds to previous observations of modulated multilayers and quasicrystal-line monolayers observed on the common Al-based quasicrystals. Combining the experimental results using scanning tunnelling microscopy (STM), low-energy electron diffraction (LEED) and x-ray photoemission spectroscopy (XPS) with density functional theory (DFT) calculations for adsorption energies, we have determined the structure of the Pb film. The Pb atoms occupy the position of atoms in the RTH cluster, the building block of the Ag-In-Yb quasicrystal, and thus mirror the atomic positions in the truncated half cluster of the bulk. As a result of this, the structure of the film can be characterized by layers of atoms with different heights above the substrate. The structure of each layer can be deduced from the substrate structure. As such, each layer is geometrically distinct from the layer below, leading to the film as a whole displaying quasicrystalline order in three dimensions. Thus, this system constitutes the simplest possible quasicrystal.

8.3 -Experimental Details

8.3.1 - Bulk structure of *i* -Ag-In-Yb

The *i*-Ag-In-Yb quasicrystal is isostructural to the unique binary *i*-Cd-Yb phase [22]. The basic building block of this system is the RTH cluster, which consists of five successive atomic shells [23]. The atomic shells are a Cd rhombic triacontahedron

(outermost), a Cd icosidodecahedron, a Yb icosahedron, a Cd dodecahedron and a Cd tetrahedron (innermost). The RTH clusters contain 93.8% of the total number of atoms in the crystal. The remaining atoms are contained in acute and obtuse rhombohedra, which provide linkages or 'glue' between the RTH units.

8.3.2 - Thin Film Preparation

Pb was deposited on the fivefold surface of i-$Ag_{42}In_{42}Yb_{16}$ at temperature of 300 K using an Omicron electron-beam evaporator with a constant flux. Before the deposition, the substrate was prepared and characterized as described in reference [24]. The pressure during deposition remained almost the same as the base pressure. The Pb film was characterized by STM, LEED and XPS. STM measurements were performed at room temperature in constant current mode. XPS and STM experiments were performed in two chambers with different flux and geometry for Pb deposition.

8.3.3 - DFT Calculations

Calculations are done with projector-augmented-wave potentials [32] and the generalized gradient approximation [33]. To handle the aperiodic fivefold surface in the periodic calculation, the surface is approximated by a disc-shaped cluster with 4 Å thickness and 30 Å diameter. The atomic positions are extracted from a model for the isostructural Cd-Yb quasicrystal [23]. Chemical ordering of Ag and In is assumed according to the occupation probability deduced from an X-ray diffraction experiment for the cubic approximant as described in reference [26]. The topmost layer is chosen to intersect the RTH cluster centre and is flat. With the chemical ordering assumed here, this flat layer consists of only In and Yb. This is consistent with the relaxation trend that Ag is more likely to intrude into the bulk [34]. Moreover, the innermost shell of

the RTH cluster is a tetrahedron of In in the bulk, but the structure near the surface has not been determined yet. We assume here that there is a single In atom at the RTH cluster centre for the topmost layer.

A convergence test for adsorption energies was performed by comparison with results for larger model-clusters with 30 Å diameter and 6 Å thickness, and 50 Å diameter and 4 Å thickness. In most cases, the maximum difference is less than 0.1 eV, and it is about 0.2 eV at worst. Relaxations of atomic positions and spin-polarization effects are not included in all calculations.

8.4 - Results and Discussion

Substrate structure. The i-Ag-In-Yb quasicrystal is isostructural to the unique binary i-Cd-Yb phase [22], where Cd is replaced by Ag and In. The atomic structure of this system has been solved without ambiguity [23]. The basic building block of this system is the RTH cluster, which consists of five successive atomic shells [23].

The substrate surface can be prepared with wide flat terraces (Figure 8.1a). The terraces are formed preferentially at bulk planes, which are dense, Yb rich and intersect the cluster centres [24]. STM images taken at negative sample bias voltage are characterized by protrusions located at the vertices of a Penrose P1 tiling with an edge length of about 24±1 Å (reference [24]). The P1 tiling consists of four different tiles: pentagons, stars, rhombi and boats [25]. The pentagons are of two different orientations, rotated at 36° to each other. These are marked in Figure 8.1a.
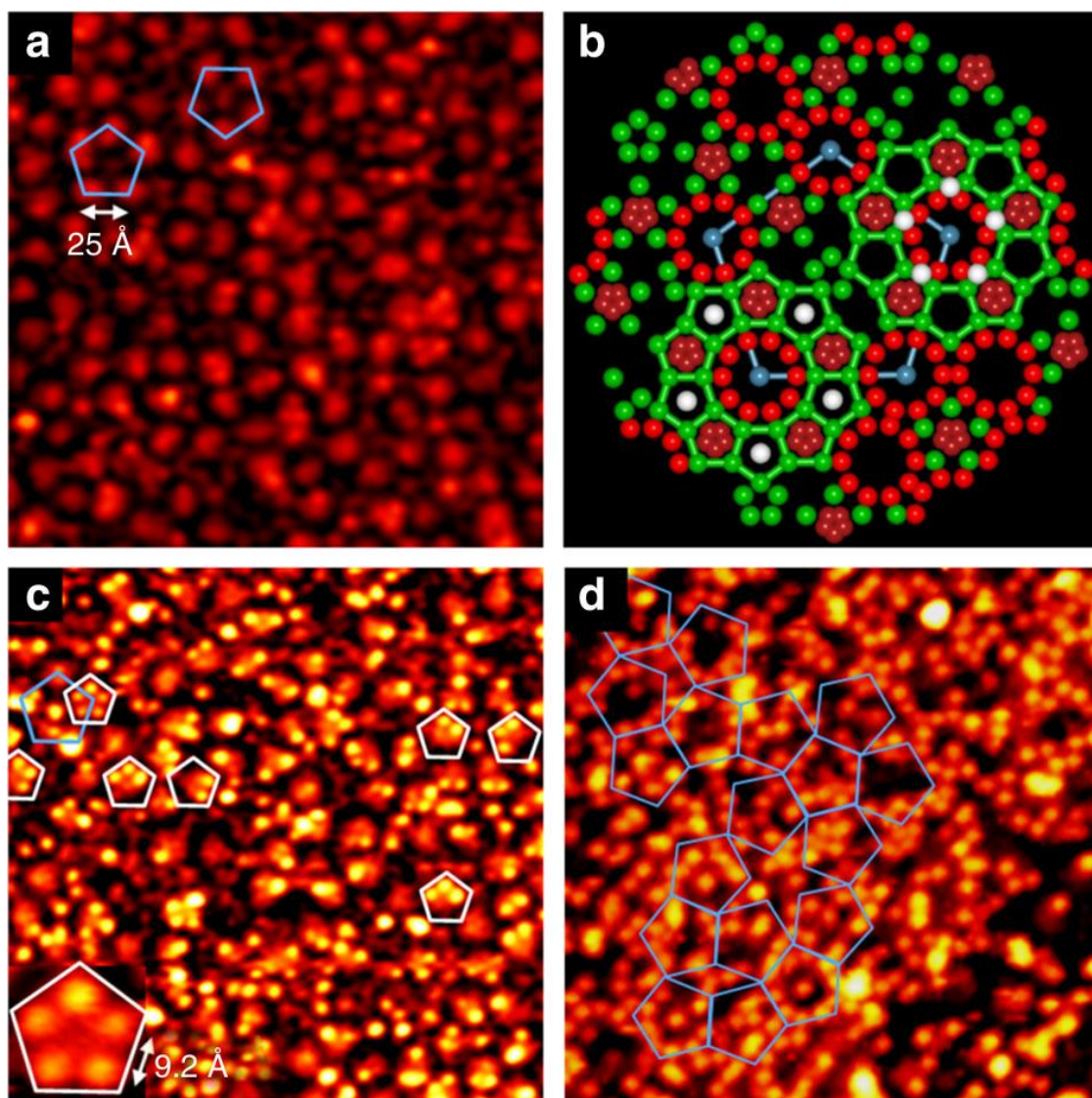
Figure 8.1 - Initial Pb adsorption sites. (a,c,d) STM images (300 Å _ 300 Å) of a terrace of the fivefold i-Ag-In-Yb surface (a, clean surface; c, after deposition of Pb for 5 min; d, 15 min). The substrate pentagonal features and Pb pentagons are marked by blue and white pentagons, respectively, in a and c. A patch of a Penrose P1 tiling is overlaid in d. (b) Atomic structure of a bulk-terminated surface of i-Ag-In-Yb deduced from the structure of i-Cd-Yb. The vertices of pentagonal unit are uniquely decorated by Ag/In rings (red) surrounded by Yb pentagons (green). Dark red spheres represent Ag/In atoms at 0.4 Å below the top layer and blue spheres the centre of RTH units. White spheres forming small and large pentagons mark adsorption sites for Pb atoms in the first and second layers.

The protrusions observed in STM are related to the cross-section of the Cd icosidodecahedral shell of the RTH cluster. To explain this, we present in Figure 8.1b the atomic structure of surface-terminating bulk layers deduced from the ideal bulk model of i-Cd-Yb [23]. The icosidodecahedral shells of the RTH cluster form decagons at the surface (red rings in the figure), which are centred at the vertices of a P1 tiling of 25.3 Å edge length. According to the structure of the Ag-In-Yb approximant [26], the icosidodecahedral shell is mostly occupied by In (see below for further discussion of the occupation probability of Ag and In). We will, therefore, refer to the decagon as the In decagon. The In decagon at each vertex of the P1 tiling is surrounded by ten Yb pentagons, which belong to different RTH units or to the glue atoms between the RTH clusters. In STM, large protrusions are observed at the positions of In decagons at negative bias, whereas the Yb pentagons are resolved at positive bias [24].

Figure 8.1c, shows an STM image after 5 min deposition of Pb, where the area covered by Pb atoms is about 10–20% of the total substrate area (about 2×10^{-3} atoms per Å^{2}). At this low coverage, both the substrate structure and the deposited Pb atoms are resolved, and thus it is possible to identify the adsorption sites. The brighter dot-like motifs in the image correspond to individual Pb atoms, which are at a height of ~1.1±0.1 Å above the substrate. The Pb atoms form pentagons of 9.2±0.5 Å edge length (marked in Figure 8.1c). At this coverage, most pentagons are incomplete, and isolated Pb atoms are also observed. At increasing coverages, complete pentagons evolve.

The Pb pentagons are observed on the top of the protrusions. They exhibit only one orientation, which is identical to one of the pentagonal units of the substrate. From the location with respect to the substrate, and the size and orientation of the Pb pentagons,

an adsorption site is identified between the In and Yb rings. These sites are marked by five spheres forming a small white pentagon in Figure 8.1b.

On further deposition (15 min), a network of Pb pentagons is obtained as shown in Figure 8.1d. The structure of the network can be mapped with a P1 tiling of edge length of ~25 Å, with the vertices located at the centres of the Pb pentagons. Such a tiling is expected from the substrate structure if Pb atoms occupy the selected adsorption sites mentioned above. The density of adatoms at this coverage deduced from STM images of different terraces varies from 4×10^{-3} to 7×10^{-3} atoms per Å^2, which is less than the atomic density of the topmost substrate layer (3×10^{-2} to 5×10^{-2} atoms per Å^2), but in the same range as the density of the possible adsorption sites calculated from the substrate structure, suggesting that this coverage is close to saturation of these sites.

Once the adsorption sites between the In and Yb rings are saturated, Pb atoms adsorb on top of the network of the Pb pentagons (Figure 8.2a). These Pb atoms, which appear as red in the colour map, are at a height of 3.1±0.1 Å above the substrate and, thus, can be considered to be part of a second Pb layer above the network of Pb pentagons, which form the first layer. The Pb atoms in the second layer also form pentagons. These pentagons have an edge length of 13.8±1.5 Å, which is larger than the pentagons in the first layer by a factor of τ =1.618… an irrational number characteristic of quasicrystalline order. They exhibit an identical orientation, rotated by 36° with respect to the pentagons in the first layer. This can be seen in Figure 8.2a, where pentagons of both layers are resolved. Both the size and orientation of the Pb pentagons suggest that Pb atoms in the second layer are adsorbed at the centre of alternating Yb pentagons surrounding the RTH cluster centres. These sites are marked by white spheres forming a large pentagon in Figure 8.1b.
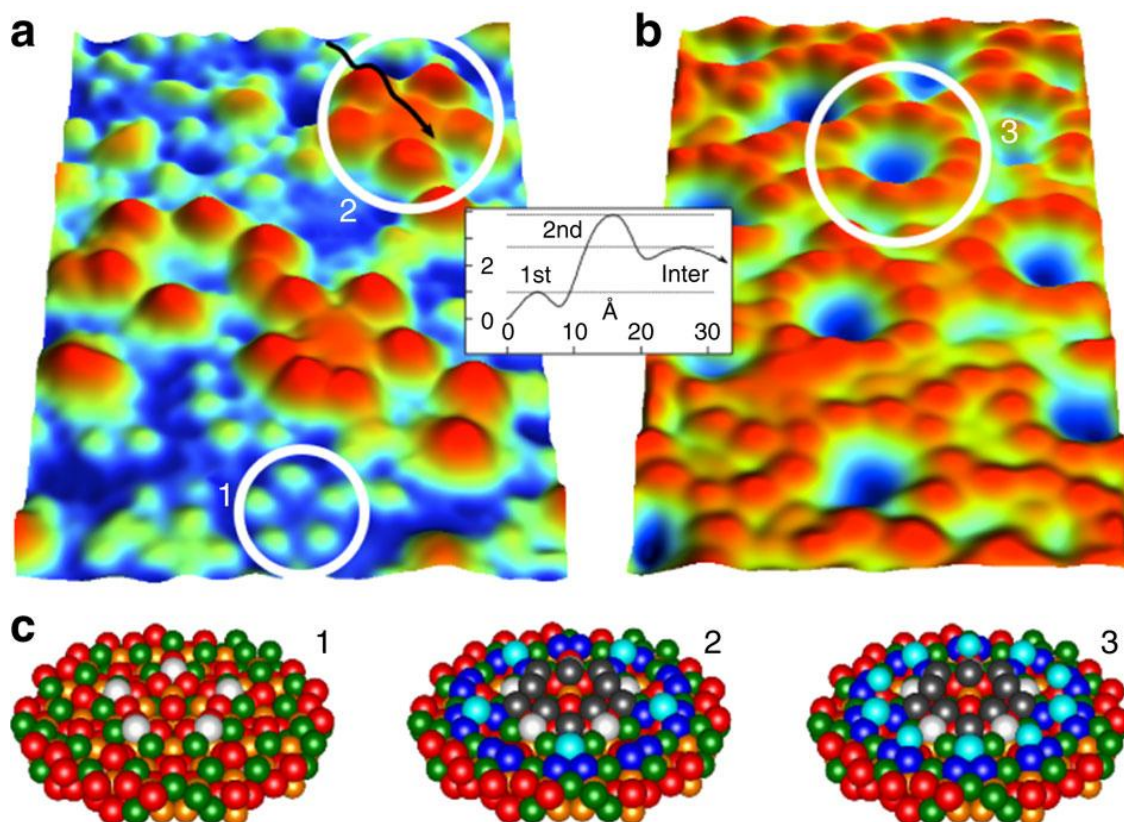
Figure 8.2 - Evolution of successive Pb layers. STM images (180 Å × 145 Å) of a terrace of the fivefold i-Ag-In-Yb surface after deposition of Pb for 30 min (a) and 90 min (b). The inset is the height profile along a line indicated by an arrow, demonstrating the height of the first, second and intermediate layers. (c) Model structures corresponding to the white circles marked 1–3 in a and b, deduced from the calculations. Red spheres, Cd atoms; green, Yb; white, Pb in the first layer; blue, Pb in the second layer; grey, Pb in the intermediate layer.

The Pb second-layer pentagon develops into a decagon with increasing coverage. The evolution to the decagon occurs when additional Pb atoms occupy the centre of the remaining Yb pentagons around the RTH cluster centre (refer to the model in Figure 8.2c). After 90 min deposition, a well-ordered network of Pb decagons is obtained (Figure 8.3a), where the Pb decagons are located at the vertices of a P1 tiling as expected from the substrate structure. Some of the Pb decagons are occupied by a single Pb atom at the centre, which is at the same height as the decagon.

The density of Pb atoms in the second layer is 7×10^3 to 8×10^3 atoms per Å^2. This value is in agreement with the density of adsorption sites expected from the substrate structure (6×10^3 to 8×10^3 sites per Å^2, that includes the centre of the RTH clusters).

A network of pentagons of two different orientations of edge length 15.8 ± 1 Å is observed at 2.8 ± 0.3 Å above the second layer and, thus, this network forms a third layer (Figure 8.3b). The pentagons are inflated by τ with respect to the pentagons in the first layer and they form part of a P1 tiling.

In addition to the first, second and third layers, Pb atoms at three other heights are also observed. Two of these additional layers are observed by STM below and above the second layer. We will refer to these layers as intermediate layers. The calculations discussed below reveal the existence of another layer in between the substrate and the first layer, and we will refer to this as an underlayer. This layer was not identified by STM, being underneath the first layer, but was detected by XPS. XPS probes the top few surface layers, whereas STM provides information on only the topmost layer. This technique also allows a determina-tion of the growth mode and the amount of Pb adsorbed on the surface. At higher coverages, Pb develops three-dimensional, rotational epitaxial periodic islands with (111) surface orientation on top of the quasicrystalline film.

Features of the intermediate layers are apparent in Figures 8.2a and 8.3b. A shallow broad feature identified in some of Pb decagons is measured at 1.0 ± 0.1 Å below the second layer or ~1 Å above the first layer, as demonstrated by a height profile in Figure 8.2.

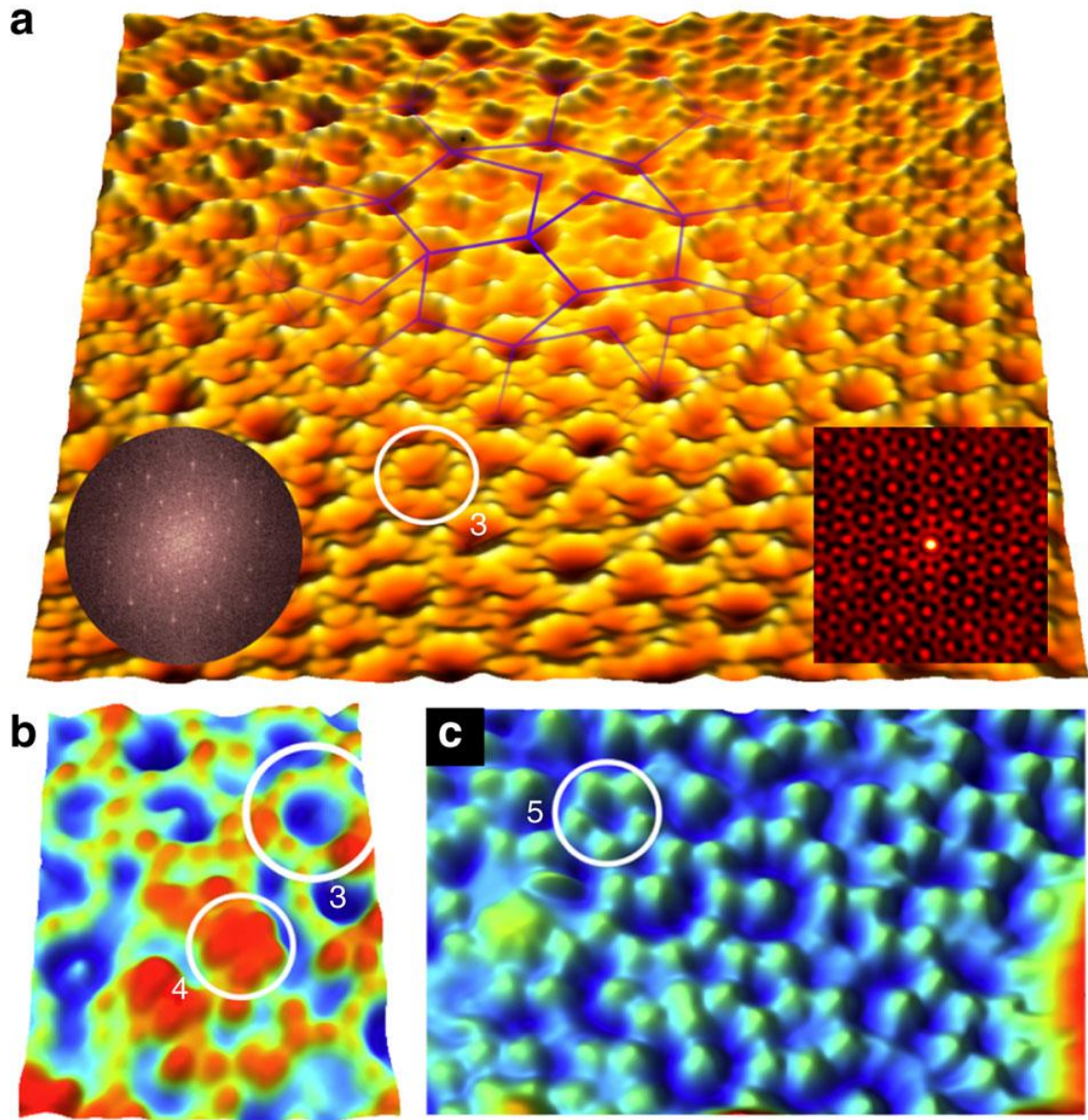**Figure 8.3 - Quasicrystalline Pb layers at different heights. (a) STM image (300 Å _ 300 Å) of the fivefold i-Ag-In-Yb surface after deposition of Pb for 90 min. Left inset: Fourier transform of the image. Right inset: a section of autocorrelation function of a 1,000 Å _ 1,000 Å STM image (180 Å _ 145 Å). A P1 tiling patch is overlaid, which is inflated by t with respect to the tiling of the substrate or first layer. (b,c) STM images at the same coverage demonstrating the intermediate (b) and third layer (b: 300 Å _ 300 Å; c: 270 Å _ 150 Å) with quasicrystalline order. The white circles marked 3, 4 and 5 identify the second, intermediate and third layer features, respectively, discussed in the text.**

These features develop simultaneously with the second layer Pb atoms (refer to the centre of the marked pentagon in Figure 8.2a). Similarly, a pentagon marked 4 in Figure 8.3b is identified above the second layer and below the third layer. In addition to these pentagons, isolated Pb atoms are observed at the same height and, thus, these atoms constitute the intermediate layers.

To measure the growth curve by XPS, the intensity of core-level peaks of the substrate (In 3d) and film (Pb 4f) were measured as a function of Pb coverage, as plotted in Figure 8.4a. A point of intersection of line segments with different gradients corresponds to a completion of a layer. Three inflection points are observed, indicating that three layers are successively formed. A comparison of STM and LEED results suggests that the first and second layers are completed at the first (11 min) and third (50 min) inflection points. The second inflection point (25 min) confirms the formation of an extra layer, the underlayer. As shown in the desorption curve in Figure 8.4a (inset), the second layer starts to desorb at ~370 K (end of the first plateau in the graph) and the first layer at ~540 K. This further indicates that the two layers have non-identical binding energies, as expected from the growth of successive layers observed in the growth curve as well as in STM images. No inflection point corresponding to the other layers has been observed in the growth curve, possibly because they grow simultaneously with other layers or their density is too low to observe a break point. For the same reason, desorption temperatures of the other layers could not be determined from the desorption curve.

LEED was employed to determine the long-range order of the film. LEED taken from each of the Pb layers show fivefold patterns with spots at the same positions as the clean surface, as shown in Figure 8.4b, which was recorded after formation of the

second layer. This confirms that the Pb layers have quasicrystalline longrange order expected from the substrate. The LEED results are consistent with Fourier transforms of STM images, which exhibit tenfold symmetry with maxima located at τ scaling distances (Figure 8.3a, inset). The modulation in the autocorrelation of STM images extends up to maximum distances within the STM images without significant decrease in intensity (Figure 8.3a, inset). This also demonstrates an undiminished long-range order within the experimentally probed length scale.

DFT calculations and comparison with STM. To evaluate adsorption energies for Pb atoms on the i-Ag-In-Yb surface, we performed total energy calculations based on DFT using the VASP code [27, 28]. The adsorption energy was calculated for different sites around the RTH cluster centre as a function of distance from the surface and optimal adsorption heights were identified. Four optimum heights were found. Three of them are at 0.5, 1.2 and 2.3 Å (Figure 8.5e, f). The fourth one will be discussed later. The two-dimensional energy maps at 1.2 and 2.3 Å heights are plotted in Figure 8.5a, b. These heights correspond to the height of the first and second Pb layers observed by STM microscopy. The adsorption energy is defined by,

$$E_{ads} = E_{substrate + atom} - E_{substrate} - E_{atom} \qquad \qquad 8.1$$

thus, a larger negative value indicates a more stable site. In agreement with the STM observations, the most stable sites for the first layer are identified between the In and Yb rings, which make a pentagon around the RTH cluster centre. These sites are indicated as '1st' in the figure. The expected structure of the first layer is represented by white spheres in the side view (Figure 8.5c,d). After the formation of the first layer, Pb atoms are adsorbed at 0.5 and 0.6 Å above the surface. These underlayer sites are represented by blue spheres in the figure (refer to as Under). The energy curve for the

adsorption sites at 0.5 Å is slightly different from the sites at 0.6 Å. We show the energy curve at 0.5 Å in Figure 8.5e as a representative.

After the underlayer sites are occupied, five deep minima (2nd_1) and the other shallow minima (2nd_2) are obtained at the centre of Yb pentagons surrounding the RTH cluster centre. These sites are at 2.3 Å from the surface and, thus, correspond to adsorption sites for the second layer. As the potential at the 2nd_1 site is slightly deeper than at the 2nd_2 site, a Pb pentagon forms first in the second layer rotated by 36° compared with the pentagon in the first layer and larger by a factor of τ. This is observed by STM. After completion of the pentagon, the shallower 2nd_2 sites are occupied, forming a decagon, again consistent with the STM results.
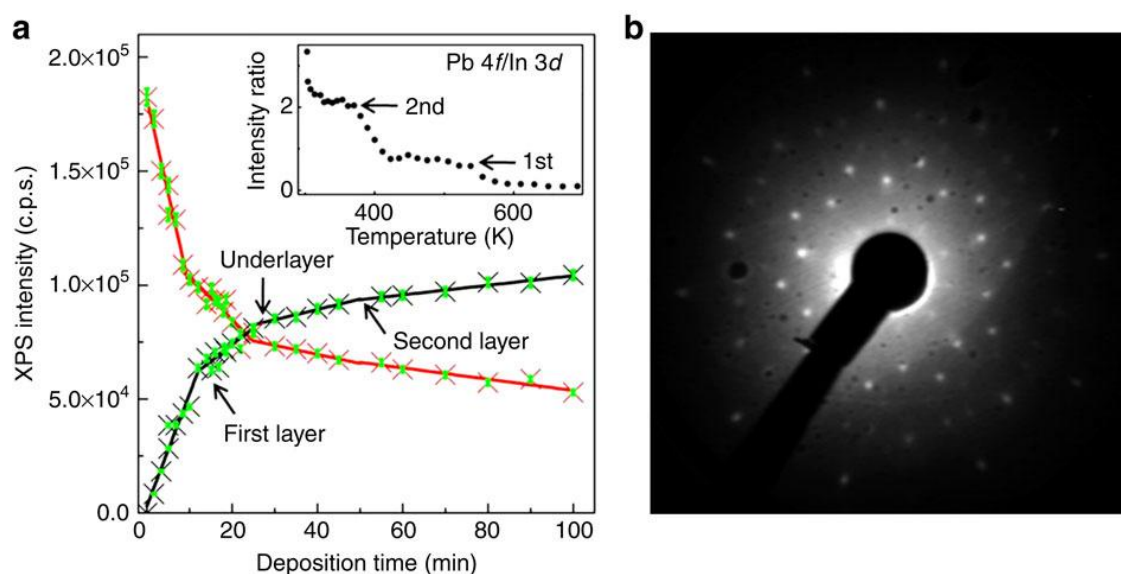

Figure 8.4 - Growth and stability, and long-range order of the Pb overlayer. (a) Variation of XPS intensity of the substrate (In 3d) and film (Pb 4f) as a function of deposition time, fitted with lines of different gradients. Error in intensity is shown by green bars. Inset: the ratio of Pb 4f and In 3d intensity after annealing the Pb-covered surface at different temperatures. The intensity corresponding to the first, second and underlayers is marked by arrows. (b) LEED pattern after formation of the second layer Pb taken using MCP-LEED optics (beam energy 24 eV).
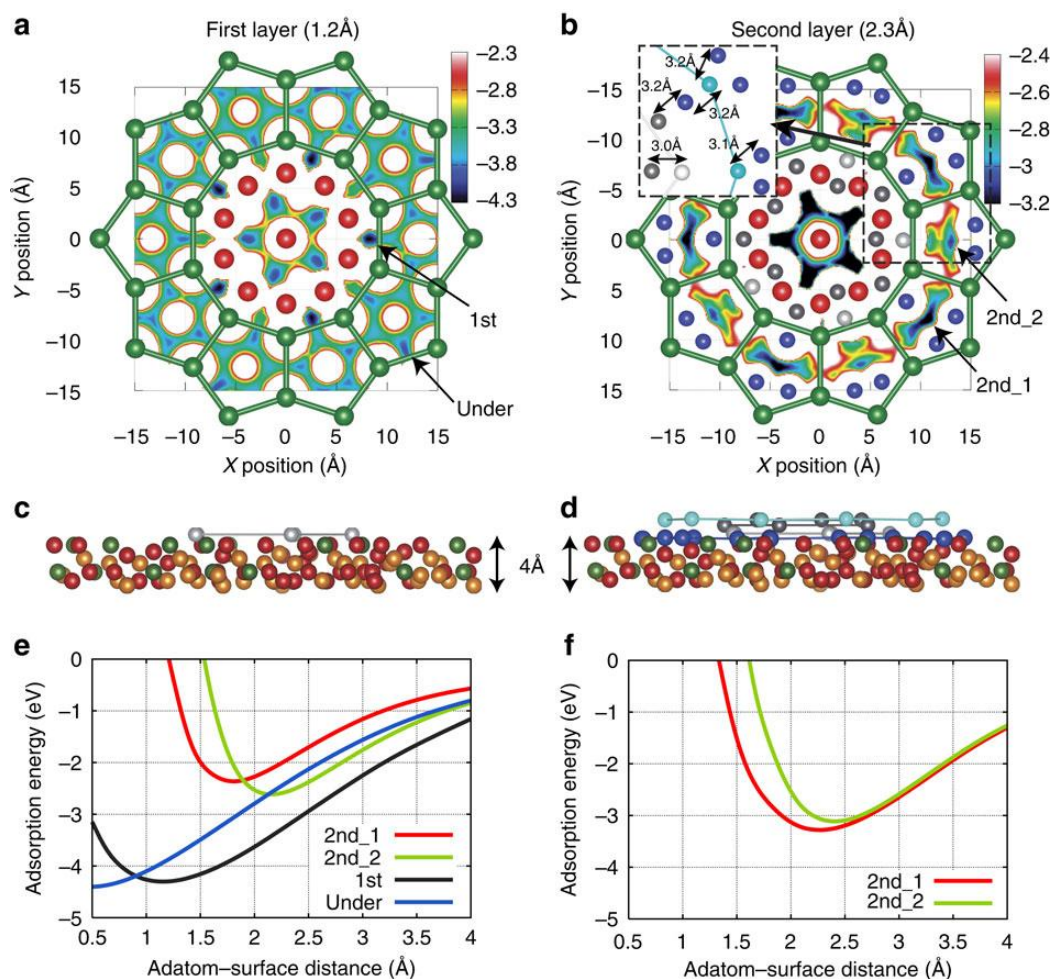
Figure 8.5 - Theoretical results for adsorption energies of the Pb layers. (a,b) Adsorption energy map for first and second layer Pb atoms around the RTH cluster centre, overlaid with atomic positions for the topmost substrate layer and Pb. Green spheres correspond to Yb, red to In, orange to Ag and other colours to Pb atoms. Inset shows the interatomic distances between adsorbed Pb atoms (see text). (c,d) Side view of atomic structure for the substrate and Pb film. (e,f) Adsorption energies for selected sites as a function of distance from the surface. Adsorption energy curves for 2nd_1 (red) and 2nd_2 (green) sites in e were calculated with the absence of the underlayer, and the same curves in f are after the underlayer atoms are considered. The centre pentagonal sites in a (right) have the highest adsorption energy. We note that a repulsive interaction is expected between atoms adsorbed on centre pentagonal sites, shown in Figure 8.5b. Therefore, these sites may be occupied partially. However, adsorption behaviour at these sites is ambiguous because of lack of information of exact atomic structure at the centre of the RTH cluster.

We also identify adsorption sites of two different types located near to the RTH cluster centre, which are represented by grey spheres in Figure 8.5a,b. These sites appear slightly below the second layer and above the first layer. In addition, the calculation indicates the existence of stable adsorption sites above the second layer and around 2nd_1 and 2nd_2 sites. From the location and height distribution, we infer that these sites correspond to the intermediate layers identified by STM.

The adsorption sites identified by STM and calculations are found to be identical to the atomic positions in the RTH cluster. The atoms of a given layer occupy sites of specific chemical species in the cluster. To demonstrate this, we present the atomic structure derived from the bulk model of i-Ag-In-Yb in Figure 8.6. The position and atomic density of the layers, which are formed by atoms of different shells of the RTH cluster, are given in Figure 8.6a. The in-plane structure of the layers are shown in Figure 8.6b-d. The atoms in the innermost tetrahedral shell are not shown, as their density is low.

The surface plane is an Yb-rich layer intersecting the centre of the RTH clusters as described above. This plane is at $z = 0$ in Figure 8.6a. Arrows indicate the layers of atomic sites occupied by Pb. The nth shell of the RTH cluster is indicated in parentheses. Figure 8.6b is the in-plane structure for $0 < z < 0.9$ Å. In sites of the fourth shell of the RTH cluster are plotted by large grey spheres. Most of these sites form a pentagon or a part of it, and the edge length of the pentagon agrees with that of the first-layer Pb pentagon obtained in experiment (9.2 ± 0.5 Å). Figure 8.6c shows the in-plane structure of the range $1.53 < z < 3.15$ Å, where the Yb sites (the third shell of the RTH cluster, blue spheres) form decagons. The edge length of the decagons matches again with that of observed second layer Pb (13.8 ± 1.5 Å). We can also identify sites corresponding to the third layer Pb, which are presented in Figure 8.6d.
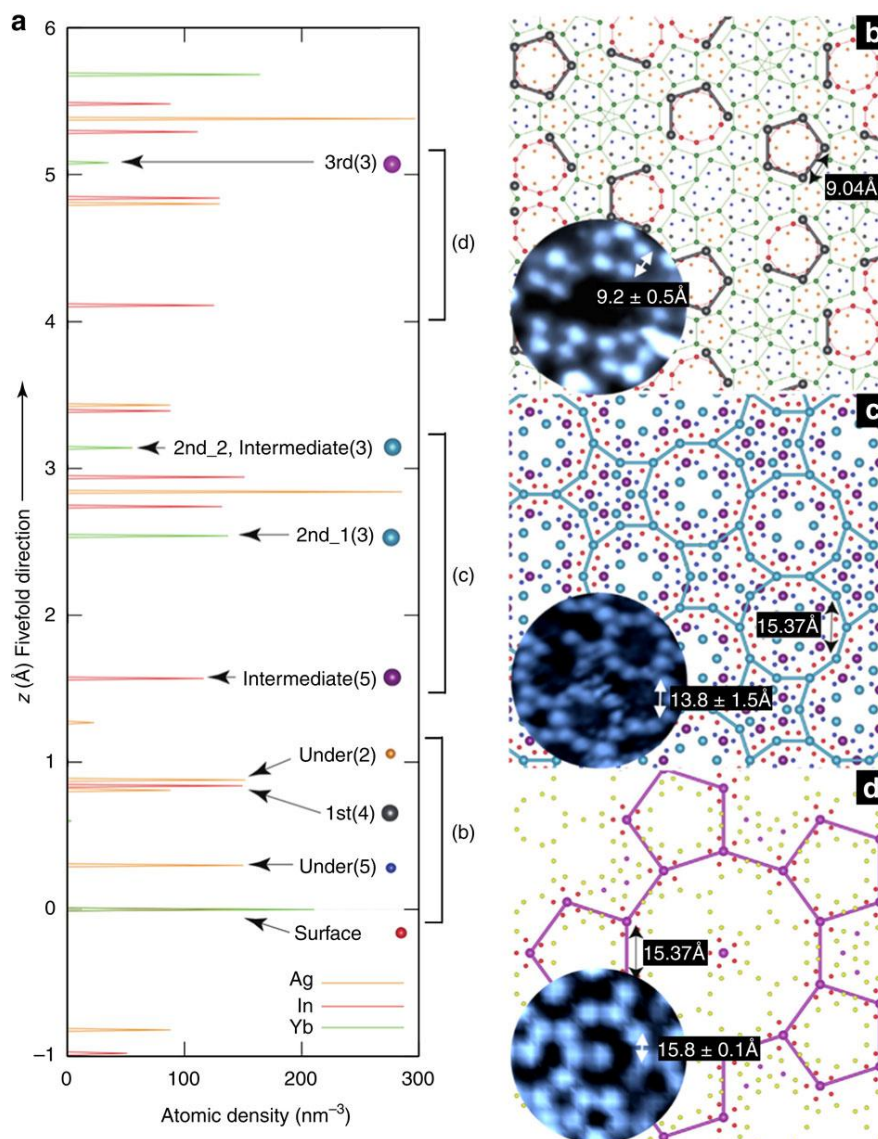
Figure 8.6 - Structure model of Pb layers. (a) The atomic density distribution of *i*-Ag-In-Yb along the fivefold direction. The density is estimated in slabs of 0.01 Å thickness. The Yb rich at plane intersecting the centre of RTH cluster represents the topmost surface layer (z = 0). Pb layers are formed at planes indicated by arrows. The nth shell of the RTH cluster is indicated in parentheses. (b–d) The in-plane atomic structure in a slab marked in a (b, 0 ≤ z ≤ 0.90 Å; c, 1.53 ≤ z ≤ 3.15 Å; d, 5.04 ≤ z ≤ 5.40 Å). (b) The surface In and Yb atoms are plotted in small red and green spheres, respectively, and are connected by thin lines. In sites are plotted by large grey spheres and connected by thick lines. These sites are identical to the first layer Pb (see inset). (c) Yb (large blue) and In (large magenta) sites correspond to the second and intermediate Pb layers, respectively. (d) Yb (large purple) corresponds to the third layer Pb. Inset of b–d is STM image of the first, second and third layer Pb, respectively.

The edge length of the decagon in the model structure is also in agreement with that of the third layer Pb (15.8±1 Å). Similarly, the sites related to the under- and intermediate layers can also be derived from the model structure (shown in Figure 8.6b,c, respectively). Although the lateral position of adsorption sites obtained in calculation agrees exactly with the bulk structure, the absolute heights of the layers differ slightly from the bulk values, probably because of the relaxation of the Pb layers due to the absence of the bulk structure in vacuum.

The adlayer–adlayer interaction is crucial for stability of the Pb film. The calculation reveals that the second-layer Pb is significantly stable only if the underlayer is present. This is demonstrated in Figure 8.5e, f, where we compare the adsorption energy curve for the second layer atoms with and without the existence of the underlayer. The adsorption energy of 2nd_1 and 2nd_2 sites increases by about 1 and 0.5 eV, respectively, after the formation of the underlayer. Similarly, the existence of the intermediate layer lowers the potential for the 2nd_1 site compared with the 2nd_2 site. This change in the potential landscape induced by the underlayer (and intermediate layer) explains the STM observations that the second layer Pb pentagons are oriented by 36° with respect to the pentagons in the first layer, and they evolve to decagons with increasing Pb coverage. We also find another relationship that implies the importance of the order of adsorption between the first layer and underlayer. If the underlayer is formed before the first layer, the first layer Pb pentagons observed by STM cannot be produced by calculation. Furthermore, the interatomic distance between the adsorbed Pb atoms is short enough to conclude a strong interaction between the adatoms. These distances are shown in Figure 8.5b (inset). The calculated values are shorter than the nearest neighbour distance in the fcc Pb (3.5 Å). We suggest that the shorter Pb–Pb

distances are caused by attractive interactions with the substrate and perhaps also by underestimation of DFT.

It is known that Pb is immiscible to Ag, but forms a solid solution with In, and forms several intermetallic compounds with Yb [29]. This suggests strong bonding for Pb–Yb and Pb–In. The top layer of the substrate in the present model consists of only In and Yb. This particular surface composition may be crucial for stabilizing the overlayer of Pb. Other elements such as Bi and Sb are expected to form strong bonds with Yb as characterized by the high melting temperature of intermetallic compounds of these elements [30, 31]. Indeed, further STM measurements show both elements produce first and second layers on the same substrate, and preliminary DFT calculations also support the existence of stable pseudomorphic Bi and Sb layers. However, the detail of each Bi or Sb layer is different from that of Pb, possibly because the Bi–Bi or Sb–Sb distance in the bulk is slightly different from that of Pb. The details of the Bi and Sb results will be published elsewhere.

The impact of our findings is fourfold. First, the proposed mechanism allows the prediction of other novel epitaxial material phases. Second, as all available bulk quasicrystals are associated with a complex chemistry, it has not been possible previously to separate the influence of quasicrystalline order and chemistry on the intriguing physical properties of quasicrystals. The single-element systems presented in this work exhibit quasicrystalline order with chemical simplicity and thus these can be used as model systems to study the impact of quasicrystalline order on physical properties, independent of chemical complexity. Third, the physical properties of a material are governed by atomic order. It will be of great interest to compare physical properties such as superconductivity between Pb in its natural periodic form and in the

quasicrystalline allotrope. Fourth, element-specific experimental techniques can be employed to exclusively probe the quasicrystalline overlayer without a contribution from the underlying substrate.

8.5 - Conclusion

In conclusion, we have presented the first observations of three-dimensional growth of quasicrystalline thin film of a single element. The film is formed on the fivefold surface of the i-Ag-In-Yb quasicrystal. Employing the experimental techniques of STM, XPS, LEED and DFT calculations, we have determined the atomic structure of the film. The deposited Pb atoms occupy the atomic sites of the RTH cluster, the building block of the substrate, and thus grow in layers with different heights and different adsorption energies. The Pb–Pb atomic distance in the film is sufficiently short compared with the bulk Pb to indicate a strong adlayer– adlayer interaction, which stabilizes the layered structure. The discovery of such a template single-element quasicrystalline thin film presents several new and exciting opportunities for further investigation of the impact of quasicrystallinity on the chemical and physical properties of materials, such as the superconductiv-ity of quasicrystalline Pb.

8.6 – References

[1] Shechtman, D., Blech, I., Gratias, D. and Cahn, J. W. 1984. Metallic phase with long-range orientational order and no translational symmetry. *Phys. Rev. Lett.* 53, pp. 1951–1953.

[2] Zeng, X., Ungar, G., Liu, Y., Percec, V., Dulcey, A.E. and Hobbs, J.K., 2004. Supramolecular dendritic liquid quasicrystals. *Nature,* 428, pp. 157.

[3] Takano, A., Kawashima, W., Noro, A., Isono, Y., Tanaka, N., Dotera, T. and Matsushita, Y., 2005. A mesoscopic Archimedean tiling having a new complexity in an ABC star polymer. *Journal of Polymer Science Part B: Polymer Physics,* 43, pp. 2427.

[4] Mikhael, J., Roth, J., Helden, L. and Bechinger, C., 2008. Archimedean-like tiling on decagonal quasicrystalline surfaces. *Nature,* 454, pp. 501.

[5] Foerster, S., Meinel, K., Hammer, R., Trautmann, M. & Widdra, W. Nature (2013) 10.1038/nature12514.

[6] Tsai, A.P., Inoue, A., and Masumoto, T., 1987. A Stable Quasicrystal in Al-Cu-Fe System. *Japanese Journal of Applied Physics,* 26(9), pp. L1505- L1507.

[7] Sharma, H.R., Shimodaa, M. and Tsaib, A.P., 2007. Quasicrystal surfaces: structure and growth of atomic overlayers *Advances in Physics,* 56, pp. 403.

[8] Ishii, Y. & Fujiwara, T. In Ishii, Y. & Fujiwara, T. (eds.) 2008. Quasicrystals, Elsevier pp. 171.

[9] Rapp.O. In Stadnik, Z. (ed.) 1999. *Physical Properties of Quasicrystals*, 119 Springer, New York, pp. 119.

[10] Dubois, J.M., 2005. *Useful Quasicrystals.* World Scientific.

[11] Park, J.Y., Ogletree, D.F., Salmeron, M., Ribeiro, R.A., Canfield, P.C., Jenks, C.J. and Thiel, P.A., 2005. High Frictional Anisotropy of Periodic and Aperiodic Directions on a Quasicrystal Surface. Science, 309, pp. 1354.

[12] Franke, K.J., Sharma, H. R., Theis, W., Gille, P., Ebert, Ph., and RiedeR, K. H., 2002. Quasicrystalline epitaxial single element monolayers on icosahedral Al- Pd- Mn and decagonal Al –Ni- Co quasicrystal surfaces. *Phys. Rev. Lett.* 89, 156104– 156107 .

[13] Smerdon, J.A., Parle, J.K., Wearing, L.H., Lograsso, T.A., Ross, A.R. and McGrath, R., 2008. Nucleation and growth of a quasicrystalline monolayer: Bi adsorption on the fivefold surface of i-$Al_{70}Pd_{21}Mn_9$. *Phys. Rev. B*, 78(7), pp. 075407.

[14] Ledieu, J., Leung, L., Wearing, L.H. and McGrath, R., 2008. Self-assembly, structure, and electronic properties of a quasiperiodic lead monolayer. *Phys. Rev. B,* 77(7), pp. 073409.

[15] Smerdon, J.A., Leung, L., Parle, J.K., Jenks, C.J., McGrath, R., Fournée, V. and Ledieu, J., 2008. Formation of a quasicrystalline Pb monolayer on the 10-fold surface of the decagonal Al–Ni–Co quasicrystal. *Surface Science*, 602(14), pp. 2496-2501.

[16] Sharma, H.R., Shimoda, M., Ross, R., Lograsso, T.A. and Tsai, A.P., 2005. Real-space observation of quasicrystalline Sn monolayer formed on the fivefold surface of icosahedral Al-Cu-Fe quasicrystal. *Phys. Rev. B*, 72(4), pp. 045428.

[17] Ledieu, J., Hoeft, J.T., Reid, D.E., Smerdon, J.A., Diehl , R.D., Lograsso, T.A., Ross, A.R. and McGrath, R., 2004. Pseudomorphic Growth of a Single Element Quasiperiodic Ultrathin Film on a Quasicrystal Substrate. *Phys. Rev. Lett.*, 92, pp. 135507.

[18] Ledieu, J., Hoeft, J.Y., Reid, D.E., Smerdon, J.A., Diehl, R.D., Ferralis, N., Lograsso, T.A., Ross, A.R. and McGrath, R., 2005. Copper adsorption on the fivefold $Al_{70}Pd_{21}Mn_9$ quasicrystal surface. *Phys. Rev. B*, 72(3), pp. 035420.

[19] Smerdon, J.A., Ledieu, J., Hoeft, J.T., Reid, E., Wearing, L.H., Diehl, D., Lograsso, T.A., Ross, R. and McGrath, R., 2006. Adsorption of cobalt on the tenfold surface of d-$Al_{72}Ni_{11}Co_{17}$ and on the fivefold surface of i-$Al_{70}Pd_{21}Mn_9$. *Philosophical Magazine*, 86, pp. 841.

[20] Fournée, V., Sharma, H.R., Shimoda, M., Tsai, A.P., Unal, B., Ross, A.R., Lograsso, T.A. and Thiel, P.A., 2005. Quantum Size Effects in Metal Thin Films Grown on Quasicrystalline Substrates. *Phys. Rev. Lett.*, 995, pp. 155504.

[21] Ünal, B., Fournée, V., Thiel, P.A. and Evans, J.W., 2009. Structure and Growth of Height-Selected Ag Islands on Fivefold i-AlPdMn Quasicrystalline Surfaces: STM Analysis and Step Dynamics Modeling. *Phys. Rev. Lett.*, 102, pp. 196103.

[22] Tsai, A.P., Guo, J.Q., Abe, E., Takakura, H. and Sato, T.J., 2000. Alloys: A stable binary quasicrystal. *Nature*, 408, pp. 537.

[23] Takakura, H., Gómez, C.P., Yamamoto, A., Boissieu, M.D. and Tsai, A.P., 2007. Atomic structure of the binary icosahedral Yb–Cd quasicrystal. *Nature Materials*, 6, pp. 58.

[24] Sharma, H.R., Shimoda, M., Sagisaka, K., Takakura, H., Smerdon, J.A., Nugent, P.J., McGrath, R., Fujita, D., Ohhashi, S. and Tsai, A.P., 2009. Structure of the fivefold surface of the Ag-In-Yb icosahedral quasicrystal. *Phys. Rev. B*, 80, pp. 121401.

[24] Penrose, R., 1974. The role of Aesthetics in pure and applied mathematics. *Bull Inst. Math. Appl.*, 10, pp. 266.

[26] Sharma, H.R., Simutis, G., Dhanak, V.R., Nugent, P.J., Cui, C., Shimoda, M., McGrath, R., Tsai, A.P. and Ishii, Y., 2010. Valence band structure of the icosahedral Ag-In-Yb quasicrystal. *Phys. Rev. B*, 81(10), pp. 104205.

[27] Kresse, G. and Hafner, J., 1993. Ab initio molecular dynamics for liquid metals. *Phys. Rev. B*, 47, pp. 558.

[28] Kresse, G. and Furthmüller, J., 1996. Efficient iterative schemes for ab initio total-energy calculations using a plane-wave basis set. *Phys. Rev. B*, 54(16), pp. 11169.

[29] Sommer, F., Predel, B., Borzone, G., Parodi, N. and Ferro, R., 1995. Calorimetric determination of the enthalpies of formation of liquid and solid Yb☐Pb alloys. *Intermetallics*, 3(1), pp. 15-22.

[30] Okamoto, H., 1999. Bi − Yb (bismuth-ytterbium). *Journal of Phase Equilibria*, 20, pp. 453

 [31] Okamoto, H., 2008. Sb-Yb (antimony-ytterbium). *Journal of Phase Equilibria*, 29, pp. 473.

[32] Kresse, G. and Joubert, D., 1999. From ultrasoft pseudopotentials to the projector augmented-wave method. *Physical Review B - Condensed Matter and Materials Physics*, 59(3), pp. 1758-1775.

[33] Perdew, J.P., Burke, K. and Ernzerhof, M., 1196. Generalized Gradient Approximation Made Simple. *Phys. Rev. Lett*., 77(18), pp. 3865.

[34] Nozawa, K. and Ishii, Y., 2010. Electronic structures and stability of Ag − In − Ca surfaces. *J. phys. conference series*, 226, pp. 012030.

Chapter 9

Conclusion

9.1 - Conclusion

The growth of Bi on Ag(111) has been studied with a variety of techniques starting with sub-monolayer coverage and up to the self assembly of nanostructures at higher depositions.

At approximately 1/3 of a monolayer we reported the formation of a $(\sqrt{3} \times \sqrt{3})R30°$ structure using LEED I-V and DFT analyses. We found good agreement between the experimental and theoretical results. LEED analysis shows that the Bi atoms are found to replace one top layer Ag atom in each unit cell, forming a substitutional unfaulted surface alloy. DFT calculations show that the stable $(\sqrt{3} \times \sqrt{3})R30°$ structure is a surface alloy, but does not distinguish between a faulted and unfaulted structure, possibly due to limitation of using a finite size slab. Because of the size difference between the Ag and Bi atoms (Bi is approximately 5% larger than Ag), the top layer is corrugated such that the Bi atoms reside about 0.6 Å above the Ag atoms. The amplitude of this 'rumpling' is smaller than what would be predicted on a simple touching hard-spheres model. The interlayer spacings, calculated with respect to the centres of mass of the Ag atoms, remain bulk like in both DFT and LEED analyses.

The growth of Bi on Ag(111) induces a number of different surface structures. As well as the $(\sqrt{3} \times \sqrt{3})R30°$ surface alloy, there is also the formation of a Bi-$(p \times \sqrt{3})$ overlayer and Bi(110) thin film as a function of increasing Bi coverage. We have investigated the coverage dependent electronic states of Bi ultra thin films deposited on Ag(111) by XPS and UPS. The evolution of electronic states is in accordance with previous structural investigations by STM and LEED [4-6]. At low Bi coverage ($\theta <$ 0:55 ML), Bi atoms intermix with Ag to form Ag_2Bi surface alloy and the sp-derived

Shockley surface state on Ag(111) is rapidly quenched. As Bi coverage increases, Bi(110) overlayer forms on Ag(111) and a new state is observed at $\theta \sim 0{:}9$ ML arising from electronic states localized at the Ag–Bi interface. The core level of Bi 4f for the Ag_2Bi alloy are shifted to lower binding energy by ~0.6 eV and ~0.3 eV compared with that of bulk Bi and Bi(110) thin film on Ag(111) respectively. The core level binding energy shifts are associated with a complex superposition effect of outward relaxation of Bi atoms, final state screening and charge transfer from Bi to Ag substrate.

These same structures formed by the deposition of Bi on Ag(111) were then studied using low-temperature scanning tunneling microscopy, low-energy electron diffraction, and ab initio calculations. We investigated the coverage-dependent growth of Bi on Ag(111) and identified a number of atomically ordered structures. The system exhibits an alloying and dealloying process that is typical for metal-on-metal systems where the individual components are not miscible as bulk phases. It is energetically favourable for the initially deposited Bi atoms to be incorporated into the topmost Ag(111) layer by exchanging with surface Ag atoms to form a dilute array of substitutional Bi atoms within the Ag matrix as well as an adlayer of the Ag_2Bi surface alloy. Since the incorporation of larger-sized Bi atoms presumably induces a compressive strain, a surface dealloying process ensues when the Bi coverage is reaches a critical value. Future stress measurements or kinetic Monte Carlo calculations are required to elucidate the mechanisms and driving force for the dealloying process. Nevertheless the Ag_2Bi alloy phase gradually converts into an ordered (p × √3) overlayer structure with a rectangular lattice 2D surface cell with $a_1 = 5.0$ Å , $b_1 = 4.7$ Å supported on Ag(111). After the dealloying process is complete, Bi(110) thin films can be finally grown epitaxially on Ag(111) with a chemically abrupt interface. The "rumpling" of the

surface alloy determined from experimental and ab initio calculations may provide additional information necessary to understand the giant spin splitting recently observed in the Bi/Ag(111) surface alloy system, which was believed to originate from a strong in-plane gradient of the crystal potential in the surface layer. This also provides a model system to envision the alloying process in other systems such as Pb on Ag(111), which exhibit a large Rashba effect. The ultrathin Bi films on Ag(111) may exhibit unusual properties originating from quantum confinement effects coupled with the unique properties of the Bi surface, opening up potential applications in spintronic devices[7-8]. As an elegant example, the quantum well state confinement by the ultrathin Bi film can induce a huge SO splitting. From a fundamental point of view, the results contribute further to the understanding of surface and interface phenomena in heteroepitaxial growth in materials.

The $(\sqrt{3} \times \sqrt{3})R30°$ structure formed by the deposition of 1/3 ML of Pb on Ag(111) has also been studied with a variety of techniques.

Initially the system was examined using LEED I-V and DFT. We reported very good agreement between the geometrical parameters extracted from both of these analysis techniques. LEED analysis confirmed that the Pb atoms are found to replace one top layer Ag atom in each unit cell, forming a substitutional unfaulted surface alloy. DFT calculations show that the stable $(\sqrt{3} \times \sqrt{3})R30°$ structure is a surface alloy, but does not clearly distinguish between a faulted and unfaulted structure, possibly due to limitation of using a finite size slab. Similarly to the Bi/Ag(111) system we found the top layer is corrugated such that the Pb atoms reside about 0.4 Å above the Ag atoms. The amplitude of this 'rumpling' is smaller than what would be predicted on a simple touching hard-spheres model. The interlayer spacings, calculated with respect to the

centres of mass of the Ag atoms, remain bulk like in both DFT and LEED analyses. Both LEED and DFT marginally favour the structure with no rumpling between the surface Ag atoms as previously reported by Dalmas *et al.*[9]. although given the small size of any possible distortion and the limitations of the techniques the rumpled structure could not be ruled out.

The situation regarding any rumpling of Ag atoms in the surface unit cell of the Pb/Ag(111) system was still uncertain. In order to further clarify the structure we conducted a MEIS experiment on the $(\sqrt{3} \times \sqrt{3})R30°$ surface. We found good agreement between the geometrical parameters extracted from MEIS data and previous studies as shown in the table, below.

	LEED IV	**MEIS**	**DFT**
R-Factor	0.21±0.02	0.26±0.1	
Adsorption Energy			-0.290
Rumpling	0.42±0.06	0.4±0.2	0.59

Table 9.1 – R factors for Pb/Ag(111) $(\sqrt{3} \times \sqrt{3})R30°$ substitutional, unfaulted structure as calculated by MEIS, LEED I-V and DFT. The errors on the LEED R-factors were derived from Pendry's variance, namely by varying a certain parameter away from the best-fit structure until the difference between the according R factor got larger than this variance. Errors on the MEIS R-factors were calculated from the spread of individual R factors from each geomertry from each of the data sets.

MEIS analysis shows that the Pb atoms are found to replace one top layer Ag atom in each unit cell, forming a substitutional unfaulted surface alloy with the Pb atoms residing about 0.4 Å above the Ag atoms. The results marginally favour the structure with no rumpling between the surface Ag, again in contrast with the Dalmas model. However, given the small size of any possible distortion and the limitations of the technique the rumpled structure still cannot be ruled out.

Lead and bismuth are similar elements, both forming a $(\sqrt{3} \times \sqrt{3})R30°$ surface alloy at low coverages. There is, however, an apparent discrepancy concerning the values of surface rumpling when we compare the two systems. Pb has an atomic radius of 180 pm compared with 156 pm for Bi so it would be expected that the Pb atoms would reside higher above the surface due to the larger size mismatch. In fact, what we see is the Pb having a surface rumpling of just 0.4 Å compared with 0.6 Å for Bi. Based on a simple electronegativity argument we would expect to see a charge transfer from Ag to Bi as their electronegativity values are 1.93 and 2.02 respectively. In chapter 3, we saw that this charge transfer was in agreement with XPS (binding energy of Bi 4f peaks were 0.3 eV lower for the Ag_2Bi surface compared with the Bi(110) overlayer) but was not supported by DFT results and workfunction changes. It was suggested that the charge transfer was actually from the Bi to the Ag and that the shift to lower binding energy for the Ag_2Bi was a combination of effects such as final state screening, reduced coordination number of Bi atoms and a more effective screening of holes by Ag electrons compared with the Bi(110) overlayer. The fact that the Bi atoms of the Ag_2Bi surface have a smaller rumpling than that expected from a simple hard spheres model could be explained by this charge transfer, the loss of an electron from Bi causing a reduction in its effective radius allowing it to sink further into the surface. This would

also explain the Pb atoms rumpling of 0.4 Å. We would expect a larger charge transfer from the Pb given its electronegativity of 1.87 and hence a larger reduction in its effective radius. The arguments do, however, rely on some degree of supposition and the results are by no means clear cut. Gierz et al. [10] state that the larger the surface relaxation, the larger the Rashba effect, which is why Bi/Ag(111) has a greater effect than Pb/Ag(111).

Finally we studied the deposition of Pb on the icosahedral Ag-In-Yb quasicrystal. We presented the first observations of multilayered quasicrystalline thin films of single elements. In this case the films were formed on the fivefold surface of the icosahedral quasicrystal. Employing the experimental techniques of STM, XPS and LEED, and DFT calculations, we determined the atomic structure of these multilayered films. The quasicrystalline Pb film consists of five atomic layers having distinct heights from the substrate and distinct binding energies. Each of the layers has a unique quasicrystalline structure propagated from the substrate structure. The chemical composition of the substrate is the most important factor for the stability of pseudomorphic overlayers and thus means that the prediction of new epitaxial materials on quasicrystal surfaces may be possible. To this end we deposited Bi on the same surface and used STM to study the surface. Though not presented here, we found Bi formed quasicrystalline overlayers with many features in common with those of the Pb overlayer. The discovery of multilayered single-element quasicrystalline thin films presents several exciting opportunities for further investigation of the impact of quasicrystallinity on the physical properties of materials, such as the superconductivity of quasicrystalline Pb and the Rashba effect in spin splitting of quasicrystalline Bi.

9.2 - References

[1] Quinn, P.D., Bittencourt, C. and Woodruff, D.P., 2002. Tensor LEED analysis of the Ni(111)($\sqrt{3}\times\sqrt{3}$)R30°-Pb surface. Phys. Rev. B, 65(23), pp. 233404

[2] Quinn, P.D., Brown, D., Woodruff, D.P., Bailey, P. and Noakes, T.C.Q., 2002. Structural study of the adsorption of Sb on Ag(1 1 1) using medium energy ion scattering. Surface Science, 511(1–3), pp. 43-56.; see also Woodruff, D.P., Muñoz-Márquez, M.A. and Tanner, R.E., 2003. Structural studies at metallic surfaces and interfaces using MEIS. Current Applied Physics, 3(1), pp. 19-24.

[3] Brown, D., Quinn, P.D., Woodruff, D.P., Bailey, P. and Noakes, T.C.Q., 2000. Medium-energy ion scattering structural study of the Ni(111)(v3×v3)R30°-Pb surface phase. Physical Review B - Condensed Matter and Materials Physics, 61(11), pp. 7706-7715.

[4] Zhang, K.H.L., McLeod, I.M., Lu, Y.H., Dhanak, V.R., Matilainen, A., Lahti, M., Pussi, K., Egdell, R.G., Wang, X.S., Wee, A.T.S. and Chen, W., 2011. Observation of a surface alloying-to-dealloying transition during growth of Bi on Ag(111). *Phys. Rev. B, 83*(23), pp. 235418.

[5] Zhang, H.L., Chen, W., Wang, X.S., Yuhara, J. and Wee, A.T.S., 2009. Growth of well-aligned Bi nanowire on Ag(1 1 1). *Applied Surface Science, 256*(2), pp. 460-464.

[6] McLeod, I.M., Dhanak, V.R., Matilainen, A., Lahti, M., Pussi, K. and Zhang, K.H.L., 2010. Structure determination of the Bi–Ag(111) surface alloy using LEED I–V and DFT analyses. *Surface Science, 604*(17–18), pp. 1395-1399.

[7] Hofmann, P., 2006. The surfaces of bismuth: Structural and electronic properties. Progress in Surface Science, 81(5), pp. 191-245.

[8] Mathias, S., Ruffing, A., Deicke, F., WIesenmayer, M., Sakar, I., Bihlmayer, G., Chulkov, E.V., Koroteev, Y.M., Echenique, P.M., Bauer, M. and Aeschlimann, M., 2010. Quantum-Well-Induced Giant Spin-Orbit Splitting. Phys. Rev. Lett., 104(6), pp. 066802.

[9] Dalmas, J., Oughaddou, H., Le Lay, G., Aufray, B., Tréglia, G., Girardeaux, C., Bernardini, J., Fujii, J. and Panaccione, G., 2006. Photoelectron spectroscopy study of Pb/Ag(1 1 1) in the submonolayer range. Surface Science, 600(6), pp. 1227-1230.

[10] Gierz, I., Stadtmüller, B., Vuorinen, J., Lindroos, M., Meier, F., Dil, J. H., Kern, K., Ast, C. R., 2010. The Structural Influence on the Rashba-type Spin-Splitting in Surface Alloys. arXiv:1003.2351v1 [cond-mat.mes-hall].

Appendix - List of Publications

McLeod, I.M., Dhanak, V.R., Matilainen, A., Lahti, M., Pussi, K. and Zhang, K.H.L., 2010. Structure determination of the Bi–Ag(111) surface alloy using LEED I–V and DFT analyses. *Surface Science,* 604(17–18), pp. 1395-1399.

McLeod, I.M., Dhanak, V.R., Lahti, M., Matilainen, A., Pussi, K. and Zhang, K.H.L., 2011. LEED *I–V* and DFT structure determination of the Pb–Ag(111) surface alloy. *Journal of Physics: Condensed Matter,* 23, pp. 265006.

Zhang, K.H.L., McLeod, I.M., Lu, Y.H., Dhanak, V.R., Matilainen, A., Lahti, M., Pussi, K., Egdell, R.G., Wang, X.S., Wee, A.T.S. and Chen, W., 2011. Observation of a surface alloying-to-dealloying transition during growth of Bi on Ag(111). *Phys. Rev. B,* 83(23), pp. 235418.

Zhang, K.H.L., McLeod, I.M., Lahti, M., Pussi, K., and Dhanak, V.R., 2012. The evolution of the electronic structure at the Bi/Ag(111) interface studied using photoemission spectroscopy. *Journal of Physics: Condensed Matter*, 24(43), pp. 435502.

King, M.O., McLeod , I.M., Hesp, D., Dhanak, V.R., Kadodwala, M., MacLaren, D, A., 2012. Growth and alloying of thin film Te on Cu(111). *Surface Science*. 606(17-18), pp. 1353–1359.

Tamura, R., Yadav, T.P., McLeod, I.M., Hesp, D., Young, K.M., Nakamura, T., Nishio, K., Dhanak, V.R., McGrath, R., and Sharma, H. R. 2013. Scanning tunneling microscopy of a polygrain Al–Pd–Re quasicrystal: study of the relative surface stability. *J. Phys.: Condens. Matter,* 25, pp. 395007.

Sharma, H. R., Nozawa, K., Smerdon, J. A., Nugent, P. J., McLeod, I., Dhanak, V. R., Shimoda, M., Ishii, Y., Tsai, A.P., McGrath, R. 2013. Templated three-dimensional growth of quasicrystalline lead. Nature communications, 4.